CERN / LHCC 99–32
ALICE TDR 6
30 September 1999

A L I C E

Technical Design Report

of the

Photon Multiplicity Detector (PMD)

Spokesperson
J. Schukraft

PMD Project Leader
Y.P. Viyogi

Technical Coordinator
W. Klempt

Engineering/Integration Coordinator
L. Leistam

Resources Coordinator
J. de Groot

Cover design by CERN Desktop Publishing Service

Printed at CERN
September 1999

ISBN 92-9083-153-7

ALICE Collaboration

Alessandria, Italy, Facoltà di Scienze dell'Università:
G. Dellacasa, L. Ramello, E. Scalas and M. Sitta.

Aligarh, India, Physics Department, Aligarh Muslim University:
N. Ahmad, S. Ahmad, T. Ahmad, W. Bari, M. Irfan and M. Zafar.

Athens, Greece, Nuclear and Particle Physics Division, University of Athens:
A.L.S. Angelis[1)], A. Kapogiannis, G. Mavromanolakis and A.D. Panagiotou.

Athens, Greece, Institute of Nuclear Physics, NRC Demokritos:
K. Kalfas.

Bari, Italy, Dipartimento di Fisica dell'Università and Sezione INFN:
D. Cozza, G. De Cataldo, D. Dell'Olio, L. Dell'Olio, D. Di Bari, D. Elia, N. Facchini, R.A. Fini, A. Franco, B. Ghidini, V. Lenti, L. Liberti, R. Loconsole, V. Manzari, E. Nappi[1)], F. Navach and F. Posa.

Bari, Italy, Politecnico and Sezione INFN:
F. Corsi, D. De Venuto, M. Di Ciano, R. Dinapoli, A. Grimaldi, P. Lamanna, C. Marzocca, G. Matarrese and E. Monno.

Beijing, China, China Institute of Atomic Energy:
H. Guo, C. Li, X. Li, S. Lu, Z. Lu, B. Sa, H. Wang, Y. Wang, J. Yuan, J. Zhou, S. Zhou and X. Zhu.

Bergen, Norway, Department of Physics, University of Bergen:
E. Andersen, K. Fanebust, H. Helstrup, A. Klovning, O.A. Maeland, O.H. Odland, D. Röhrich, R. Rongved and T.F. Thorsteinsen.

Bhubaneswar, India, Institute of Physics:
A.K. Dubey, D.P. Mahapatra, B. Mohanty and S.C. Phatak.

Birmingham, United Kingdom, School of Physics and Space Research, University of Birmingham:
I.J. Bloodworth, D. Evans, G.T. Jones, P. Jovanović, J.B. Kinson, A. Kirk, O. Villalobos Baillie and M.F. Votruba.

Bologna, Italy, University/INFN:
F. Anselmo, P. Antonioli, G. Bari, M. Basile, L. Bellagamba, D. Boscherini, L. Brocco, A. Bruni, G. Bruni, G. Cara Romeo, D. Casadei, E. Cerron, F. Cindolo, N. Coppola, M. Corradi, S. De Pasquale, D. Falchieri, A. Gabrielli, E. Gandolfi, P. Giusti, B. Guasina, D. Hatzifotiadou, N.Y. Kim, G. Laurenti, M.L. Luvisetto, A. Margotti, A. Masetti, T. Massam, D. Migani, R. Nania, F. Palmonari, A. Pesci, F. Pierella, A. Polini, G. Sartorelli, A. Semak, G. Valenti, M.C.S. Williams and A. Zichichi.

Bratislava, Slovakia, Faculty of Mathematics and Physics, Comenius University:
J. Braciník, V. Černý, J. Ftáčnik, V. Hlinka, M. Ivanov, R. Janik, R. Lietava, M. Pikna, J. Pišút, N. Pišútová, B. Sitar, P. Strmeň and I. Szarka.

Bucharest, Romania, National Institute for Physics and Nuclear Engineering:
A. Andronic, V. Catanescu, M. Ciobanu, M. Duma, D. Moisa, M. Petrovici, V. Simion, C. Staii and G. Stoicea.

Budapest, Hungary, KFKI Research Institute for Particle and Nuclear Physics, Hungarian Academy of Sciences:
E. Denes, B. Eged, Z. Fodor, G. Harangozo, T. Kiss, G. Palla, G. Rubin, J. Sulyan, L. Szendrey, J. Sziklai, D.L. Tarjan, Z. Varga, B.N. Vissy and J. Zimanyi.

Cagliari, Italy, Dipartimento di Fisica dell'Università and Sezione INFN:
C. Cicalo, A. De Falco, M.P. Macciotta-Serpi, A. Masoni, S. Mauro, G. Puddu, P. Randaccio, S. Serci, E. Siddi and G. Usai.

Calcutta, India, Saha Institute of Nuclear Physics:
P. Bhattacharya, S. Bose, Sukalyan Chattopadhyay, N. Majumdar, A. Sanyal, S. Sarkar, P. Sen, S.K. Sen and B.C. Sinha.

Calcutta, India, Variable Energy Cyclotron Centre:
Subhasis Chattopadhyay, M.R. Dutta Majumdar, M.S. Ganti, P. Ghosh, T.K. Nayak, S. Pal, R.N. Singaraju, Bikash Sinha, M.D. Trivedi and Y.P. Viyogi.

Catania, Italy, Dipartimento di Fisica dell'Università and Sezione INFN:
A. Badalà, R. Barbera, U. Becciani, M. Gulino, S. Ingrassia, A. Insolia, F. Librizzi, L. Lo Nigro, D. Lo Presti, D. Nicotra, A. Palmeri, G.S. Pappalardo, L. Pappalardo, C. Petta, N. Randazzo, S. Reito, F. Riggi, G.V. Russo and M. Russo.

CERN, Switzerland, European Laboratory for Particle Physics:
J. Bächler, J.A. Belikov[2)], V. Berejnoi[3)], J.-C. Berset, R. Brun, M. Burns, M. Campbell, E. Cantatore, W. Carena, F. Carminati, P. Chochula, J. Christiansen, D. Collados, J. Cruz de Sousa Barbosa, M. Davenport, J. de Groot, A. Di Mauro, R. Divià, C. Eisenberg, C. Engster, J. Espirito Santo, M. Fageda, H.G. Fischer, F. Formenti, D. Fraissard, E. Futo[4)], E. Gaumann, B. Goret, T. Grassi[5)], C. Gregory, M. Hoch, P.G. Innocenti, A. Jachołkowski, W. Klempt, A. Kluge, X. Lagrue, G. Lecoeur, J.C. Legrand, L. Leistam, P. Lenoir, Y. Lesenechal, C. Lourenço, P. Martinengo, M. Mast, T. Meyer, H. Milcent, R. Monnin, M. Morel, A. Morsch, M. Mota, L. Musa, B. Perrin, D. Picard, L. Pigni, F. Piuz, E. Quercigh, J. Raynaud, H. Renshall, A. Rivetti, K. Šafařík, J.-C. Santiard, J. Schukraft, E. Schyns, W. Snoeys, P. Sonderegger, M. Spegel, D. Swoboda, P. Szymanski, G. Tabary, J. van Beelen, H. van der Velde, P. Vande Vyvre, A. Vascotto, D. Vranic, S. Wenig, P. Wertelaers, T. Williams and K. Zelazowski.

Chandigarh, India, Physics Department, Panjab University:
M.M. Aggarwal, V.S. Bhatia, R. Chugh, A. Kumar and V. Vashisht.

Clermont-Ferrand, France, Laboratoire de Physique Corpusculaire (LPC), IN2P3-CNRS and Université Blaise Pascal:
IN2P3: J.P. Alard, A. Baldit, V. Barret, N. Bastid, G. Blanchard, J. Castor, T. Chambon, A. Cosquer, P. Crochet, F. Daudon, A. Devaux, P. Dupieux, B. Espagnon, J. Fargeix, P. Force, A. Genoux-Lubain, L. Lamoine, F. Manso, G. Roche, O. Roig, P. Rosnet, L. Royer and P. Saturnini.

Coimbra, Portugal, Departamento de Física, Faculdade de Ciências e Tecnologia:
R. Ferreira Marques, P. Fonte[1)] and A. Policarpo.

Columbus, U.S.A., Department of Physics, Ohio State University:
T.J. Humanic, M. Lisa, G. Lo Curto, B.S. Nilsen, G. Paić, D.M. Reichhold and E. Sugarbaker.

Copenhagen, Denmark, Niels Bohr Institute:
I. Bearden, H. Bøggild, J. Gaardhøje and B. Nielsen.

Cracow, Poland, Henryk Niewodniczanski Institute of Nuclear Physics, High Energy Physics Department:
J. Bartke, E. Gładysz-Dziaduś, E. Górnicki, M. Kowalski, A. Rybicki, P. Stefański and Z. Wlodarczyk[6)].

Darmstadt, Germany, Gesellschaft für Schwerionenforschung (GSI):
R. Averbeck, C. Blume, P. Braun-Munzinger, A. Deusser, A. Devismes, J. Eschke, P. Foka, C. Garabatos, B. Kolb, J. Lühning, U. Lynen, A.M. Marin, D. Miśkowiec, W.F.J. Müller, C. Neyer, A. Sandoval, H. Sann, H.R. Schmidt, A. Sharma, H. Stelzer and A. Wörner.

Frankfurt, Germany, Institut für Kernphysik, Johann-Wolfgang Göthe Universität:
C. Bormann, P. Buncic, M. Gaździcki, J. Günther, S. Lange, R. Renfordt, G. Roland, R. Stock and H. Ströbele.

Gatchina, Russia, St. Petersburg Nuclear Physics Institute:
V. Guersenchtein, B. Komkov, V. Kozlov V. Nikouline, V. Samsonov, O. Tarasenkova, S. Volkov and A. Vorobiev.

Heidelberg, Germany, Max-Planck-Institut für Kernphysik:
F. Ceretto, C. Fuchs, J. Rak and J.P. Wurm.

Heidelberg, Germany, Institut für Hochenergiephysik, Ruprecht-Karls Universität:
F.O. Lesser, V. Lindenstruth and A.G.E. Mass.

Heidelberg, Germany, Physikalisches Institut, Ruprecht-Karls Universität:
H. Appelshäuser, S. Esumi, K. Filimonov, P. Glässel, N. Herrmann, B. Lenkeit, M.J. Richter, W. Schmitz, J. Stachel, H. Tilsner, J.P. Wessels, T. Wienold and B. Windelband.

Ioannina, Greece, University of Ioannina, Department of Physics:
X. Aslanoglou.

Jaipur, India, Physics Department, University of Rajasthan:
A. Bharti, S.K. Gupta, R. Raniwala and S. Raniwala.

Jammu, India, Physics Department, Jammu University:
S.K. Badyal, A. Bhasin, A. Gupta, V.K. Gupta, S. Mahajan, L.K. Mangotra, B.V.K.S. Potukuchi, N.K. Rao and S.S. Sambyal.

JINR, Russia, Joint Institute for Nuclear Research:
P.G. Akichine, V.A. Arefiev, V.I. Astakhov, A. Baldina, A.A. Baldine, A.M. Baldine, V.D. Bartenev, B.V. Batiounia, I.V. Boguslavsky, Z.V. Borissovskaia, P. Bylinkine, A.V. Chabounov, G.S. Chabratova, I.A. Chichov, V. Danilov, V.I. Datskov, V.K. Dodokhov, L.G. Efimov, A.G. Fedounov, O.A. Golubitsky, B.N. Guouskov, O.I. Iouldachev, V.G. Kadychevsky, I.E. Karpunina, E.K. Koshurnikov, A.D. Kovalenko, A. Lioubimtsev, V.L. Lioubochits, V.I. Lobanov, G.I. Lykasov, E.A. Matiouchevski, K.V. Mikhailov, D.P. Mikhalev, I. Minaev, P.V. Nomokonov, A.N. Parfenov, I.V. Pouzynin, V.N. Pozdnyakov, A.B. Sadovski, A.E. Senner, I.A. Shelaev, A.V. Sidorov, N.V. Slavine, M.K. Suleimanov, G.P. Tsvineva, A.S. Vodopianov, M.B. Yuldasheva, S. Zaporozhets and A.I. Zintchenko.

V. Diomkin[7)], V. Kuznetsov[7)], V. Shestakov[7)], A. Vasiliev[7)] and A. Zhakovksy[7)].

Ts. Baatar[8)], B. Khurelbaatar[8)] and R. Togoo[8)].

K.G. Akhobadze[9)], A.K. Djavrishvili[9)], T. Grigalashvili[9)], E.S. Ioramashvili[9)], A.V. Kharadze[9)], L. Khizanishvili[9)], T.V. Khuskivadze[9)], L.V. Shalamberidze[9)] and N. Shubitidze[9)].

V. Djordjadze[10)], N. Grigalashvili[10)], Z. Menteshashvili[10)], M. Nioradze[10)], M. Tabidze[10)] and Y. Tevzadze[10)].

M. Bondila[11)], D. Felea[11)], A. Gheata[11)], M. Gheata[11)], M. Haiduc[11)], D. Hasegan[11)], R. Marginean[11)], R.I. Nanciu[11)] and S.I. Zgura[11)].

Jyväskylä, Finland, Department of Physics, University of Jyväskylä and Helsinki Institute of Physics:
J. Aysto, V. Ruuskanen and W. Trzaska.

Kharkov, Ukraine, National Scientific Centre ‘Kharkov Institute of Physics and Technology’:
G.L. Bochek, V.F. Boldyshev, I.F. Chervonny, A.N. Dovbnya, V.I. Kulibaba, N.I. Maslov, S.M. Potin, I.M. Prokhorets and A.F. Starodubtsev.

Kharkov, Ukraine, Scientific and Technological Research Institute of Instrument Engineering:
V.N. Borshchov, S.K. Kiprich, O.M. Listratenko, N. Mykhaylova, G. Protsay and V.E. Starkov.

Kiev, Ukraine, Department of High Energy Density Physics, Bogolyubov Institute for Theoretical Physics, National Academy of Sciences of Ukraine:
T. Hryn’ova, D.E. Kharzeev, V. Palshin, O. Pavlenko, A. Velytsky and G. Zinovjev.

Košice, Slovakia, Institute of Experimental Physics, Slovak Academy of Sciences and Faculty of Science P.J. Šafárik University:
J. Bán, J. Fedorišin, M. Hnatič, A. Jusko, B. Kocper, I. Králik, A. Kravčáková, F. Kriváň, I. Kuľková, M. Lupták, G. Martinská, B. Pastirčák, L. Šándor, J. Urbán, S. Vokál and J. Vrláková.

Legnaro, Italy, Laboratori Nazionali di Legnaro:
R.A. Ricci.

Lisbon, Portugal, Departamento de Física, Instituto Superior Técnico:
P. Branco, R. Carvalho, J. Seixas and R. Vilela Mendes.

Lund, Sweden, Division of Cosmic and Subatomic Physics, University of Lund:
L. Carlen, S.I.A. Garpman, H.-A. Gustafsson, P. Nilsson, A. Oskarsson, L. Osterman, I. Otterlund, D. Silvermyr and E.A. Stenlund.

Lyon, France, Institut de Physique Nucléaire de Lyon (IPNL), IN2P3-CNRS and Université Claude Bernard Lyon-I:
M.Y. Chartoire, M. Chevallier, B. Cheynis, E. Gangler, M. Goyot, J.Y. Grossiord, R. Guernane, A. Guichard, D. Guinet, G. Jacquet, P. Lautesse and S. Tissot.

Marburg, Germany, Fachbereich Physik, Philipps Universität:
F. Eckhardt, V. Friese and F. Pühlhofer.

Mexico City, Mexico, Centro de Investigación y de Estudios Avanzados:
R. Hernández Montoya, G. Herrera Corral, L. Magaña-Mendoza, H. Mendez and L.M. Montaño.

Moscow, Russia, Institute for Nuclear Research, Academy of Science:
K.A. Chileev, M.B. Goloubeva, F.F. Gouber, T.L. Karavitcheva, A.B. Kourepin, A.I. Maevskaia, V.I. Razine, A.I. Rechetine, N.S. Topilskaia and N.V. Zaikovskaya.

Moscow, Russia, Institute for Theoretical and Experimental Physics:
A.N. Akindinov, S.V. Boiarinov, V. Golovine, I.G. Grichouk, A.B. Kaidalov, M.M. Kats, I.T. Kiselev, S.M. Kisselev, E. Lioublev, M. Martemianov, A.N. Martemiyanov, P.A. Polozov, S.A. Pozdniakov, I. Roufanov, V.S. Serov, A.V. Smirnitski, M.M. Tchoumakov, I.A. Vetlitski, K.G. Volochine, L.S. Vorobiev and B.V. Zagreev.

Moscow, Russia, Russian Research Center 'Kurchatov Institute':
V. Antonenko, S. Beliaev, R. Cherbatchev, I. Doubovik, S. Fokine, M. Ippolitov, K. Karadjev, A.L. Lebedev, V. Lebedev, V.I. Manko, G. Mguebrichvili, T. Moukhanova, A. Nianine, S. Nikolaev, S. Nikouline, O. Patarakine, D. Peressounko, I. Sibiriak, A. Vasiliev, A. Vinogradov and M. Volkov.

Moscow, Russia, Moscow Engineering Physics Institute:
V. Grigoriev, V. Kapline, V. Loguinov and M. Strikhanov.

Münster, Germany, Institut für Kernphysik, Westfälische Wilhelms Universität:
D. Bucher, T. Peitzmann, K. Reygers, R. Santo, H. Schlagheck and M. Wahn.

Nantes, France, Laboratoire de Physique Subatomique et des Technologies Associées (SUBATECH), Ecole des Mines de Nantes, IN2P3-CNRS and Université de Nantes:
L. Aphecetche, A. Boucham, S. Bouvier, L. Conin, J.P. Cussonneau, H. Delagrange, D. D'Enterria, M. Dialinas, C. Drancourt, B. Erazmus, S. Giliberto, G. Guilloux, H.H. Gutbrod, M.S. Labalme, P. Lautridou, F. Lefèvre, M. Le Guay, L. Luquin, L. Martin, G. Martinez, V. Métivier, M.J. Mora, W. Pinganaud, A. Rahmani, O. Ravel, F. Retiere, C.S. Roy, D. Roy, Y. Schutz and A. Tournaire.

NIKHEF, The Netherlands, National Institute for Nuclear and High Energy Physics:
M. Botje[12)], A. Buijs[13)], J.J.F. Buskop[12)], A.P. De Haas[13)], P.K.A. De Witt Huberts[12,13)], R. Kamermans[12,13)], P.G. Kuijer[12,13)], D. Muigg[13)], G. Nooren[12)], C.J. Oskamp[13)], A. Van Den Brink[13)], N. Van Eijndhoven[13)] and J. Visschers[12)].

Novosibirsk, Russia, Budker Institute for Nuclear Physics:
A.R. Frolov, I.N. Pestov and M.A. Tiounov.

Oak Ridge, U.S.A., Instrumentation and Controls Division, Oak Ridge National Laboratory:
T. Awes, C.L. Britton, W.L. Bryan, J.W. Walker and A.L. Wintenberg.

Orsay, France, Institut de Physique Nucléaire (IPNO), IN2P3-CNRS and Université de Paris-Sud:
L. Bimbot, P.F. Courtat, R. Douet, P. Edelbruck, B. Genolini, H. Harroch, D. Jouan, L. Kharmandarian, Y. Le Bornec, M. Mac Cormick, J. Peyré, J. Pouthas, R. Sellem, E. Wanlin and N. Willis.

Oslo, Norway, Department of Physics, University of Oslo:
A.K. Holme, L.M. Ingebrigtsen, G. Løvhøiden, B. Skaali, T.S. Tveter and D. Wormald.

Padua, Italy, Dipartimento di Fisica dell'Università and Sezione INFN:
F. Antinori, F. Brandolini, N. Carrer, M. Morando, A. Pepato, F. Scarlassara, G. Segato, F. Soramel and R. Turrisi.

Prague, Czech Republic, Institute of Physics, Academy of Science:
J. Mareš, E. Mihoková, M. Nikl, K. Píška, K. Polák and P. Závada.

Protvino, Russia, Institute for High Energy Physics:
A.M. Blik, M. Bogolyubsky, G. Britvitch, S. Erine, G.V. Khaoustov, I.V. Kharlov, V.N. Kolossov, V. Lichine, M. Lobanov, N. Minaev, S.A. Sadovski, V.D. Samoilenko, P.A. Semenov, V.I. Suzdalev, V. Tikhonov and A. Zviagine.

Řež u Prahy, Czech Republic, Academy of Sciences of Czech Republic, Nuclear Physics Institute:
V. Hanzal, J. Hošek, I. Hřivnáčová, S. Kuschpil, V. Kuschpil, A. Kugler, V. Petráček, M. Šumbera, P. Tlustý, V. Wagner and D. Zákoucký.

Rome, Italy, Dipartimento di Fisica dell'Università 'La Sapienza' and Sezione INFN:
S. Di Liberto, M.A. Mazzoni, F. Meddi, D. Prosperi and G. Rosa.

Saclay, France, Centre d'Etudes Nucléaires, DAPNIA:
P. Ageron, A. Baldisseri, H. Borel, D. Cacaut, I. Chevrot, P. De Girolamo, J. Gosset, L. Gosset, P. Hardy, J.C. Lugol, F.M. Staley and Y. Terrien.

Salerno, Italy, Università di Salerno and Sezione INFN:
L. Cifarelli, B. Cozzoni, A. De Caro, G. Grella, M. Guida, A. Lavorato, J. Quartieri, G. Romano, A. Seganti, D. Vicinanza and T. Virgili.

Sarov, Russia, Russian Federal Nuclear Center (VNIIEF):
S. Abramovitch, V. Basmanov, V. Ianowski, R. Ilkaev, L. Ilkaeva, A. Ivanov, A. Khlebnikov, E. Kolokolnikov, V. Matiev, S. Nazarenko, V. Pounine, S. Poutevskoi, I. Selin, M. Tarasov, I. Vinogradov, S. Zhelezov and A. Zhitnik.

Shanghai, China, Shanghai Institute of Ceramics (SICCAS):
Q. Deng, P. Li, J. Liao, D. Yan and H. Yuan.

St. Petersburg, Russia, Institute for Physics of St. Petersburg State University, Mendeleev Institute for Metrology and Meson Scientific Association:
L.Y. Abramova, V.S. Alexandrov, V.M. Baratov, A.A. Bolonine, P. Bolokhov, M.A. Braun, V.M. Dobulevitch, G.A. Feofilov, O.N. Godissov, S. Guerassimov, S.N. Igolkine, M.I. Ioudkine, A.A. Kolojvari, V. Kondratiev, I.A. Novikov, S.V. Potapov, O.I. Stolyarov, T.A. Toulina, F.A. Tsimbal, F.F. Valiev, V.V. Vetchernine, L.I. Vinogradov and L.F. Vitouchkine.

Strasbourg, France, Institut de Recherches Subatomiques (IReS), IN2P3-CNRS and Université Louis Pasteur:
L. Arnold, J. Baudot, D. Bonnet, J.P. Coffin, G. Deptuch, M. Germain, C. Gojak, G. Guillaume, B. Hippolyte, F. Jundt, C. Kuhn, J. Lutz, A. Michalon and A. Tarchini.

Trieste, Italy, Dipartimento di Fisica dell'Università and Sezione INFN:
V. Bonvicini, L. Bosisio, P. Camerini, E. Fragiacomo, A. Gregorio, N. Grieo, G. Margagliotti, C. Piemonte, A. Rachevski, R. Rui, A. Vacchi and N. Zampa.

Turin, Italy, Dipartimenti di Fisica dell'Università and INFN:
G. Alberici, B. Alessandro, R. Arnaldi, S. Beolé, G. Bonazzola, E. Botta, L. Busso, D. Cavagnino, P.G. Cerello, E. Chiavassa, P. Cortese, E. Crescio, F. Daudo, N. De Marco, P. Deremigis, A. Feliciello, A. Ferretti, M. Gallio, G. Giraudo, P. Giubellino, A. Marzari-Chiesa, M. Masera, G. Mazza, P. Mereu, B. Minetti, O. Morra, A. Musso, D. Nouais, C. Oppedisano, A. Piccotti, G. Piragino, L. Riccati, E. Scomparin, L. Simonetti, F. Tosello, E. Vercellin, A. Werbrouck and R. Wheadon.

Warsaw, Poland, Soltan Institute for Nuclear Studies:
D. Czerwinski, A. Deloff, K. Karpio, S. Kozak, M. Kozlowski, L. Lukaszek, H. Malinowski, T. Siemiarczuk, G. Stefanek, L. Tykarski and G. Wilk.

Warsaw, Poland, University of Technology, Institute of Physics:
J. Grabski, M. Janik, P. Kindziuk, A. Kisiel, P. Leszczynski, A.M. Maliszewski, J.M. Mazur, T.J. Pawlak, P. Pery, W.S. Peryt, J. Pluta, M. Przewlocki, S. Radomski, A.M. Roszczewski, P. Skowronski, P. Stepien and P. Szarwas.

Wuhan, China, Institute of Particle Physics, Huazhong Normal University:
X. Cai, S.Q. Feng, Y. Hu, W. Li, F. Liu, F.M. Liu, H. Liu, L.S. Liu, Y. Liu, W.Y. Qian, S.Q. Wu, T. Wu, X.R. Wang, C.B. Yang, Z.B. Yin, D.C. Zhou and D.M. Zhou.

Yerevan, Armenia, Yerevan Physics Institute:
M. Atayan, R. Avakian, V. Danielyan, V. Gavalian, A. Grigorian, S. Grigoryan, H. Gulkanyan, R. Hakobyan, V. Kakoyan, Yu. Margaryan, S. Mehrabyan, L. Parlakyan, R. Shahoyan and H. Vardanyan.

Zagreb, Croatia, Ruder Bošković Institute:
D. Ferenc, A. Ljubičić and T. Tustonic.

---

[1] Also at CERN, Geneva, Switzerland
[2] On leave from JINR, Dubna, Russia.
[3] On leave from IHEP, Protvino, Russia.
[4] On leave from Budapest University, Hungary.
[5] On leave from Dipartimento di Fisica dell'Universitá and Sezione INFN, Padua, Italy.
[6] Institute of Physics, Pedagogical University, Kielce, Poland.
[7] Research Centre for Applied Nuclear Physics (RCANP), Dubna, Russia.
[8] Institute of Physics and Technology, Mongolian Academy of Sciences, Ulaanbaatar, Mongolia.
[9] Institute of Physics, Georgian Academy of Sciences, Tbilisi, Georgia.
[10] High Energy Physics Institute, Tbilisi State University, Tbilisi, Georgia.
[11] Institute of Space Sciences, Bucharest, Romania.
[12] Foundation of Fundamental Research of Matter in The Netherlands.
[13] Utrecht University, Utrecht, The Netherlands.

Acknowledgements

It is a pleasure to acknowldege the help of P. Bhaskar, S. Biagi, S. Haider, S. Iranzo, T.M. Lopez, S. Maridor, E. Morin, I. Smirnov and R. Veenhof in the preparation of this TDR. The collaboration wishes to thank all the technical and administrative staff involved during the preparation of this TDR. We also thank the staff from the Desktop Publishing Service for their professional help with the editing. This work is being supported by the Department of Atomic Energy and the Department of Science and Technology of the Government of India.

Contents

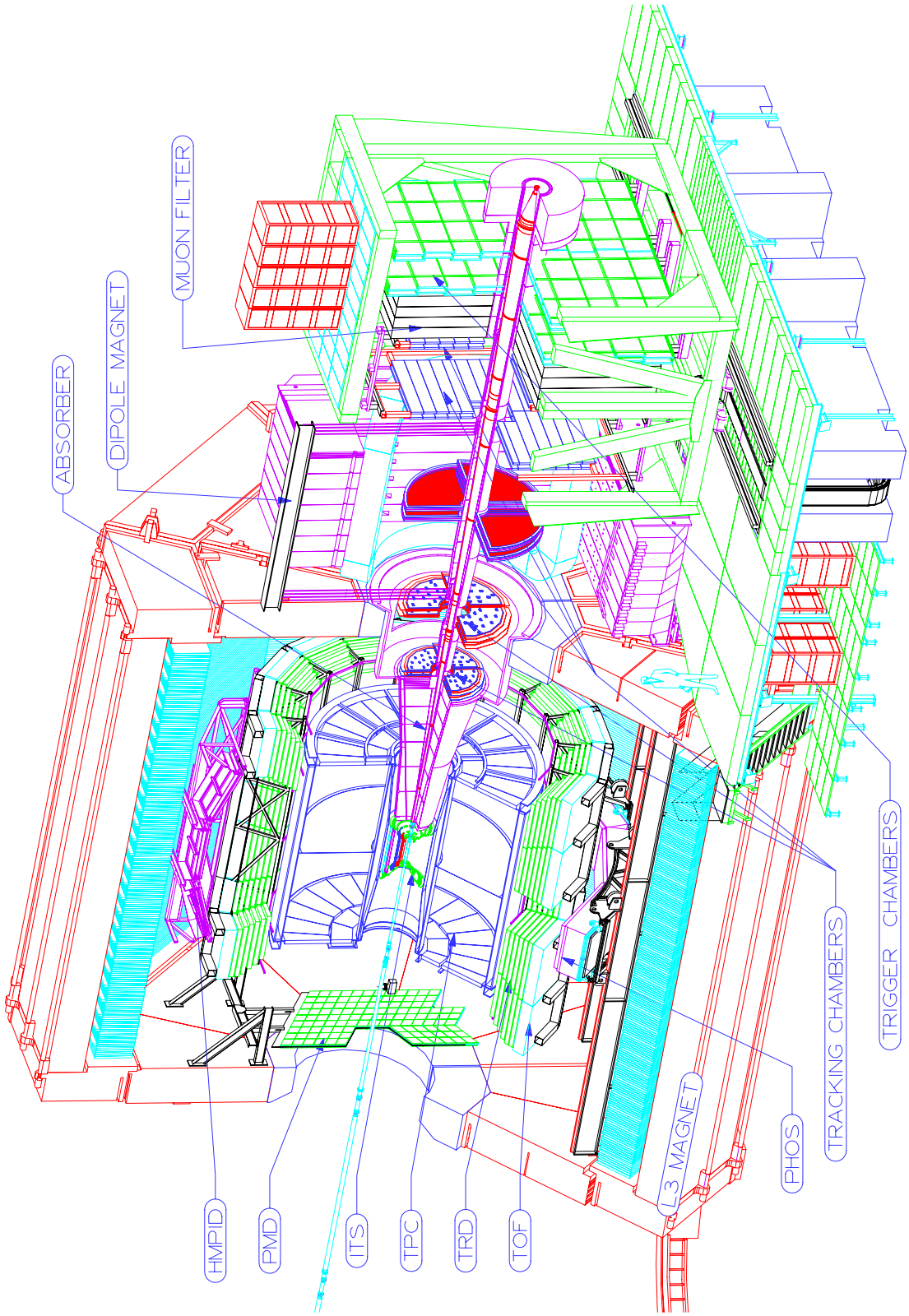

Colour Fig. I : Layout of the ALICE detector. The PMD is seen on the left attached to the magnet door.

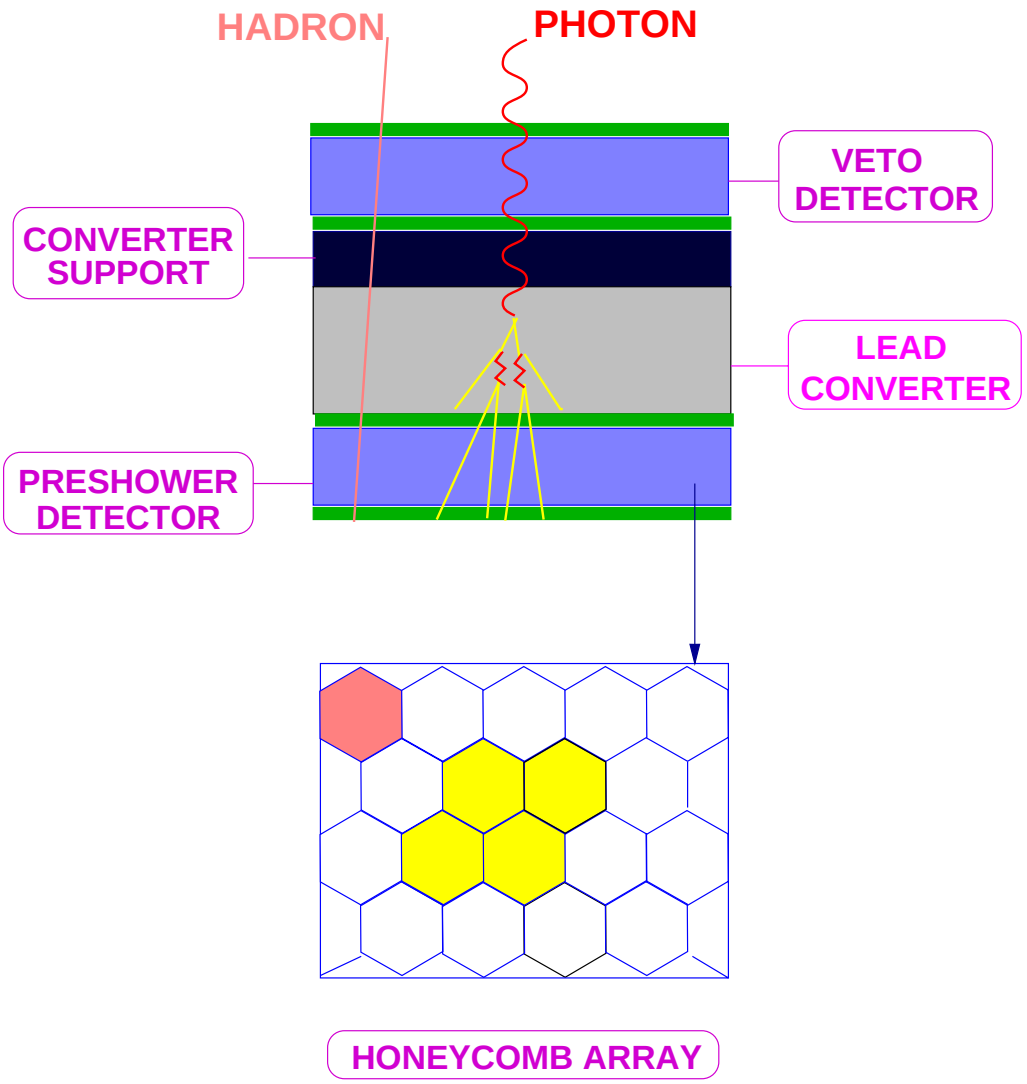

Colour Fig. II : Schematic illustration showing a hadron and a photon track passing through a converter and hitting the preshower detector. The hadron track hits only one cell; the photon track initiates a shower in the converter and hits several cells.

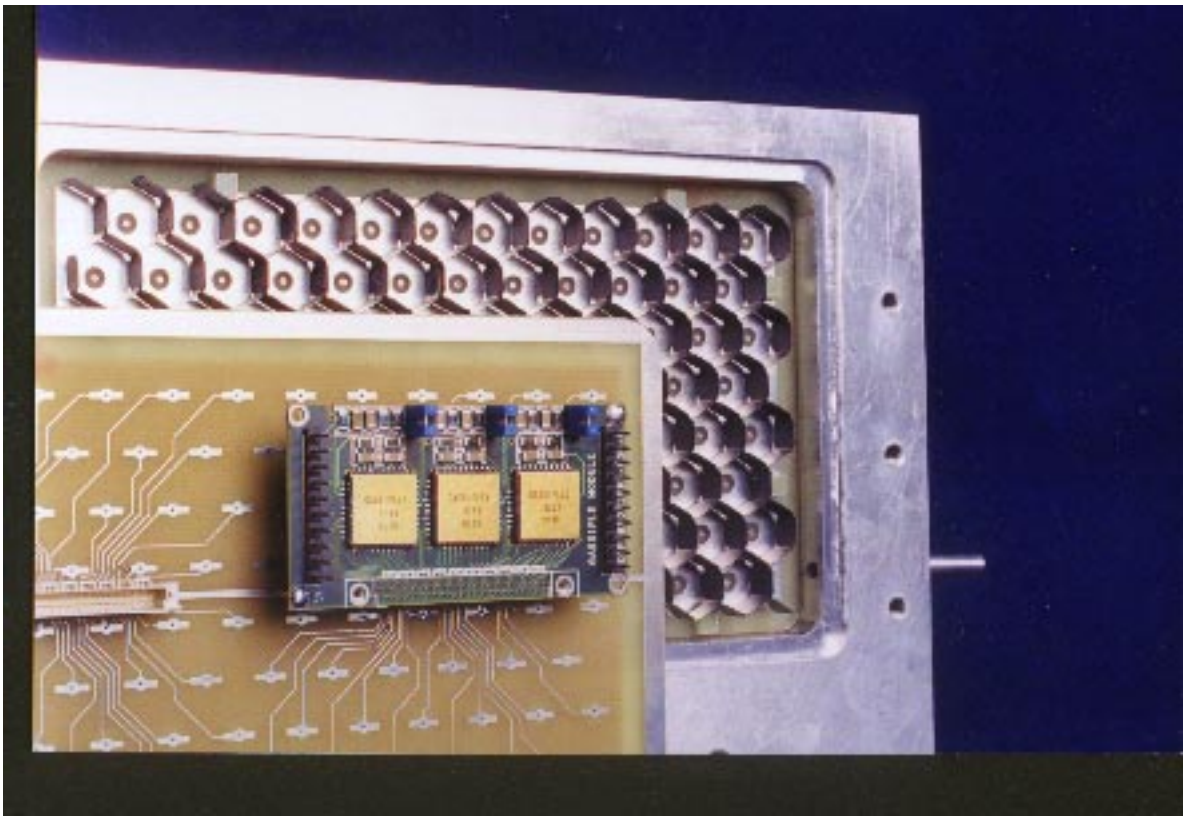

Colour Fig. III : Components of a prototype honeycomb chamber before assembly. The GASSIPLEX board is directly mounted on the chamber PCB.

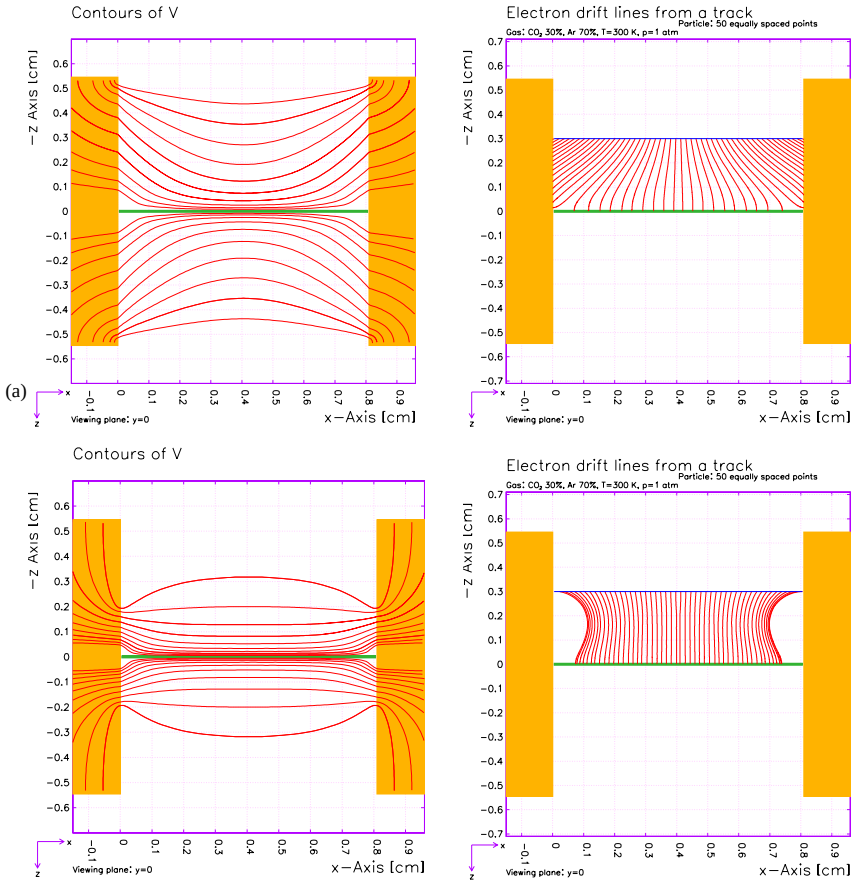

Colour Fig. IV : GARFIELD simulation results : (a) potential contours for open-geometry model, (b) electron drift lines for open-geometry model, (c) potential contours for extended-cathode model, and (d) electron drfit lines for extended-cathode model.

1 Introduction

1.1 The ALICE experiment

The ALICE (A Large Ion Collider Experiment) [1] experiment is designed for the dedicated study of heavy-ion collisions at the LHC in order to probe the deconfinement transition and chiral-symmetry restoration. The layout of the ALICE set-up is shown in colour Fig. I.

The main detector components of the experiment are the following.

- The central part, composed of detectors mainly devoted to the study of hadronic signals and di-electrons in the pseudorapidity range $-1 < \eta < 1$.
- The forward muon spectrometer, devoted to the study of quarkonia behaviour in dense matter.
- A set of multiplicity detectors and calorimeters, including a photon multiplicity detector (PMD) described in the present document. These detectors complement the central detectors in event characterization and in the study of critical phenomena associated with phase transition.

The basic motivation for including a PMD in the ALICE experiment is described in Ref. [1]. An important technical challenge to the experiment is imposed by the expected production of up to 8000 charged particles per unit of rapidity, at midrapidity, in central Pb+Pb collisions. This multiplicity dictates the granularity of the detectors and their optimal distance from the interaction point.

1.2 The photon multiplicity detector (PMD)

The PMD is a preshower detector having fine granularity and full azimuthal coverage in the pseudorapidity region $1.8 \leq \eta \leq 2.6$. It will be mounted on the L3 magnet door 5.8 m from the interaction point [2] on the opposite side of the dimuon spectrometer.

The principle of a preshower detector is schematically depicted in colour Fig. II. Photons passing through a converter initiate an electromagnetic shower and produce large signals on several cells of the sensitive volume of the detector. Hadrons normally affect only one cell and produce a signal representing minimum-ionizing particles. The thickness of the converter is optimized such that the conversion probability of photons is high and the transverse shower spread is small to minimize the shower overlap in a high-multiplicity environment. A preshower PMD having an array of plastic scintillator pads behind a 3 X_0 thick converter has already been used in SPS experiments to study sulphur- and lead-induced reactions [3, 4].

Figure 1.1 shows the cross-section and layout of the PMD schematically. The detector has a vertical axis of symmetry. The veto detector in front of the converter is used to reject charged particles. Both the preshower and the veto detectors are based on a honeycomb proportional chamber design. There are $\sim 2 \times 10^5$ cells in the entire detector, each cell having an area of 1 cm^2. The honeycomb wall forms a common cathode, operated at a high negative voltage. The signal is read out from the anode wires at ground potential using GASSIPLEX front-end electronics [5].

By measuring the multiplicity and spatial distribution of photons on an event-by-event basis, the PMD will be able to study event shapes and fluctuations in the forward region where large particle densities impose very severe constraints on the design of the detectors. Using the preshower signal the PMD will provide estimates of transverse electromagnetic energy [3].

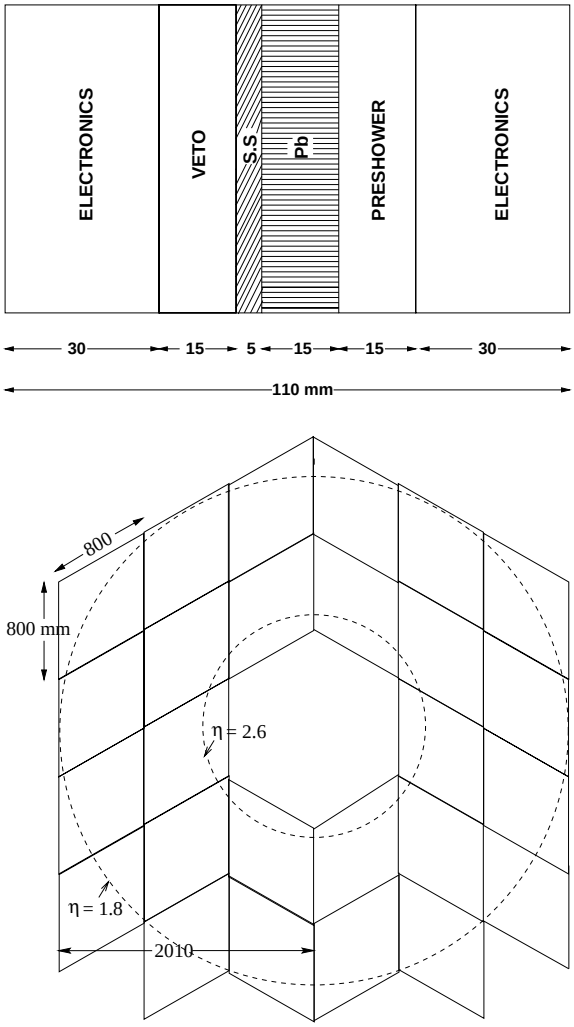

Figure 1.1: Top: Cross-section of the PMD (schematic only) showing the veto plane, lead converter and the preshower plane. SS is the support plate on which lead plates and chambers will be mounted. Bottom: The layout and the pseudorapidity coverage. Each rhombus denotes a supermodule of side 80 cm containing 72×72 hexagonal cells. The detector has a vertical axis of symmetry and the two halves can be opened independently.

1.3 Physics goals

1.3.1 Introduction

Using the measured observables in the PMD, investigations in the following broad topics of physics can be pursued:

- determination of the reaction plane and probes of thermalization via studies of azimuthal anisotropy and flow;
- critical phenomena near the phase boundary leading to fluctuations in global observables like multiplicity, mean transverse momentum and pseudorapidity distributions;
- signals of chiral-symmetry restoration (e.g. disoriented chiral condensates) through the measurement of charged-particle multiplicity ($N_{\rm ch}$) in a common part of phase space and study of the observables N_γ and $N_\gamma/N_{\rm ch}$ with full azimuthal coverage.

1.3.2 Azimuthal anisotropy and flow

Colliding nuclear matter emerges with a flow pattern that has its origin in the amount of incompressibility of nuclear matter or in the effect of mean fields. Collective flow manifests itself in altered event shapes which can be studied by measuring the momentum distribution of produced particles. A measurement of any section of the three-dimensional event shape reveals the momentum distribution at freezeout. There are suggestions that if flow occurs in the plasma state, then the subsequent hadronization may affect the kinematic quantities of different particle species differently. It is therefore desirable to measure the azimuthal anisotropy for different particle species in the final state. It is advantageous to study the event shapes with photons because their transverse distribution and that of the parent pions is not affected by the final-state Coulomb effects.

The asymmetric components of flow (directed and elliptic) are determined with respect to a reaction plane of the interacting system. Sophisticated techniques have been used to search for anisotropic patterns and the observed behaviour has been linked to phenomena such as softening of equation of state, nature of mean field interaction and also quark–gluon plasma formation [6–8]. Hydrodynamical models have shown that the magnitude of elliptic flow is sensitive to the initial spatial anisotropy and its subsequent evolution [9].

Photon multiplicity measurements using a preshower PMD have already been used to study collective flow at the SPS energies [10, 11] using the Fourier expansion technique. The full azimuthal coverage of the ALICE PMD and the large multiplicities observed will enable the determination of the reaction plane, even when the anisotropy present is very low [12]. The determination of the event plane improves with increasing flow and particle multiplicity. The determined event plane can be used to study the emission characteristics of various particle species as detected in other subdetectors of ALICE.

Centrality dependence of flow is shown to be sensitive to the equation of state, and has been shown to have different behaviours for a hadron gas and a quark–gluon plasma. Simulation results suggest that it will be possible for the PMD to determine flow in a wide range of centralities.

1.3.3 Disoriented chiral condensates

The formation of hot and dense matter in high-energy heavy-ion collisions has the possibility of creating a chiral-symmetry-restored phase in the laboratory. After the initial stage of the collision, the system cools and expands leading to normal QCD vacuum in which the chiral symmetry is spontaneously broken. During this process, a metastable state may be formed in which the chiral condensate is disoriented from the true vacuum direction. This transient state would subsequently decay by emitting coherent pions within finite subvolumes or domains of the collision region. This possibility of the formation of the disoriented chiral condensate (DCC) would lead to large imbalances in the production of charged and neutral pions. This topic has initiated a lot of enthusiasm in terms of theoretical understanding [13–20] and experimental searches [21–23]. Although not conclusively explained, the CENTAURO and anti-CENTAURO events observed in cosmic-ray experiments [24] remain possible candidates for large-scale charged-to-neutral fluctuations.

The primary signature of DCC is a large event-by-event fluctuation in photon to charged-particle multiplicity. This requires careful measurement of photons and charged particles in a common coverage. The challenge is to design sophisticated analysis tools on an event-by-event basis to identify DCC amidst the large background due to conventionally produced particles. Such studies have already been performed by using a preshower PMD and a set of charged-particle multiplicity detectors in the WA98 experiment [22, 23, 25–28].

The probability of DCC formation increases at the LHC energy with the increased prospect of creating a chiral-symmetry-restored phase. Its observation would signal the chiral transition as well as bring a wealth of information for understanding of QCD. The PMD, in conjunction with the forward multiplicity detector (FMD) measuring the multiplicity of charged particles in a common part of phase space, is well

suited to the search for signals of DCC formation. It should be able to effectively search for DCC by using different analysis methods outlined in Chapter 4.

Although the important signature for DCC would be obtained by photon and charged-particle measurements, the signals of DCC also appear in other observables such as p_T distribution of charged particles and photons, two-particle correlation (HBT) [29], dilepton signals [20, 30], and antibaryon production [31, 32].

Information can be obtained from the PMD and the FMD to tag interesting DCC candidate events, and the above signatures can be studied using other detectors in the ALICE experiment.

1.3.4 Event-by-event fluctuation

Fluctuations in global observables like multiplicity, $< p_{\rm T} >$ and $N_\gamma/N_{\rm ch}$ have received great attention recently [33–35] because of their usefulness in probing the critical phenomena accompanying the phase transitions. The analysis of single events with large statistics can reveal very different physics than studying averages over a large statistical sample of events. Recently, the NA49 Collaboration has presented a prototypical event-by-event analysis of fluctuations in central Pb+Pb collisions at 158 A GeV, which produces more than a thousand particles per event [36]. Similar results are also being investigated by the WA98 Collaboration. The multiplicities measured with the high granularity of PMD will be an excellent tool to study event-by-event fluctuations, even in smaller phase-space regions.

In a first-order phase transition, e.g. chiral-symmetry restoration, supercooling may lead to density fluctuations such as droplet formation and hot spots [37]. These will lead to large-scale rapidity fluctuations event-by-event. Such fluctuations can be easily detected using the PMD data, e.g. by the power spectrum method [38–40].

1.3.5 Relation with other ALICE detectors

The physics topics to be addressed by the PMD are closely interwoven with those of other ALICE detectors. The reaction plane determined from the PMD can be used to study flow parameters of various particle species in the TPC. While the azimuthal anisotropy can be determined independently using the PMD alone, a correlation between the anisotropy determined from the PMD and the FMD will be very useful to establish collective flow. One can study quarkonium suppression as a function of reaction plane in order to distinguish between rescattering effects and deconfinement as possible causes of suppression. The charged-particle multiplicity measurements from the FMD will be required to study DCC using the PMD.

The PMD will be able to take data in conjunction with both the central barrel detectors and the dimuon spectrometer to enable the above studies. This will also help to generate larger statistics for the PMD data which will be required to search for exotic events with low production rate.

1.4 Transverse electromagnetic energy

The ALICE experiment does not have any electromagnetic calorimeter of sizeable coverage, particularly in the forward region [1]. The PMD can be used to provide an estimate of the transverse electromagnetic energy $E_{\rm T}^{\rm em}$ using the measured preshower signals. Although there are large fluctuations in the energy deposited by individual photons in a preshower detector, the fluctuation substantially reduces when the energy deposition of a large number of particles are added together. For the preshower PMD, an estimate of $E_{\rm T}^{\rm em}$ can be given by the relation [3]

$$\hat{E}_{\rm T} = \sum_i \Delta E_i . \sin\theta_i \tag{1.1}$$

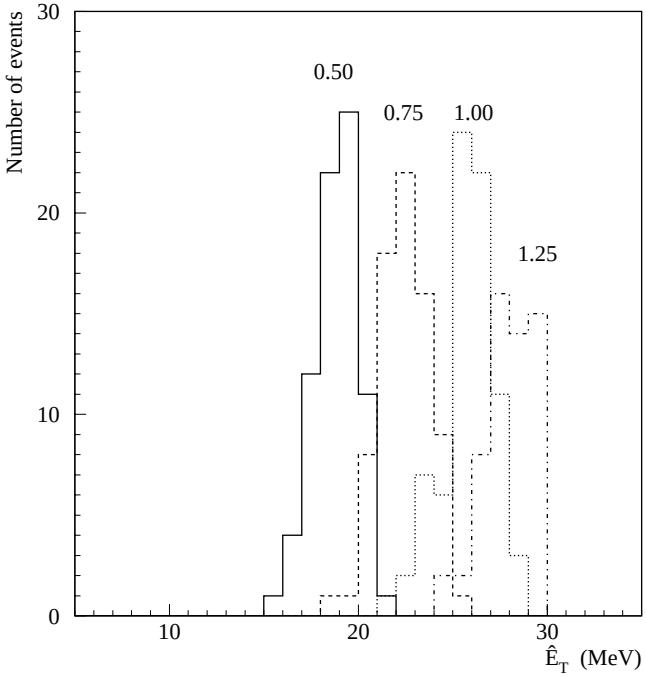

Figure 1.2: $\hat{E}_{\mathrm{T}}$ histograms for a set of central VENUS events. The different histograms represent the estimated $\hat{E}_{\mathrm{T}}$ when the $E_{\mathrm{T}}^{\mathrm{em}}$ values for the group of events have been modified by multiplying the momenta of all the particles in the event by the factor indicated above each histogram.

where θ_i is the angle at which the ith photon appears, ΔE_i is the energy deposited in the sensitive volume of the PMD by the ith photon, and the sum runs over all the observed photons. We denote $E_{\mathrm{T}}^{\mathrm{em}}$ measured by the PMD as $\hat{E}_{\mathrm{T}}$ to distinguish it from the calorimetric measurement of $E_{\mathrm{T}}^{\mathrm{em}}$. $\hat{E}_{\mathrm{T}}$ is found to be a small and constant fraction of $E_{\mathrm{T}}^{\mathrm{em}}$ [1].

The estimated $\hat{E}_{\mathrm{T}}$ value is expected to be sensitive to changes in the transverse energy in an event. In order to study the sensitivity of the preshower signal to variations in the $E_{\mathrm{T}}^{\mathrm{em}}$ in the event in an unambiguous way, we have modified a set of central Pb+Pb events obtained from the VENUS event generator [41]. The momenta of all the particles are multiplied by an arbitrary factor so that the transverse energy in the events is increased by the corresponding factor [42]. As the multiplicity of the group of events remains unaltered, the effect of this modification on the preshower signal should provide a measure of the sensitivity which is independent of multiplicity. The results obtained for the estimated $\hat{E}_{\mathrm{T}}$ are shown in Fig. 1.2 for several factors varying from 0.5 to 1.25. Each group is distinctly visible. The relative change in mean $\hat{E}_{\mathrm{T}}$ is found to be $\sim$50% of the change in $E_{\mathrm{T}}^{\mathrm{em}}$ of the event. The event-by-event fluctuation is found to be around 6% in all cases, including the fluctuation in input multiplicity.

1.5 General design considerations

1.5.1 Introduction

The forward region of the ALICE experiment is particularly suitable for a preshower photon detector because (a) the photon energies are large owing to rapidity boost, giving adequate detection efficiency, and (b) the area to be covered by the detector is within manageable and affordable limits. The PMD will be installed 5.8 m from the vertex, hanging from the L3 magnet door and covering the region $1.8 \leq \eta \leq 2.6$ on the opposite side of the dimuon spectrometer. This region has been selected to minimize

the effect of upstream materials like the beam pipe and the baseline detectors. This phase-space region also overlaps with the FMD.

1.5.2 Choice of detector technology

The PMD will use gas as the sensitive medium, as the other options are either too expensive (e.g. scintillator readout) or not compatible with ALICE baseline detectors [e.g. a silicon option placed close to the vertex resulted in increased background into the Time Projection Chamber (TPC)]. The choice of detector technology for use in a preshower detector is dictated by the considerations that (a) charged particles should be confined preferably to one cell; (b) low-energy δ-electrons should be prevented from travelling to nearby cells and from causing crosstalk among adjacent channels; (c) the technology should be amenable to modular design with minimum dead space at the boundaries; and (d) the detector should be placed in contact with the converter without large air gaps.

After surveying various technologies in the field of gas detectors, we have selected a novel design having honeycomb structure and wire readout. The honeycomb cells are physically isolated from each other by thin metallic walls to contain δ-rays. The metallic wall of the honeycomb forms the common cathode and is kept at a large negative potential. The individual anode wires in the cells are kept at ground potential and connected to the readout electronics.

The honeycomb geometry is selected because of its closeness to a circular approximation, providing almost circular equipotentials within a cell. This geometry also facilitates close packing of large arrays. The same design can be used for both the preshower part and the charged-particle veto. The photograph in colour Fig. III shows the components of a prototype honeycomb chamber.

The operating gas in the chamber is selected to be a mixture of Ar and CO_2 because of its insensitivity to neutrons and its non-inflammable nature.

1.5.3 Granularity and converter thickness

The granularity of the PMD is determined by the consideration of highest particle multiplicity in the event. The cell size is selected such that the occupancy be within 15%, which allows clustering of hits and reconstruction of photons. For an acceptance of the PMD extending to within one unit of pseudorapidity, a uniform cell size of 1 cm^2 has been selected. The granularity of the veto has been kept identical to that of the preshower part.

The optimized converter thickness is found to be 3 X_0 as in previous preshower detectors [3, 4]. The basic physical parameters of the PMD are summarized in Table 1.1.

Table 1.1: Basic parameters of the PMD

Parameter	Value
Distance from vertex	580 cm
η-coverage	1.8–2.6
Active area	10 m^2
Inner radius	85 cm
Outer radius	200 cm
Cell size (area)	1 cm^2
Cell depth (gas depth)	8 mm
Number of channels	200,000

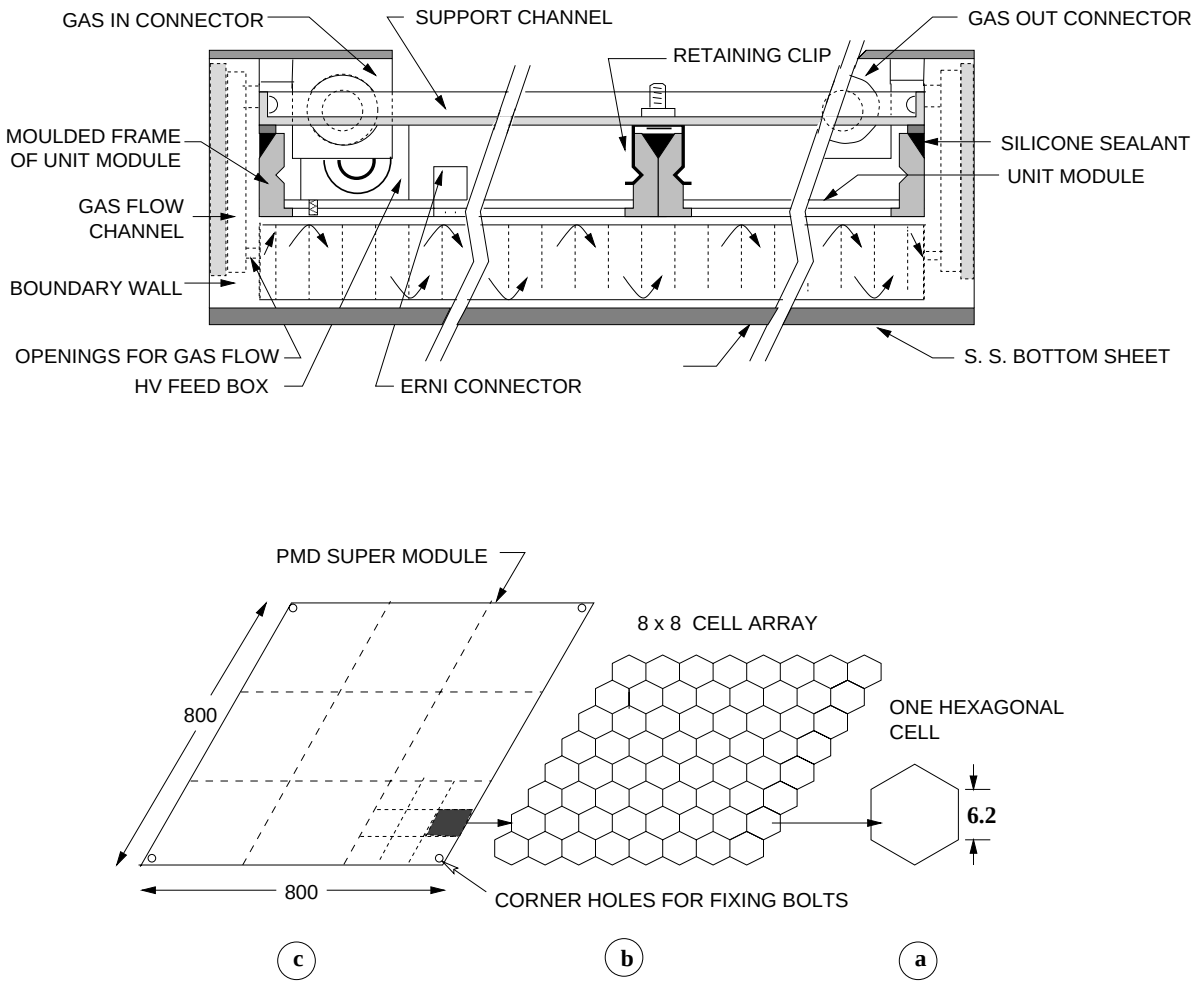

Figure 1.3: Schematic view of a PMD supermodule showing details of unit module placement and gas tightness inside the supermodule. The bottom part shows the components: (a) a single cell, (b) an array of 8×8 cells for connection to the front-end electronics, and (c) the 3×3 unit modules within a supermodule.

1.6 Overview of the PMD design and main R&D results

1.6.1 General structure of the PMD

A technical design of the PMD will be presented in Chapter 3. The detector is fabricated in the form of unit modules having dimensions which are convenient to handle during assembly. The unit module consists of 24×24 hexagonal cells in a rhombus array. The rhombus shape of a honeycomb array provides minimum dead space at the boundaries. A set of 3×3 unit modules are contained within a supermodule. Each supermodule is a rhombus of side 80 cm and provides a gas-tight enclosure. A schematic view of a supermodule is shown in Fig. 1.3.

1.6.2 R&D, prototype and test results

Several configurations of the honeycomb chambers have been tested in beams during 1998–1999 to study the response to minimum-ionizing particles (MIPs) and electrons. The prototypes having a matrix of 96 cells were constructed using thin (0.1–0.2 mm) copper sheets. An earlier prototype had the cathode in the

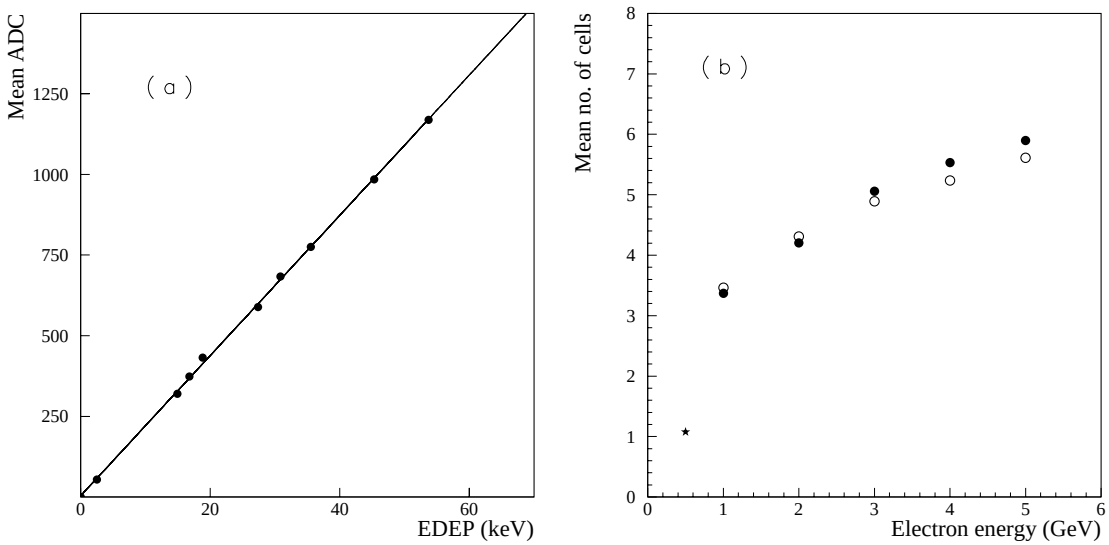

Figure 1.4: (a) Average pulse height (ADC) vs. energy deposition (EDEP), deduced from simulation, for various preshower cases studied using prototype-99-8 at 1465 V. (b) Comparison between test data and simulations for the average number of cells fired in a preshower as a function of electron energy. Solid circles denote the test data and open circles are simulation results. The asterisk denotes the average number of cells fired by 7 GeV pions.

form of an open hexagonal tube. In this case the efficiency for charged-particle detection was found to drop substantially near the boundaries of the hexagon. In a subsequent prototype, designed after studies of field distribution within the cell, the cathode plane was extended on the inner side of the PCB to 2 mm from the anode wire. This is referred to as the extended-cathode type. The operating voltage varied around 1400 V for the extended-cathode chamber using a mixture of Ar and CO_2 gas in the ratio 70:30. This prototype provided almost uniform efficiency throughout the cell volume. The details of prototype fabrication and test results are described in Chapter 2.

The test results suggest that the efficiency for MIP detection is almost uniform within the cell and approaches a value close to 98%. The signal of individual charged particles is almost always confined to one cell. The relative gains of the cells have been studied by scanning about half of the cells in the prototype. The response is quite uniform, the distribution of relative gains having a width (σ) of 6%.

The tests for preshower behaviour have been done using electron beams at several energies and using several converter thicknesses. Figure 1.4(a) shows the relation between the average pulse height (in ADC units) for an operating voltage of 1465 V and the average energy deposition (EDEP) obtained from the GEANT simulations [43]. The behaviour of the detector and the readout electronics is found to be quite linear.

The average number of cells fired in test runs and in simulations for electrons at various energies passing through a 3 X_0 thick lead converter is shown in Fig. 1.4(b) as a function of electron energy. The test data are found to be in close agreement with those given by the GEANT simulation. This is a very important result and represents a marked improvement over the WA98 PMD case where the preshower size in test data was about twice that of simulation data, and the signal due to MIPs was spread to three pads as opposed to one in simulation. The present design should thus help in handling the large multiplicity at the LHC energy.

The dynamic range of the GASSIPLEX chip, available in the 0.7 μm technology version, has been estimated by measuring the level of saturation observed in test data. It is found that the electronics can handle the signal produced when the maximum energy deposition in one cell is in the range of 60–75 keV, depending on the operating voltage. The percentage of cells where the energy deposition may exceed

this value in the actual experiment, as found from the VENUS + GEANT simulations, will be $\sim 0.4\%$.

1.6.3 Readout electronics

The PMD will use the new version (MANAS-16) of GASSIPLEX as front-end electronics based on the scheme used for the tracking chambers of the muon spectrometer [44]. An array of 8×8 cells will be connected with a multi-chip module (MCM). A set of MCMs will be read out using Digital Signal Processors (DSPs). The total time of data transfer to the DSP will be ≤ 100 μs. Using full trigger rate, the PMD will generate data at the rate of ~ 63 Mbyte/s.

1.6.4 Detector performance

The performance of the PMD has been simulated for various event centralities in Pb+Pb collisions and also using various physics processes relevant for the PMD-related signals as described in detail in Chapter 4.

The reconstruction of photons is done by clustering the hits on the preshower plane. Hadrons are rejected by employing a neural-network algorithm using signals in both the veto and preshower planes. The main results on the performance of the detector are given below.

- The efficiency of the PMD for counting photons has been estimated using simulations. For central Pb+Pb collisions we obtain values of 73% and 68%, respectively, for the cases of PMD only and with all detectors and beam pipes in the actual ALICE environment. The corresponding values of the purity of the photon sample are 75% and 61%.

- The PMD can provide an estimate of $E_{\rm T}^{\rm em}$. The resolution of the $\hat{E}_{\rm T}$ value for the entire PMD acceptance is $\sim 3\%$ for fixed multiplicity. The fractional change in $\hat{E}_{\rm T}$ obtained using the preshower signal is found to be $\sim 50\%$ of the change in the transverse energy in the event.

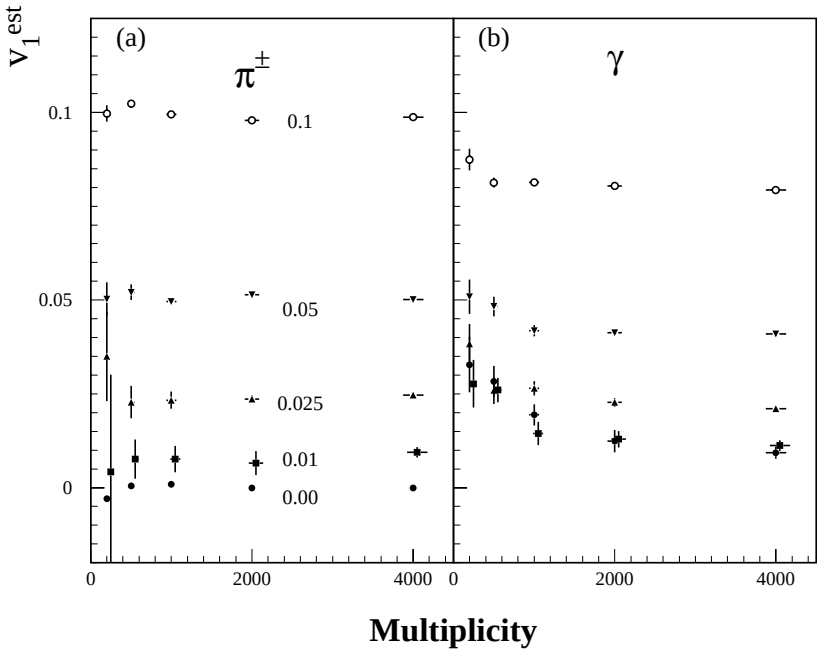

Figure 1.5: Multiplicity dependence of $v_1^{\rm est}$ (the estimated values of v_1) for various input values for (a) charged particles and (b) photons. The numbers in the left panel are the input values of v_1.

- It is possible to discern the anisotropy of the event shapes in the ALICE environment for anisotropies as low as $\sim 2\%$ [12]. The simulation results for the estimated value v_1^{est} of the flow parameter v_1 for photons are shown in Fig. 1.5 for various input values. For comparison the results for charged particles are also displayed. The anisotropy observed with photons is slightly less than that for charged particles. It will be possible to estimate the flow signal in the parent pions by measuring the signal in photons. The estimated flow does not significantly depend on the photon counting efficiency so long as the multiplicity is reasonably high. The resolution correction factor for the determination of event planes approaches unity for the multiplicities expected to be encountered in central Pb+Pb collisions within the PMD acceptance. The determination of the event plane will enable an investigation of any correlated emission of other particle species in different phase-space regions.

- Even with limited acceptance the PMD can study event-by-event pseudorapidity fluctuations using the power spectrum technique. It will be possible to select events having non-statistical fluctuations at the 1% level of admixture in normal events. Multiplicity fluctuations of photons for different impact parameters and colliding systems can be determined to a high accuracy. These can be compared to predictions from theoretical models. By comparing these to known theoretical models one will understand the possible interesting physical effects.

- It is possible to detect signals of the formation of DCC primarily in conjunction with the FMD and also with other central detectors. Sophisticated analysis methods using wavelet techniques, robust observables and power spectrum have already been developed and shown to be sensitive to an identification of DCC signals.

2 R&D, prototypes, test results

The design of the PMD has evolved through several stages of simulation studies and prototype tests. The initial results can be found in Refs. [1–3]. The detector is based on a honeycomb proportional chamber design. The present chapter describes the results of simulation studies for the optimization of cell geometry, material, and thickness in the first section. The prototype fabrication, test set-up, and results are described in the next two sections. The calibration procedure for the detector, combining the test beam and simulation results, is described in the last section.

2.1 Design and simulation

2.1.1 Simulation tools

In order to optimize the detector parameters and to study the preshower evolution, the response of the detector has been studied by tracking charged particles and photons through the detector medium using the ALICE version of the GEANT simulation package [4]. The implementation of the PMD set-up in the AliRoot configuration is described in Chapter 4.

2.1.1.1 Single particle simulation

GEANT simulations were carried out using single particle cases (photons, electrons and charged pions) to optimize the parameters of the honeycomb cells and to understand the results of the prototype tests. The geometry of the prototype chamber was especially included in the AliRoot PMD implementation for single-particle simulation.

2.1.1.2 Simulation with event generators

To optimise the pseudorapidity coverage and granularity, we used events that were generated using VENUS [5] and parametrized multiplicity and kinematic distributions from HIJING [6], as described in Ref. [3]. These simulations were also used to extrapolate the results of prototype tests carried out with electrons to those of photons produced in actual heavy-ion collision events, as discussed in Section 2.4.4.3.

2.1.2 Detector specifications

2.1.2.1 Preshower part

The choice of detector technology for use in a preshower detector was based on the following considerations:

- the active volume of the detector should be thin and very close to the converter so that the transverse spread of the shower is minimized;
- low-energy δ-electrons should be prevented from travelling to nearby cells and causing significant crosstalk among adjacent channels;
- the technology should be amenable to modular design with a minimum of dead spaces at the boundaries and should not require a staggered layout;
- the detector material (gas) should be insensitive to neutrons. In a hydrogeneous medium neutrons tend to produce large signals due to recoil protons, which can mimic a photon signal;

- the technology should permit the construction of large chambers. Large chambers are needed in order to minimize the total number of chambers for the given coverage, so that the splitting of clusters at the box boundaries is minimized.

2.1.2.2 Charged particles

The considerations for charged particles are the following:

- the charged particles should be confined preferably to one cell so that the occupancy does not increase significantly. If the signal spreads to neighbouring cells then there is a significant probability of vetoing nearby photons.
- the efficiency of detection should be high ($> 95\%$) so that the same technology can be used for both the preshower and the veto parts.

2.1.2.3 Survey of existing technologies

The conventional technology of gas detectors employs large uniform gas volume with cathode pad readout. In this scheme charges are invariably induced at neighbouring pads, causing the number of pads affected by a charged particle to be more than one. Hence this technology cannot be used in the high multiplicity of the forward region.

Large-area cathode pad chambers also require support for the cathode planes (usually a few centimetres thick Rohacell-type material), which would increase the distance between the converter and the active volume of the detector, thereby affecting the performance of the preshower detector.

Segmentation of the gas volume with material separation becomes necessary to reduce the effect of δ-rays. Some attempts have been made to develop cellular proportional chambers with wire readout [7, 8]. However, these schemes do not suit our requirements of small gas thickness, field homogeneity, and material thickness.

2.1.2.4 The present design

We have selected a design with a honeycomb structure and a wire readout, as shown schematically in Fig. 2.1. The honeycomb geometry was selected to provide almost circular equipotentials within a cell. This geometry also facilitates the close packing of large arrays. The cells are physically isolated from each other by thin metallic walls in order to contain δ-rays. It was found that in an unsegmented uniform gas volume the preshower signal extends to a large number of cells [1],

The honeycomb body forms the common cathode and is kept at a large negative potential. It also supports the printed circuit boards (PCBs). The individual anode wires in the cells are grounded through the input channels of the readout electronics.

The present design of the proportional chamber is novel in its scheme of using a honeycomb cathode. In a normal proportional chamber the long wire length compared to the diameter of the tube minimizes the edge effects. In the present case the gas thickness is comparable to the cell size. This necessitates a special design of the cathode and field shaping to enable most of the ionization in the gas to be collected at the anode.

2.1.2.5 Choice of honeycomb material and thickness

The choice of material and the thickness for the honeycomb cells were dictated by the following considerations:

- The material should help to reduce the transverse size of the preshower by containing low-energy electrons moving at large angles;

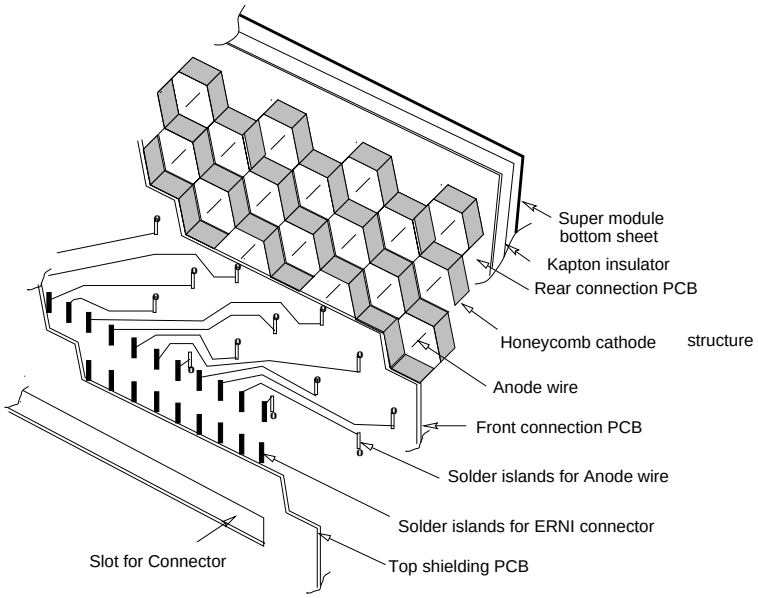

Figure 2.1: Schematic design of the honeycomb chamber.

- The thickness should be kept low to avoid large amounts of material;
- It should be easy to fabricate or to procure commercially.

The results of simulation for different materials and thicknesses are summarized in Fig. 2.2 for a range of photon energies. It was found that (a) compared to low-density materials like plastic and aluminium, the use of higher-density materials like iron and copper helps to reduce the average number of cells in a preshower by 30% to 50%, depending on photon energy, and (b) the transverse shower size decreases with increasing thickness of the cell wall and then reaches a plateau for lower photon energies around a thickness of 0.4 mm. As the average energy of photons emitted in Pb+Pb collisions within the PMD acceptance, as given by the VENUS event generator, is ~ 2 GeV, we selected a 0.4 mm wall thickness as the optimum choice for cell fabrication. Copper was selected as the material for the honeycomb chambers because of its non-magnetic nature. It can be shaped easily and it is very good for soldering the joints.

2.1.3 Cell modelling

2.1.3.1 Introduction

The PMD is an array of close-packed hexagonal cells. The small dimensions and large aspect ratio make these cells quite unconventional. Modelling of the cell was carried out to understand the electric field within the cell and to maximize the charge collection at the anode.

All simulations were carried out with the help of GARFIELD [9], a computer program for detailed simulation of drift chambers. GARFIELD interfaces with MAXWELL [10] in the input stage to obtain the field maps.

2.1.3.2 The first model

The first model is based on the results of two-dimensional simulations performed in the early phase of the design studies [11]. Subsequently, three-dimensional simulation was carried out with later versions of GARFIELD.

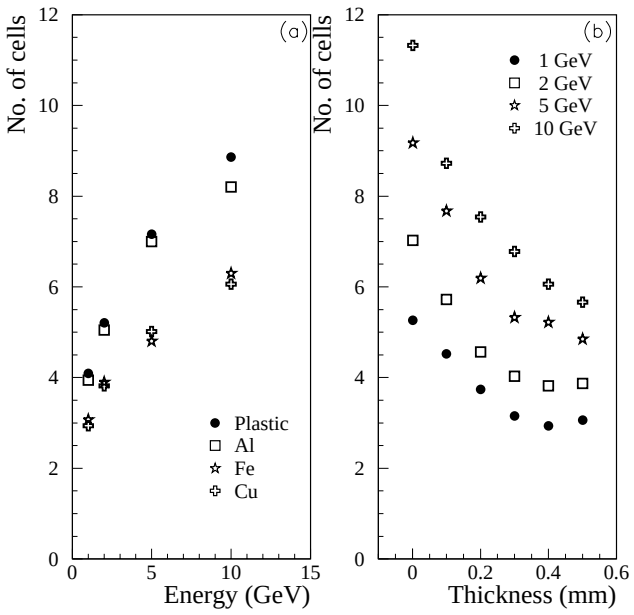

Figure 2.2: (a) The transverse shower size of photons at different energies for a 0.4 mm thick cell wall of different materials; (b) The average number of cells affected as a function of the cell wall thickness of copper for various photon energies as labelled.

Each detector cell is a tubular hexagonal chamber (as shown in Fig. 2.3) with a wire along the tube axis. The cell volume is filled with an Ar + CO_2 gas mixture and is sealed by G10 plates which provide soldering contact for the wire and the readout electronics. The cell is covered by a thin copper-clad G10 plate for proper grounding. Being an open tube structure, this model is referred to as the 'open geometry model'.

The cell acts like a proportional counter. When a charged particle traverses the gas medium, it ionizes the gaseous molecules. The primary electrons, thus generated, drift towards the wire, leading to an avalanche very close to the wire. This produces the signal.

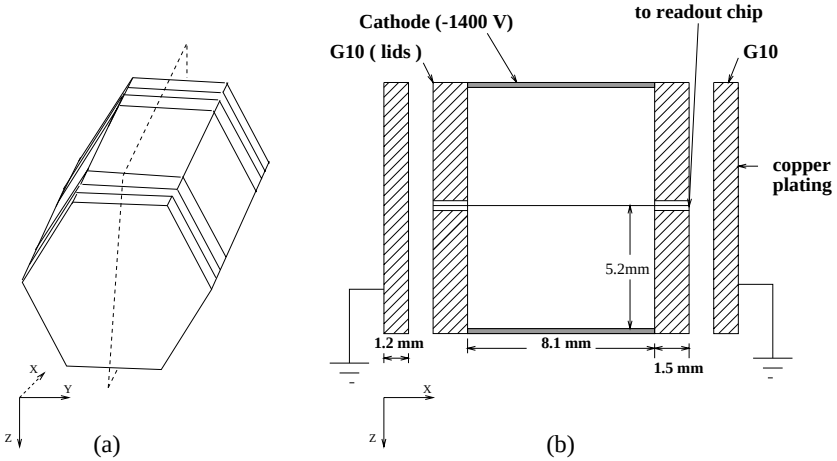

Figure 2.3: Schematic picture of a unit cell with open geometry and the longitudinal cross-section of the cell.

Table 2.1: Parameters of the unit cell

Cell radius (typical)	6 mm
Cell depth (typical)	8 mm
Radius of anode wire	10 μm
Thickness of inner G10 plates (the 'lids')	1.5 mm
Thickness of the outer G10 plates	1.2 mm
Gap between two G10 plates	1.2 mm
Dielectric constant of G10 (F4 epoxy)	4.4
Thickness of cell wall	0.2 mm
Anode wire support (dia.)	0.5 mm
Anode wire support (length)	1.5 mm
Cathode potential	-1400 V

2.1.3.3 Implementation of the unit cell

The parameters of the unit cell are given in Table 2.1. The detector cell is modelled in MAXWELL according to these parameters. Because of the six-fold axial symmetry of the cell and a mirror symmetry in the plane perpendicular to the tube axis, only 1/12 of the whole cell was modelled in MAXWELL. The field maps for the entire cell were then generated by GARFIELD using the symmetry considerations.

Several combinations of cell radii and depths were tested. The results presented here correspond to a cell of 6 mm radius and 8 mm depth.

2.1.3.4 Field distribution in an open geometry cell

Using the field maps from MAXWELL as input, the equipotential lines in the *xz*-plane for the complete cell was obtained using GARFIELD, as shown in colour Fig. IV(a). The orange bars are the projection of the 'lids' described in Table 2.1. The wire is along the *x*-axis and the tube walls (cathode) are 5.2 mm away from the wire. The difference between successive potential contours is 100 V.

It was observed from the contours that, because of a large aspect ratio, the edge effects dominate inside the drift region. This makes the contours convex instead of parallel as would have been the case for an ideal and infinitely long cylindrical chamber. This results in a leakage of flux on to the lids.

This is further illustrated by the drift-line plot for electrons. Colour Fig. IV(b) shows the drifting of electrons originating from 50 equally-spaced points in the drift space along a track typically at $r = 3$ mm from the anode wire. The red lines correspond to the drift lines of electrons. One observes that a large number of drift lines end on the 'lids' instead of going to the wire. This implies a substantial loss in the collection of primary electrons, which leads to a loss of efficiency for charged-particle detection. This necessitated a modification of the cell geometry to achieve better field uniformity.

2.1.3.5 Model with extended cathode

Guard rings have been traditionally used for field shaping. In the present case these could have been implemented using multilayer PCBs. A simpler variant of the guard rings was to extend the cathode from the cell walls on the G10 surface inside the gas volume towards the anode wire, making a box-like structure. This option could be implemented using double-sided single-layer PCBs which are easier to handle and also much cheaper compared to multilayer PCBs. This motivated us to perform a simulation study of such a model.

The cross-sectional view of the extended cathode model is shown in Fig. 2.4. Here the cathode has been extended to 2 mm from the wire on the inner surface of the lids. The thickness of the extended

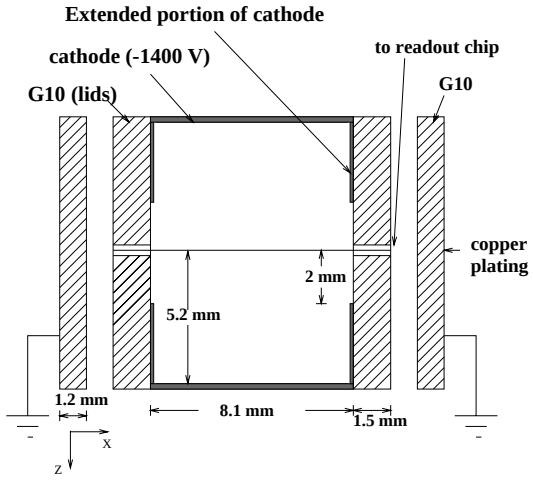

Figure 2.4: Cross section view of the model with extended cathode

portion of the cathode was taken as 50 μm. The other parameters of the unit cell were identical to those contained in Table 2.1.

2.1.3.6 Field distribution in the extended cathode cell

The potential contours are shown in colour Fig. IV(c). The equipotential lines are almost parallel near the wire and concave at larger distances. This suggests that electrons are now focused into the drift medium. Colour Fig. IV(d) shows the electron drift lines for a track at a distance of 3 mm from the wire. Here we observe that most of the ionization electrons are collected on the wire.

Figure 2.5(a) shows the electric field strength in the drift medium 3 mm from the anode wire for the two models. Whereas for the open geometry model the field varies by a factor of $\sim$2 along the length of the wire, it is quite homogeneous for the extended cathode model.

2.1.3.7 Timing characteristics

One of the important aspects of the charge collection is its typical time-scale. This allows us to judge the suitability of the readout electronics.

For a gas mixture of 70% Ar and 30% CO_2 the drift time graph is shown in Fig. 2.5(b) for a track 5 mm away from the anode in the case of the extended cathode model. There is a slight asynchrony in the arrival time of the drift electrons from the same track. This is due to the non-uniform radial field inside the cell owing to its typical geometry. The drift time is longer for the electrons originating near the lids, compared to the ones starting from the middle of the drift region.

For a cathode potential of -1400 V, the simulation shows the slowest drift time to be $\sim$ 500 ns for a track 5 mm away from the wire. For electrons originating in the plane of the longest diagonal, the largest drift time is found to be $\sim$ 750 ns. The fraction of such slow tracks over the whole volume of the cell is rather small, and these are still within the acceptable limits of the readout electronics as will be described in Chapter 3.

2.2 Prototypes

2.2.1 Single-cell prototype for laboratory tests

Single hexagonal cells of varying depths were fabricated, with and without extended cathode geometry, for laboratory tests with radioactive sources. The cell was housed in a thin gas-tight chamber (see

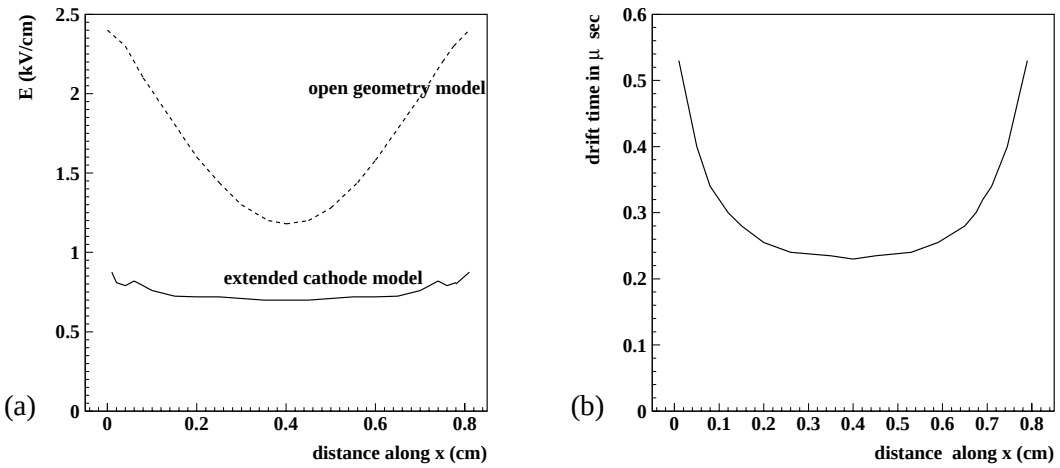

Figure 2.5: (a) Electric field graphs for the open geometry and for the model with the extended cathode. (b) Drift time for extended cathode model for a track 5 mm from the anode.

Fig. 2.6). The perspex lid of the chamber had a small Mylar foil window for the β-rays and X-rays to enter the cell. The anode was connected to a positive high voltage and the cathode was kept at ground potential. The signal was processed using standard NIM electronics and recorded on a MCA.

Extended cathode single cells were made in the laboratory by covering the open ends of the single cells with printed circuit boards (copper side inwards) and by electrically connecting the boards with the cathode. The boards had 4 mm dia. holes along the axis of the cell and tiny G10 supports were attached radially to the hole to give axial support to the anode wire.

2.2.2 Honeycomb prototypes

The honeycomb prototypes fabricated for R&D and tests consisted of 96 cells. The number of cells in the prototype were kept moderate to keep the cost of the readout electronics low. However, this was adequate for the study of preshower characteristics and cell-to-cell variation of gains and efficiencies. The construction of prototype chambers involved the following stages.

2.2.2.1 Fabrication of the honeycomb matrix

Copper strips of proper width were prepared by photochemical machining so that notches were produced on both sides at regular intervals (see Fig. 2.7). These were shaped in the form of a half-honeycomb using a precision-machined hexagonal jig. Joining two such half-honeycomb strips by spot-soldering produced a row of hexagonal cells. In this scheme four sides of the hexagon have a thickness equal to the original thickness of the strip and two sides have double the thickness. In the final shape, notches appeared on all sides of the hexagonal cells. This facilitated a smooth gas flow within all the cells in the chamber. The honeycomb matrix was then cleaned with a soap solution and coated with graphite paint to improve the ageing properties and suppress after-pulsing.

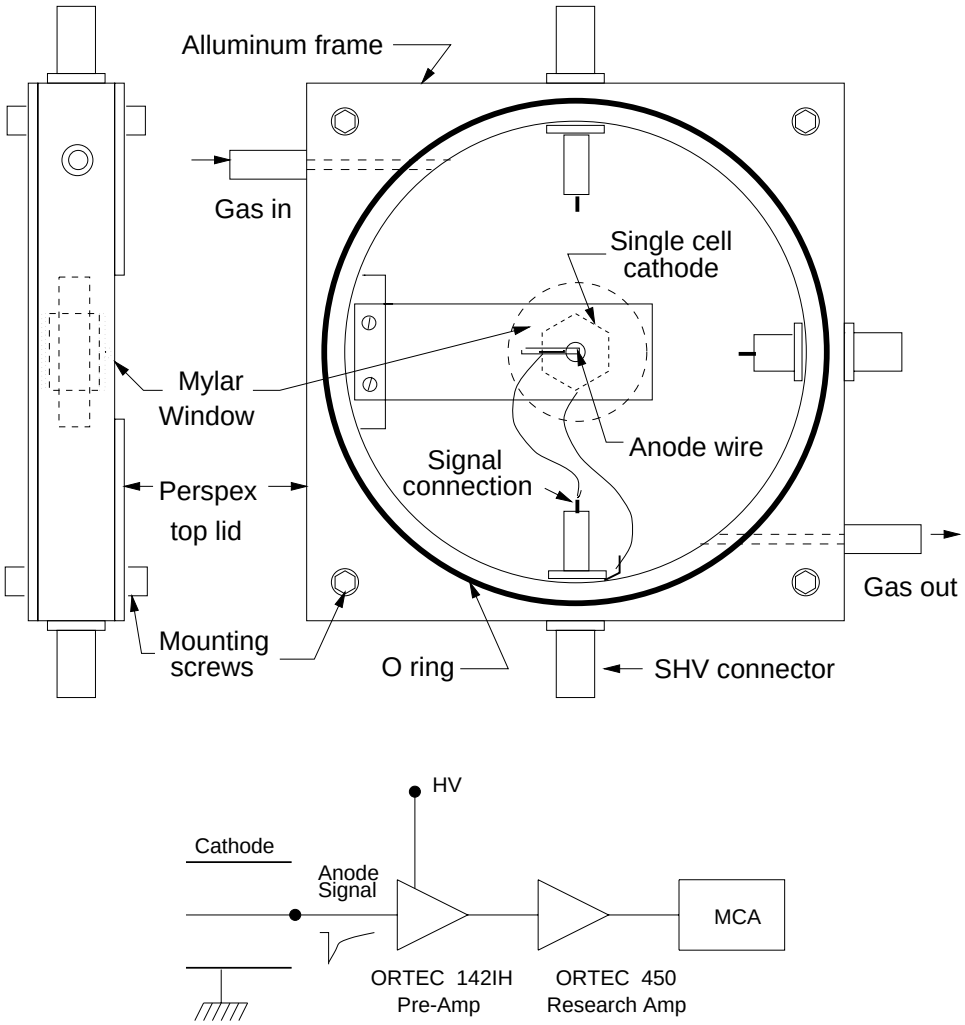

Figure 2.6: Schematic diagram of one cell with open geometry used in laboratory tests and the test set-up electronics. The enclosure volume was 100 mm $\times$ 100 mm $\times$ 12 mm.

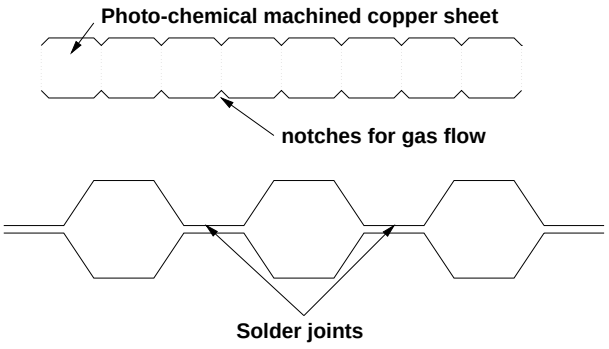

Figure 2.7: Sketch showing a half-row formed from metal pieces

The layout of a prototype chamber is schematically shown in Fig. 2.8. A G10 frame was machined to house the honeycomb. The thickness of the frame was 0.5 mm larger than that of the honeycomb to allow for tolerances. Gas flow nozzles were fitted on the sides of the frame.

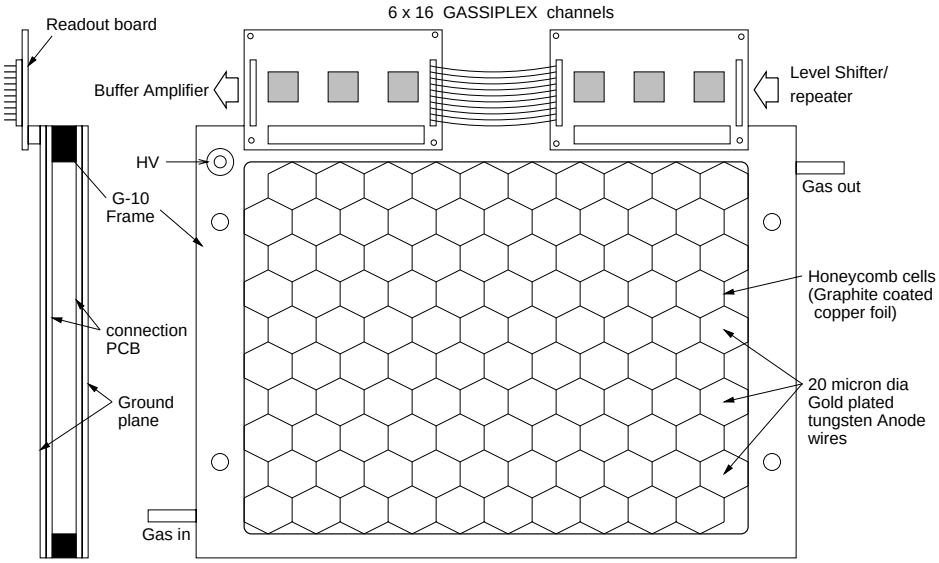

Figure 2.8: Layout of the hexagonal cells in the prototype chamber. The section on the left shows the G10 frame for the chamber. The size of the prototype was 180 mm $\times$ 165 mm.

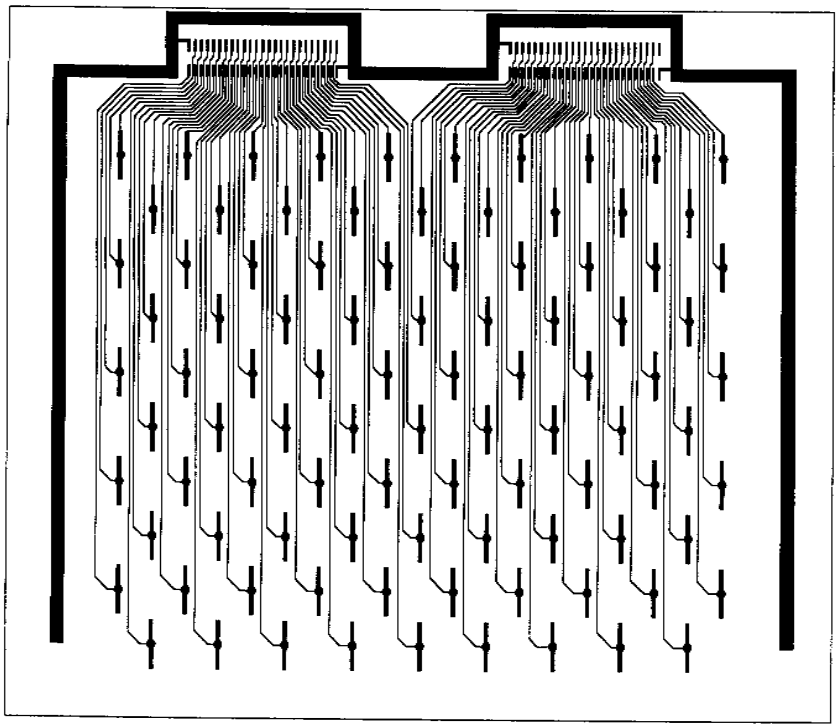

Figure 2.9: PCB layout for the open geometry prototype chamber.

2.2.2.2 Assembly of the chamber

Two printed circuit boards (PCBs) of thickness 1.5 mm each were fabricated. These had solder islands (1 mm $\times$ 4 mm) at the centre of each cell and thin (0.25 mm) tracks leading to 50 pin ERNI connectors, as shown in Fig. 2.9. One board contained the full wiring layout of the tracks, the other only solder islands to anchor the anode wires. One PCB was first bonded with epoxy to the G10 frame. Then the honeycomb was tack-glued to it (edges only) after checking the alignment. The second PCB was then

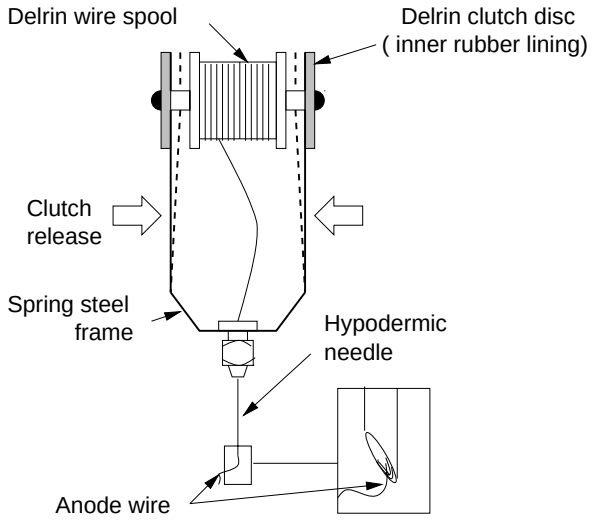

Figure 2.10: Jig for wire insertion during assembly of the prototype chamber.

bonded to the other side of the frame, taking care of the hole alignment, after bringing out the cathode (honeycomb) connection to the SHV connector.

The factory-supplied gold-plated tungsten wire (20 μm dia.) was wound on a separate spool of smaller dimensions. This spool was designed to fit into the wire insertion jig, which is shown in Fig. 2.10. During winding, the wire was first cleaned by pressing it against alcohol-dipped lint-free tissue. The wire was inserted through the holes of the PCB using the wire insertion jig. The jig consists of a small plastic wire spool on an aluminium frame with a hypodermic syringe needle fitted to the frame. The wire is drawn through the capillary of the needle and inserted through the PCB holes together with the needle. The needle was withdrawn after tack-soldering the wire onto the rear PCB. The wire was stretched to a tension of 25 g (equivalent to 30% of the elastic limit) using a spring-loaded slider on the spool, before being soldered onto the front PCB. Care was taken whilst soldering to prevent flux creepage into the cell. The holes were then closed by a high viscosity fast-setting (5 min) epoxy. The two copper-clad printed boards were again bonded on the soldered surface of the above-mentioned PCBs, with copper on the outer surface to make a proper shielding for the entire readout connections.

A thin Teflon-coated wire was soldered at one end of the structure, through which a negative voltage was applied to the cathode. This wire was brought out through a small hole (sealed later) to an SHV connector outside. Negative high voltage was applied to the honeycomb cathode through a high value (2.2 MΩ) non-inductive resistor with a HV decoupling capacitor. The readout board containing three GASSIPLEX chips [12] was connected at the edges.

2.2.3 Prototype-98

The first prototype was tested at the PS in 1998. The cells were made using 0.1 mm thick copper strips. The design of the cells in this case was based on the open geometry model. The radius of the hexagon was 7 mm corresponding to a cross-sectional area of 130 mm^2. This area was selected in order to be able to use the same chamber in the STAR experiment [13] as well. The depth of the chamber was kept to 12 mm. This chamber will be referred to as Prototype-98.

The layout of the chamber is shown in Fig. 2.8. The connectors and electronics boards were located at the edge of the chamber.

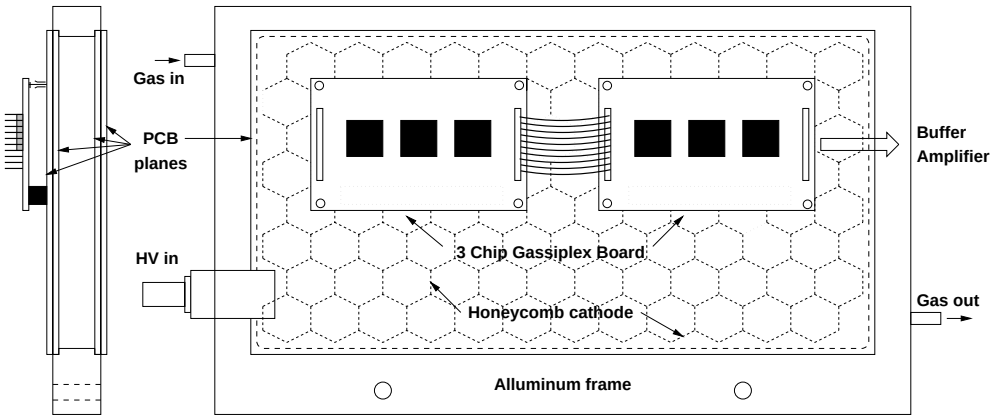

Figure 2.11: Schematic diagram of the prototype of the extended cathode chamber used in the May–June 1999 tests at the PS. The size of the prototype was 200 mm $\times$ 135 mm.

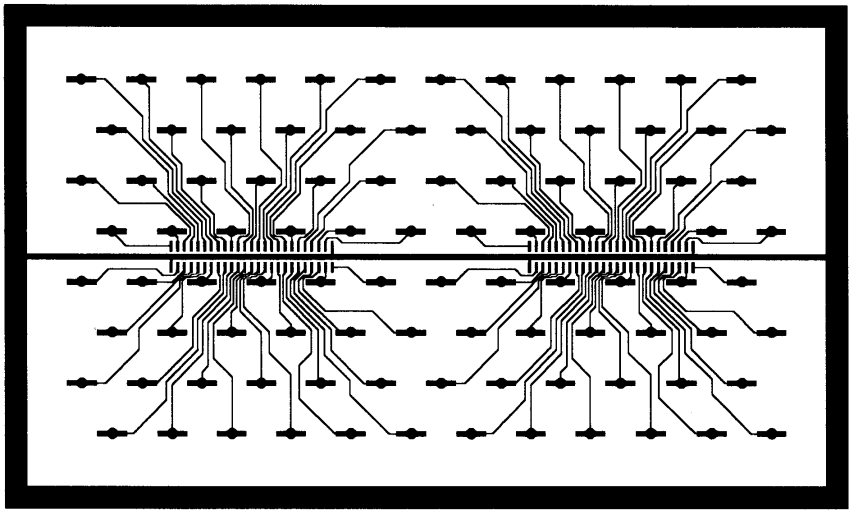

Figure 2.12: PCB layout for the extended cathode chamber used in the June 1999 tests at the PS.

2.2.4 Prototype-99

The results of the tests of open geometry models and simulations using GARFIELD led to the design of future prototypes. The cells in these prototypes were designed with an extended cathode structure. The honeycomb matrix was made using 0.2 mm thick copper strips. Two prototypes having 10 mm and 8 mm depths and a 1 cm^2 cross-sectional area each were fabricated and tested. These are referred to as Prototype-99-10 and Prototype-99-8, respectively.

In the extended cathode geometry the inner faces of the PCBs consist of a nickel-plated copper surface in contact with the cathode and extended towards the anode wire up to a radius of 2 mm. A cell with an extended cathode is shown schematically in Fig. 2.4.

The sketch of the 96-cell prototype with extended cathode geometry is shown in Fig. 2.11. This was designed with the aim of providing surface mounted connectors for the electronics at the back of the chamber, as will be used in the actual detector. The corresponding PCB layout is shown in Fig. 2.12. In this case also, we used 48-channel 3-chip GASSIPLEX boards as shown in the layout.

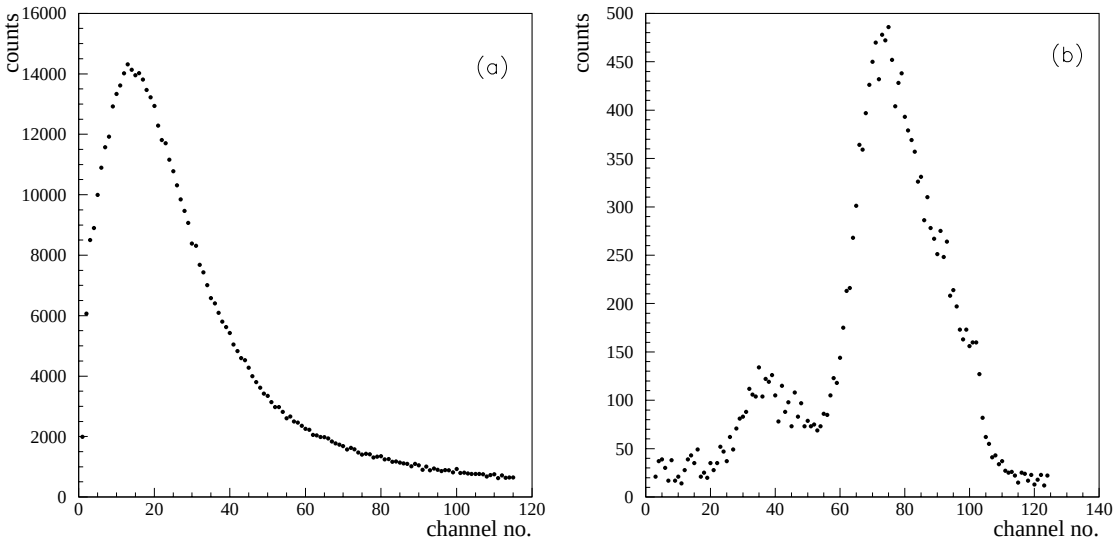

Figure 2.13: (a) β-ray spectrum from ^{106}Ru source, and (b) X-ray spectrum from ^{55}Fe source obtained with extended cathode single-cell operating at 1400 V. The gas mixture used was Ar (80%) + CO_2 (20%).

2.3 Test results

2.3.1 Laboratory tests

The first tests of the prototypes were performed using single-channel standard NIM electronics and radioactive sources. The cell housing was filled with Ar–CO_2 gas (pre-mixed in the ratio 80:20). A voltage scan was carried out to obtain a reasonable β-ray spectrum. The operating voltage for the open geometry model was in the range of 2000 V and that for the extended cathode type was in the range of 1400 V.

Typical spectra for the extended cathode prototype obtained with with a ^{106}Ru β-source and a ^{55}Fe X-ray source are shown in Fig. 2.13. The FWHM for the 5.89 keV X-ray line is about 15%.

In laboratory tests it was not possible to use cells with a completely closed geometry as the thickness of the PCB and other materials would not allow β-rays to pass through the gas all the way in order to have a trigger.

2.3.2 Test beam facilities and test layouts

Beam tests of the prototype chambers have been performed at the T10 and T11 beam lines of the PS and at the H6 beam line of the SPS. The response of the chamber to minimum ionizing particles (MIPs) were studied using pion beams at the PS and electron beams at the SPS without the converter. Preshower studies were carried out using electron beams and placing a converter in front of the chamber. The test set-ups are described below.

2.3.2.1 T11 beam line in 1998

The test set-up in the T11 beam line of the CERN PS is schematically shown in Fig. 2.14 for tests using a pion beam of 3.5 GeV energy to study the response of the chamber to minimum ionizing particles. It consisted of two sets of microstrip silicon detectors (MSD) for position information on the beam profile. Each set had three $x-y$ planes covering an area of 1 cm $\times$ 1 cm, each plane having 192 strips of 50 μm

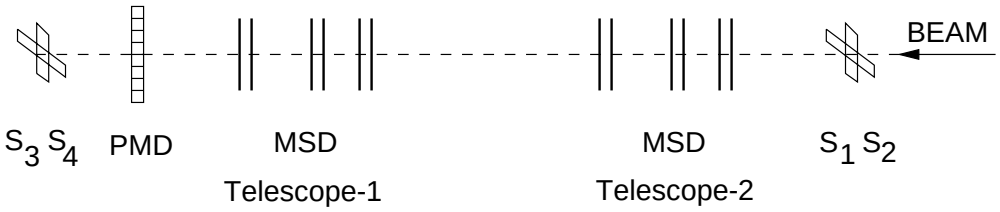

Figure 2.14: Test set-up at the T11 beam line of the PS in August 1998.

pitch. The MSDs were used to track particles through the prototype chamber so that smaller regions within a cell could be studied.

Two pairs of scintillators covering an area of 1 cm $\times$ 1 cm were used for generating triggers, one pair of scintillators being kept behind the prototype chamber. The beam trigger was defined by a four-fold coincidence of the scintillators. The pair of scintillators were aligned in the beam line by maximizing the individual and coincidence counts. The trigger rate for the pion beam varied between 20 and 100 per spill.

2.3.2.2 T10 beam line in 1999

During May–June 1999 a set of prototypes was tested in the T10 beam line using both pion and electron beams at various energies. The test set-up, shown in Fig. 2.15, consisted of three planes of cathode strip chambers (CSC) for tracking during runs with 7 GeV pion beams. Each CSC had strips at a pitch of 4 mm. The prototype chamber was kept in between the last two CSCs. The CSCs were used to track particles through the prototype chamber. Two pairs of crossed scintillators in a 4-fold coincidence provided the hadron trigger.

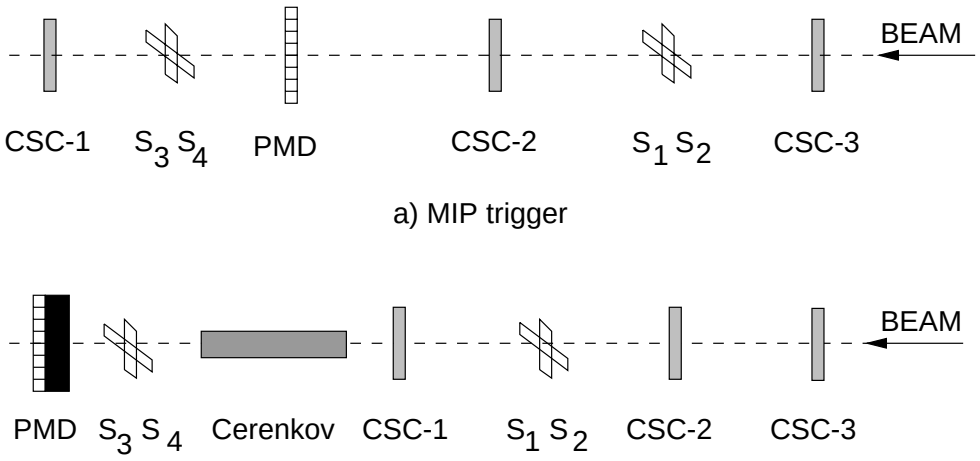

Figure 2.15: Test set-up at the T10 line during May–June 1999 (a) for pion runs and (b) for electron runs. A lead plate was placed in front of the chamber for preshower studies.

2.3.2.3 H6 beam line in 1999

The test set-up used for the SPS H6 beam line is shown in Fig. 2.16. As the main aim during this test was to study preshower behaviour using higher energy electrons, no tracking devices were used. The beam

passed through two pairs of crossed scintillators before falling on the chamber. The 4-fold coincidence of the scintillators provided the trigger. The response to MIPs was also studied using 30 GeV electrons incident on the bare chamber without the lead converter.

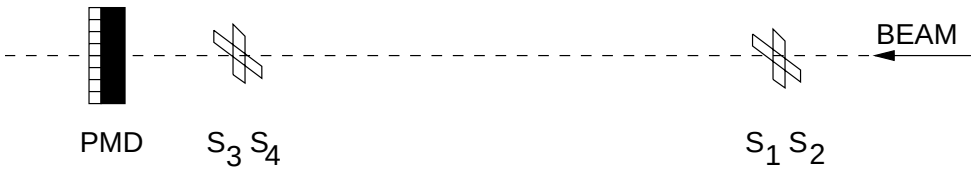

Figure 2.16: Test set-up at the SPS H6 line for preshower studies using electron beams in July 1999.

2.3.2.4 Electron trigger

For tests using electron beams to study the preshower characteristics, a lead plate was placed in front of the chamber. The thickness of the plate was 2 X_0 and 3 X_0. In this case the trigger scintillators behind the chamber would not register the beam particles. Hence these were brought in front of the prototype chamber and placed close to it.

A gas Cherenkov detector was used in the T10 beam line to tag the electrons. This was located further downstream of the cathode strip chambers. The prototype chamber was located 1 m behind the Cherenkov detector, and one pair of trigger scintillators was kept just in front of the prototype chamber.

At the H6 line of the SPS, electrons were produced using a lead target and used without discrimination, as the probability of pions being produced in such a case is small.

2.3.2.5 Electronics and data acquisition

The readout of the prototype chambers for the PS tests was carried out using old GASSIPLEX electronics [12] (1.5 μm version) and C-RAMS-based data acquisition [14]. The chips were obtained from CERN in the form of boards with three chips (48 channels) for the initial tests at the T11 line. For the 1999 tests the chips procured from CERN were assembled in India using indigenous passive components and assembly techniques. The MSDs and the CSCs used for hadron tracking were also read out using the same electronics and data acquisition system.

The honeycomb chamber with wire readout generates negative pulses. The dynamic range of GASSIPLEX for negative signals is rather low, being only 75 fC compared to 150 fC for positive pulses, and the output pulse is limited to –1 V. With the C-RAMS ADC having a range of 1K channels for 1.5 V pulses, we expected a saturation around 700 ADC channels. For the present tests, however, this is not a serious limitation.

For the preshower studies with higher energy electrons at the SPS, we used the new GASSIPLEX [15] (0.7 μm version) chip which has $\sim$ 4 times larger dynamic range. However, the output is still a 1 V pulse. With the 10-bit digitizer of the C-RAMS-based data acquisition, each ADC channel represents more input charge. Thus saturation is expected in this case also around 700 ADC channels.

The GASSIPLEX amplifier can be operated in silicon mode by removing the filter stage, in which case its dynamic range is larger [15]. However, the baseline recovery may not be efficient because of long tails of signals from gaseous detectors. This may affect its performance at rates exceeding several kHz. Data were also taken in silicon mode to study the dynamic range and saturation effects.

During T11 tests, the pedestals of the GASSIPLEX chips on board the prototype chamber were adjusted to around 60 ADC channels. The r.m.s. deviation of the pedestals was around unity and quite steady throughout the run. During the 1999 tests, the pedestals were around 160 channels with an r.m.s. deviation of $\sim$ 1.5 units. Since only one adjustment of threshold is possible for pedestals in one chain of GASSIPLEX chips and all the channels must remain positive, the pedestal is dictated by the channel having the highest negative offset. Thus it was not possible to reduce the pedestals further.

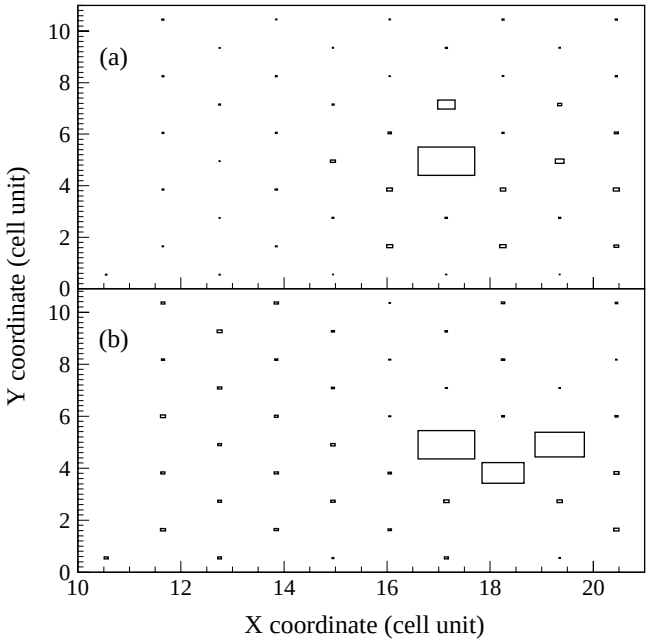

Figure 2.17: Two-dimensional plot of the cells affected: (a) chamber positioned to allow only one cell to intercept the beam, (b) chamber positioned such that beam hits at the boundary of cells.

2.3.2.6 Detector positioning

The prototype chamber was mounted on a stand having independent *x*- and *y*- movements, reproducible to within a millimetre. For most of the studies related to the detector's response to MIPs, the chamber was positioned in such a way that the beam profile was confined to almost one cell. This is shown in the 2-D plot of Fig. 2.17(a). The plot is a linearized version of the honeycomb array obtained by assigning *x* and *y* coordinates suitably. As the pair of scintillators had an overlap area of 1 cm^2 and the hexagonal cells also had a comparable area, in most cases the chamber could be positioned so that more than 90% of the beam entered the central cell. In some cases the chamber was moved to allow the beam to fall near the boundaries of two cells in order to study the effect of field distributions at the edges. The position of the affected cells in such a case is shown in Fig. 2.17(b).

2.3.3 Data analysis

2.3.3.1 Clustering of hits

Particles entering the chamber are expected to affect more than one cell in general. To analyse the data, the cell hits were first clustered using a simple nearest neighbour clustering algorithm. Two levels of nearest neighbours comprising 19 cells in two concentric rings around the hit cell were scanned for contiguous cells which might have been affected. The ADC channel contents in all the cells falling within the cluster were added together to represent the pulse height corresponding to the total energy deposited by the incident particle.

2.3.3.2 Tracking

The tracking system (MSDs and CSCs) provided the external reference for the impact point of the particle on the prototype chamber. In all cases only single-hit tracks having good reconstruction in all detector planes were used. Taking the last plane as the reference, projections were made on the prototype chamber. The projected coordinates were then used for further subdivision of the cell to study the variation in efficiency within the cell.

2.3.3.3 Terminology for the presentation of the data

For the discussions of the test results in the subsequent sections, the following terminology has been used:

ADC: represents the pulse height (in ADC channel units) for the cluster, both for hadrons (MIPs) and electron preshowers.

Cell ADC: represents the energy deposition in an individual cell.

MIP unit: Mean pulse height (ADC) due to MIPs (hadrons).

EDEP: energy deposition in keV units obtained from single particle GEANT simulations.

2.3.4 Results for Prototype-98

The results of prototype tests carried out in 1998 are described in detail in Refs. [16] and [3]. Some salient results are presented here.

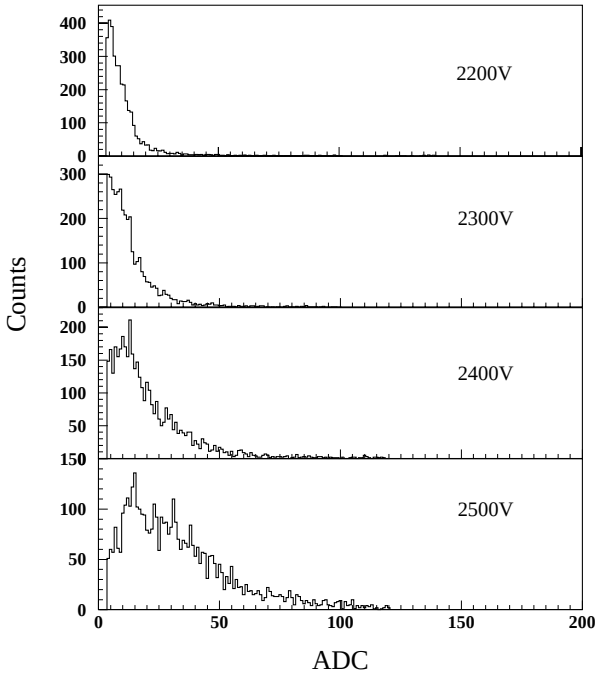

Figure 2.18: Pulse height spectra of 3.5 GeV pions at different voltages for the 12 mm deep open geometry chamber.

2.3.4.1 Characteristics for MIP detection

The pulse height spectra of 3.5 GeV pions at different voltages are shown in Fig. 2.18. Each ADC channel represents approximately 0.1 fC. The spectra move to higher channels as the voltage is increased.

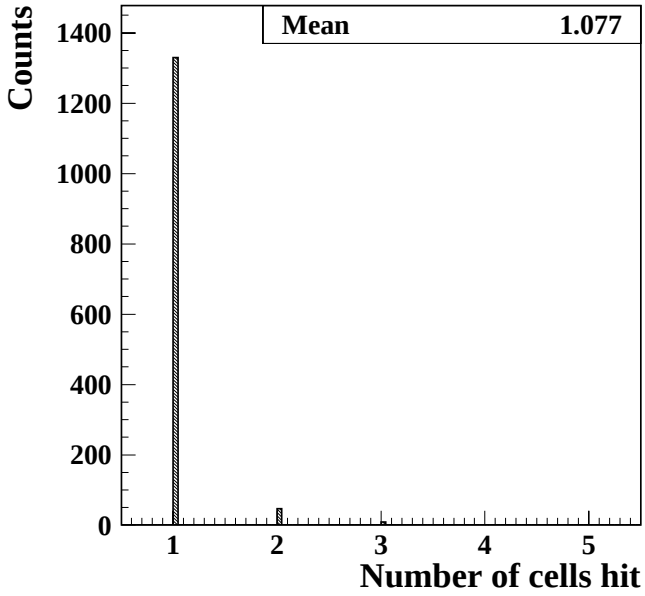

Figure 2.19: Number of cells affected by 3.5 GeV pions in prototype-98 at operating voltage of 2450 V.

A further increase in operating voltage was not considered necessary as the aim of the present prototype was to have good efficiency for detecting minimum ionizing particles at the lowest possible operating voltage so that a large dynamic range can be obtained for the preshower mode of operation.

Figure 2.19 shows the number of cells affected by MIPs. It can be seen that most of the MIPs are confined to within one cell, and only about 8% of the MIPs affect more than one cell.

This result is very significant, suggesting that the cellular design with wire readout is able to confine the charged particle signal, and that the crosstalk with neighbouring channels is negligible. Considering the fact that the average number of pads affected in the WA98 PMD for the MIP case was three, the present design represents a marked improvement and should allow us to handle the large particle multiplicity at the LHC.

2.3.4.2 Efficiency for charged-particle detection

The average efficiency as a function of applied voltage is plotted in Fig. 2.20(a). It was found that for the Ar + CO_2 gas mixture in the ratio 70:30, the efficiency is more than 90% and nearly independent of the applied voltage in the range studied. The optimum values of the gas mixture and the high voltage to be applied to the chamber were selected to be Ar(70%):CO_2(30%) and 2450 V.

The chamber was moved to various positions to study the efficiency within the cell and in particular at the boundaries using the beam profile, as registered in the six planes of the MSDs.

Figure 2.20(b) shows the variation of efficiency as a function of position in the *x*-direction at 1 mm intervals covering a full cell and parts of two cells on the sides. It was found that whilst the central part of the cell has a uniform efficiency of around 95%, the efficiency is reduced to about 70% at the extreme edge. A small part of this reduction in efficiency can be attributed to the dead area imposed by the cell wall, but the major reason remains the non-uniformity of field distribution within the cell as described in Section 2.1.3.

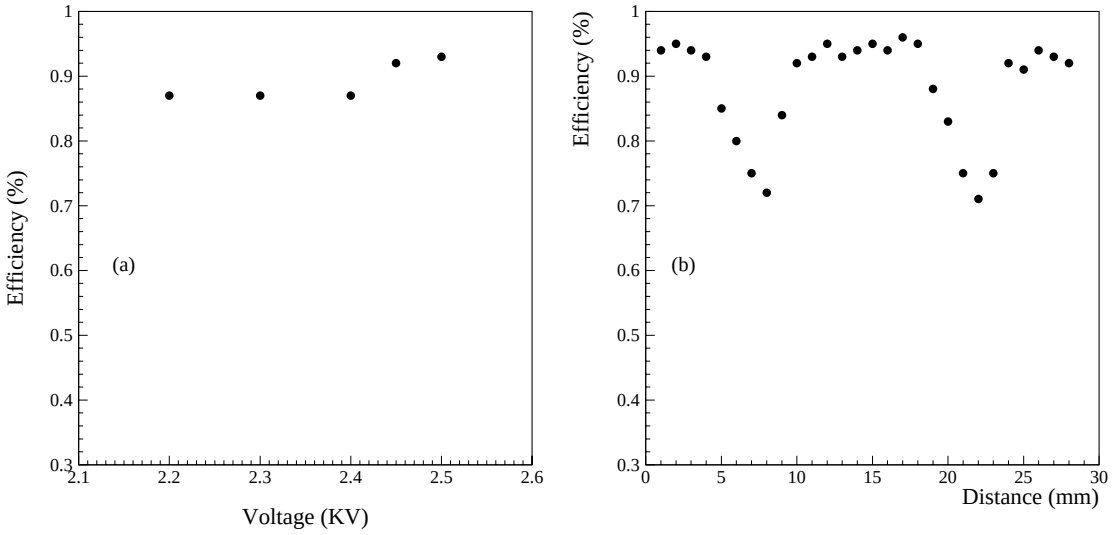

Figure 2.20: (a) Variation of the charged-particle detection efficiency with applied voltage for Prototype-98, and (b) Variation of efficiency as a function of distance from the anode wire within a cell for an operating voltage of 2450 V. One cell extends to 14 mm.

2.3.5 Results for Prototype-99

Two prototypes having 96 cells each, with a cell cross sectional area of 1 cm^2 and gas depths of 8 mm and 10 mm (referred to as Prototype-99-8 and Prototype-99-10, respectively) were used for the tests. The results are described below.

2.3.5.1 Characteristics of MIP detection

Typical pulse height spectra for 7 GeV pions incident on the prototype chambers are shown in Fig. 2.21(a,b) along with fits using a Landau distribution. The mean value of the fitted distribution is taken as a measure of the average energy deposition by a MIP. Taking into account the sensitivity of GASSIPLEX-1.5, the range setting of the C-RAMS ADC and the average pulse height for MIPs, we estimate the gas gain to be $\sim 10^3$.

The distribution of the number of cells hit is shown in Fig. 2.21(c). The average is close to unity, suggesting that MIPs are essentially confined to one cell. Even when the chamber was positioned such that the beam profile was at the boundary of two cells, the average number of cells affected by a MIP was found to change only marginally. This satisfies one of the basic requirements of our design.

A further investigation was carried out for clusters having more than one cell. It was observed that the probability of firing the second cell around the central cell is almost uniform. For these cases the pulse heights are quite high, suggesting contributions from many particles. Such high pulse height values can be attributed to a possible small admixture of electrons in the trigger and also to secondary interactions taking place in upstream materials.

2.3.5.2 Optimization of operating conditions

The operating conditions (e.g. the gas mixture and the operating voltage) were optimized after a detailed study of the variation of the MIP detection efficiency and the proportionality region. Figure 2.22(a) shows the variation of efficiency for various gas mixtures for both the 10 mm and 8 mm prototypes. It was found that for 90:10 and 80:20 proportions of Ar and CO_2, efficiency values of $\sim$ 99% are easily

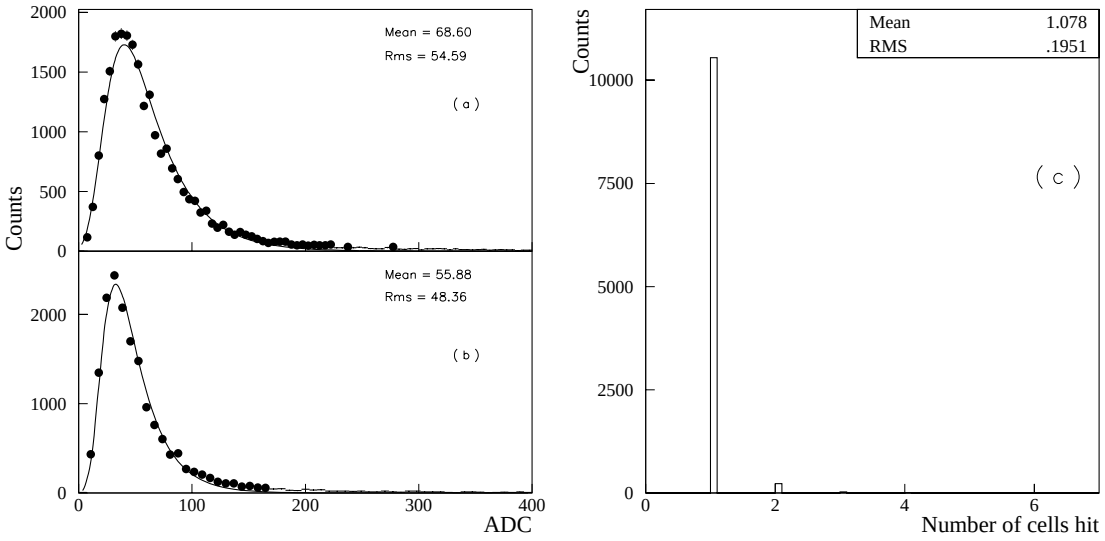

Figure 2.21: Results on the response of the extended cathode prototype to a 7 GeV pion beam: (a) pulse height spectrum for the 8 mm deep chamber at 1520 V, (b) pulse height spectrum for 10 mm deep chamber at 1450 V. Fits using the Landau distribution are shown by solid lines. (c) Number of cells affected in the 8 mm deep chamber at 1520 V.

obtained. For the 70:30 case, the efficiency attained was 96%. For the same applied voltage the silicon mode of operation of GASSIPLEX results in reduced efficiency, primarily due to problems with baseline recovery. The charge collected within the peaking time of GASSIPLEX is reduced and the resulting efficiency is low.

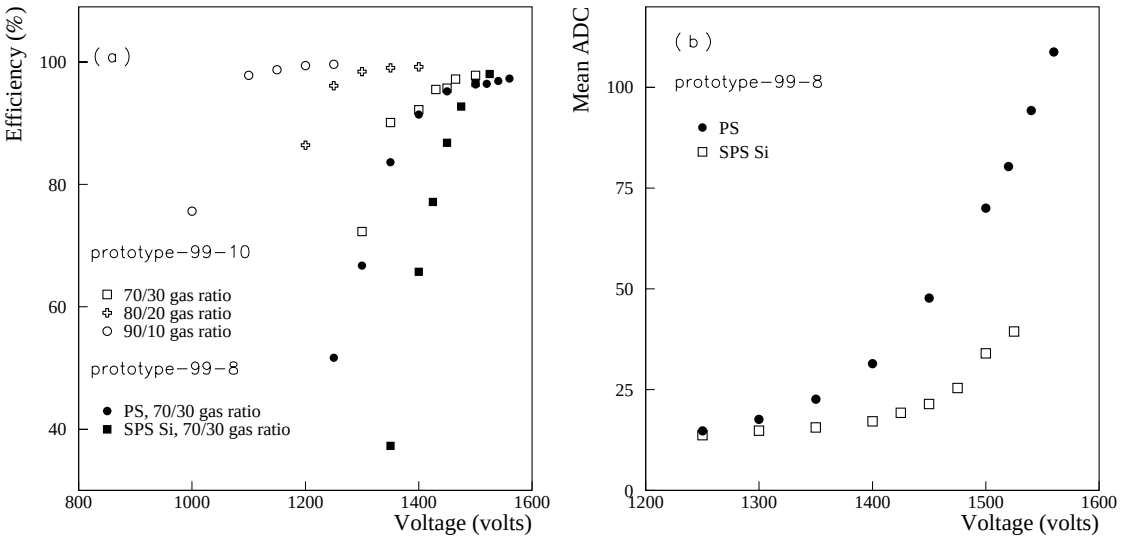

Figure 2.22: (a) Variation of charged particle detection efficiency with applied voltage for various gas mixtures and operating modes of GASSIPLEX chips. SPS-Si denotes the data taken at the SPS using GASSIPLEX in the silicon mode); (b) Variation of mean pulse height (ADC) as a function of applied voltage for Prototype-99-8 in the gas mode of operation (PS data) and in silicon mode of operation (SPS data) of the readout chip.

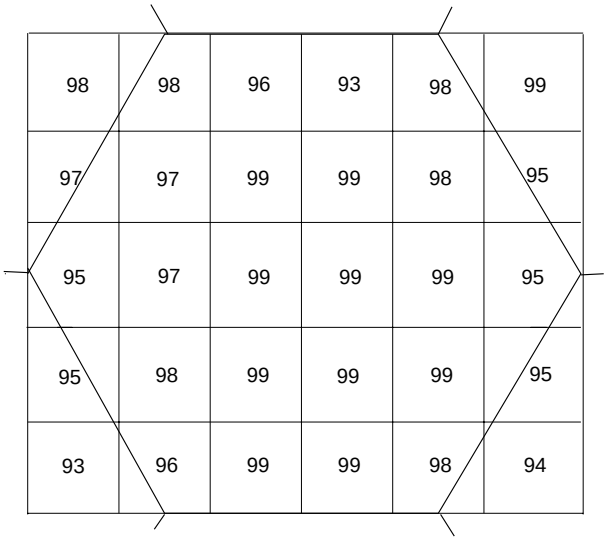

Figure 2.23: Variation of efficiency within a cell in a 2 mm x 2 mm grid.

Figure 2.22(b) shows the evolution of pulse height as a function of voltage due to increased electron multiplication in the gas. In the region of near constant efficiency, the mean ADC values increase approximately linearly with voltage, indicating the onset of the proportional region.

Although with a higher percentage of Ar in the gas mixture the efficiency of detection of charged particles is higher, the long tails in the signal are removed faster if the percentage of CO_2 is higher. This is important for handling a higher rate of particle fluxes. As a compromise, we have chosen the operating gas to be a mixture of Ar and CO_2 in the ratio 70:30. The operating voltages selected for Prototype-99-10 and Prototype-99-8 were 1450 V and 1520 V, respectively.

2.3.5.3 Variation of efficiency within a cell

A high statistics scan of the chamber was taken around selected cells to study the variation of efficiency within the cell in smaller *x*- and *y*-bins. For this scan the chamber position was shifted by a few millimetres in both the horizontal and vertical directions around the incident beam. The data were analysed to estimate the efficiency within the cell with the help of tracking coordinates provided by the CSCs.

The detector was divided into 2 mm wide bins in the *x*- and *y*- directions. Figure 2.23 shows the variation of efficiency in 2 mm $\times$ 2 mm regions throughout the cross section of the cell. The efficiency was found to be (96 ± 3)% throughout the cell. The efficiency values obtained at the junction of two cells correspond to the contribution from both the cells. The slight decrease at the boundaries may be attributed to the dead area of the cell wall as well as to the cell-to-cell fluctuation in efficiency. The present design with the extended cathode is thus able to provide uniform efficiency throughout the cell volume. This should be compared with the results with the open geometry model, as discussed in section 2.3.4.2.

Figure 2.24 shows typical pulse height spectra for MIPs when the beam was positioned at the centre of a cell, and 5 mm away from the centre towards the left and right. They are identical, the mean ADC being within statistical errors. This demonstrates that the behaviour of the honeycomb chamber is uniform throughout its volume.

2.3.5.4 Cell-to-cell variation of efficiency

About 40 cells, randomly selected over the area of the prototype, were scanned by positioning them into the beam to study the detection efficiency and average pulse height for MIPs. The relative gains of the cells, defined by the ratio of the mean pulse height in a cell to the average value of the mean pulse heights

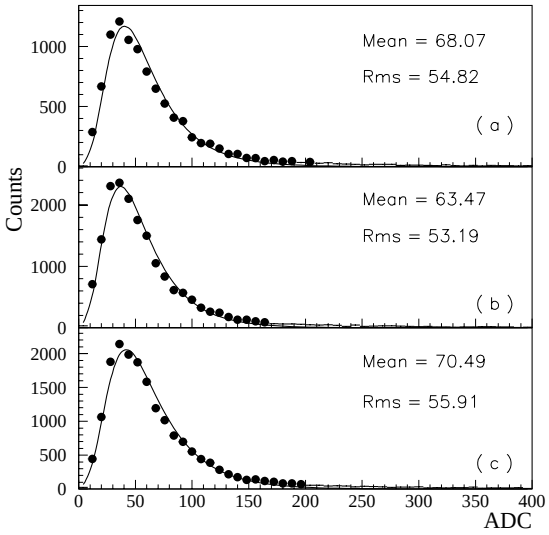

Figure 2.24: MIP spectra in an 8 mm chamber at three different positions : (a) when the beam is positioned in the centre of the cell, (b) 5 mm towards the left of centre, (c) 5 mm towards the right of centre.

in all the cells taken together, is shown in Fig. 2.25. The overall gain of the prototype chamber was found to be quite uniform, the distribution having a width (σ) of only 6%. The efficiencies of the cells scanned are also shown in the figure. All the cells have efficiency in excess of 96%.

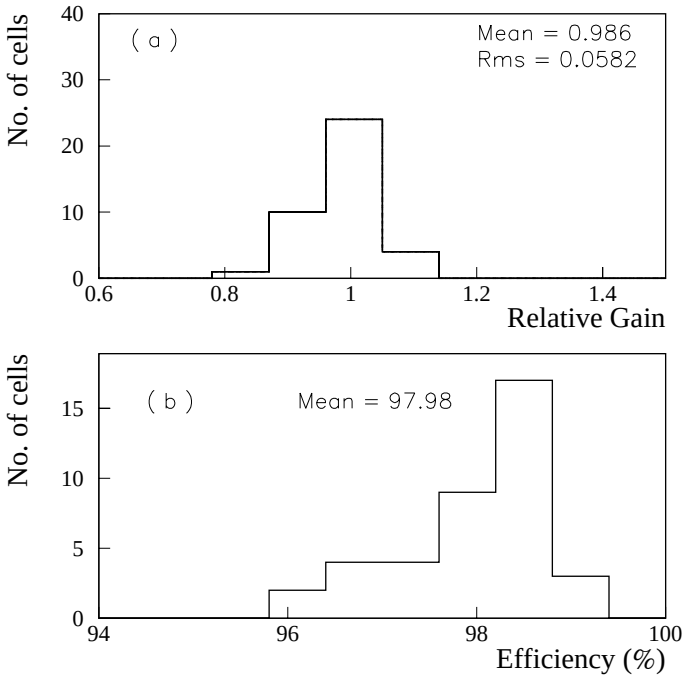

Figure 2.25: (a) Relative gains of various cells in an 8 mm extended cathode chamber, and (b) efficiencies of the cells.

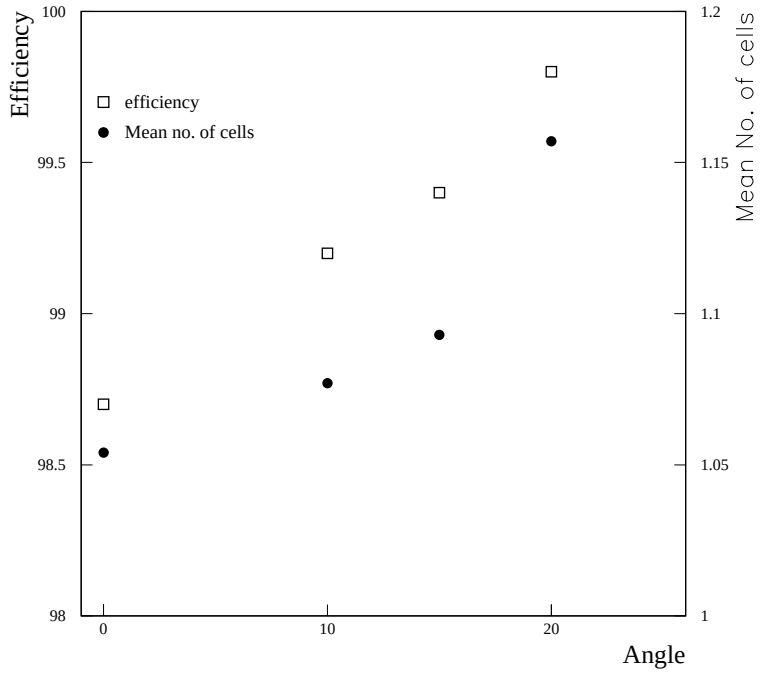

Figure 2.26: Detection efficiency (left y-axis) and mean number of cells (right y-axis) as a function of angle of incidence for 7 GeV pions.

2.3.5.5 Angular incidence

The PMD in the ALICE experiment will cover the angular range 8°–18°. We have therefore studied the number of cells affected by charged particles for non-normal incidences. For this purpose the chamber was rotated with respect to the beam direction to subtend approximate angles in the range of 10–20°. The results are shown in Fig. 2.26. The average number of cells affected by MIP increases only by a few per cent, and the efficiencies show a slight increase due to the increased path length of the particles passing the chamber.

The region of larger angular incidence in the actual detector also happens to be the region of relatively lower occupancy. Hence even when the average number of cells hit by charged particles becomes slightly larger than unity, it is not expected to create a significant overlap of photon and charged particle clusters.

2.3.5.6 Count rate capability

During the SPS test run in July 1999 the chamber was subjected to various particle fluxes to study the count rate capability. The GASSIPLEX chip was operated in gas mode. The collimators were opened successively to allow more beam into the chamber. The count rate was determined by the coincidence counts in the S3 $\times$ S4 pair which was close to the chamber (see Fig 2.16). The MIP spectra and efficiencies were studied as a function of rate ranging from $\sim$ 30 to $\sim$ 1000 particles/cm^2/sec. The results are shown in Fig. 2.27. The mean pulse height and the detection efficiency are found to be stable.

The flux of particles incident on the PMD chambers (including secondaries as described by GEANT simulation) will be $\sim 10^3$ particles/cm^2/sec in typical central Pb+Pb collisions. Thus the present tests suggest that the chamber can be successfully operated in the experiment. Further tests will be carried out with higher flux rates to understand the behaviour at even higher rates. This will enable us to determine the safety margin of operation.

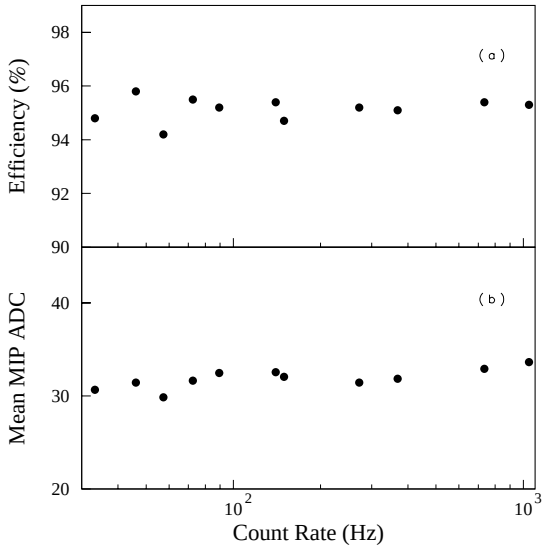

Figure 2.27: Effect of count rate on (a) detection efficiency and (b) mean pulse height (ADC) for MIPs.

2.3.6 Preshower characteristics

The preshower characteristics were extensively studied for Prototype-99-8 using electrons in the energy range of 1–6 GeV at the PS and in the range 7–30 GeV at the SPS. Both 2 X_0 and 3 X_0 thick lead converters were used. The results are described below.

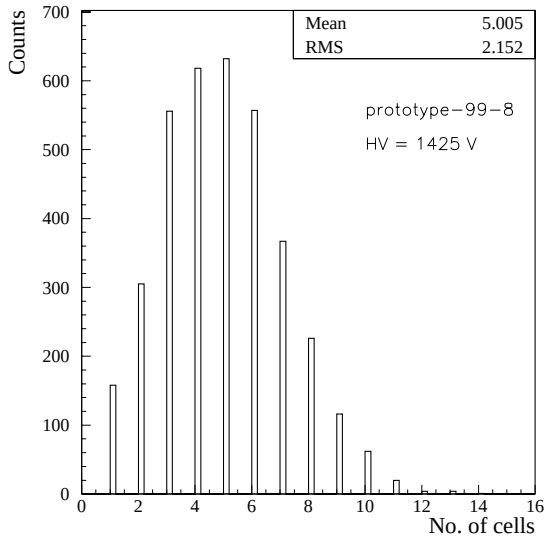

Figure 2.28: Distribution of hit cells for a typical preshower of 3 GeV electrons passing through a 3 X_0 thick lead converter.

2.3.6.1 Operating voltage

The old GASSIPLEX electronics has a small dynamic range of only 75 fC for negative input pulses. Considering the average number of shower particles produced by the highest energy electrons available

at the T10 beam line, the operating voltage was reduced to avoid large-scale saturation of the preshower signal. After a study of the efficiencies at intermediate voltages, we selected 1425 V as the operating voltage. However, data were also taken at 1465 V, to compare saturation effects and to understand better the linearity and dynamic range requirements of the readout electronics.

2.3.6.2 Transverse shower spread

A typical distribution of the number of cells affected in the preshower detector with a 3 X_0 thick converter for 3 GeV electrons is shown in Fig. 2.28.

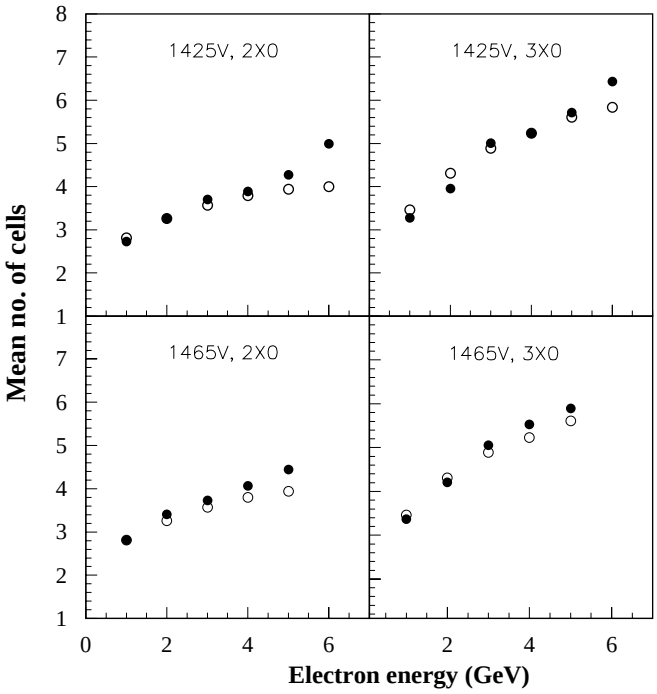

Figure 2.29: Number of cells affected by a preshower for different electron energies. The converter thicknesses used are shown in the figure. The filled circles denote test data and the open circles are simulation results.

The average number of cells affected by a preshower have been studied for several combinations of electron energies and converter thicknesses. The results are summarized in Fig. 2.29. Comparing the results with single particle GEANT simulation for electrons, it was found that the average preshower size is very close to that obtained in simulation. This is a very important result and represents a marked improvement over the WA98 PMD case where the preshower size in test data was about twice that obtained in simulation. The final occupancy in the actual experiment is expected to be well described by simulation results, enabling a reliable production of mock data for further analyses. These results also suggest that when the efficiency is high, further increase in the gain (voltage) has only a marginal effect on the transverse shower size.

2.3.6.3 Energy deposition

The preshower pulse height spectra, obtained by adding the ADC contents of all the cells in a preshower cluster, are shown in Fig. 2.30 along with the corresponding single particle simulation results. The two sets of spectra look similar in shape. The mean values of the two sets provide the calibration relation

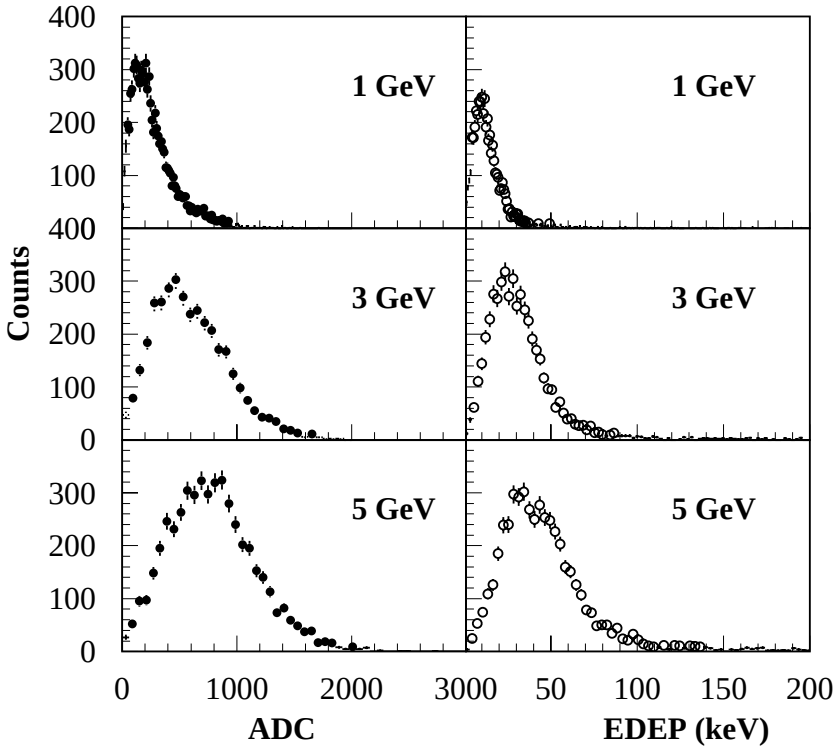

Figure 2.30: Preshower spectrum for different electron energies for a 3 X_0 thick converter. The left panels show the test data and the right panels show simulation results.

between the deposited energy (in keV) and the pulse height (in ADC) as described in the following section.

The preshower spectra at two different gains, differing by about 40%, are shown in Fig. 2.31 where the pulse height scale is normalized in MIP units. The spectra are similar in shape at the two gains, giving an almost identical mean value and width. This also shows that at both operating voltages the gains are adequate and that the mean ADC of a MIP is a good representation for normalizing the energy deposition.

2.4 Detector calibration

2.4.1 Introduction

A good knowledge of the detector response is required to produce simulated data in ADC units in which the effects of detector and readout electronics are properly folded in. These data should resemble the actual experimental data that will be used for developing the analysis tools and also for generating mock data before the start of the experiment. This information is obtained by a detailed comparison of the test beam data with single particle simulations. Such a procedure has already been employed for the WA98 PMD [17].

The calibration of the preshower PMD is performed using extensive test data at a number of energies using electron and pion beams using Prototype-99-8. A simulation framework was developed which describes the entire test data.

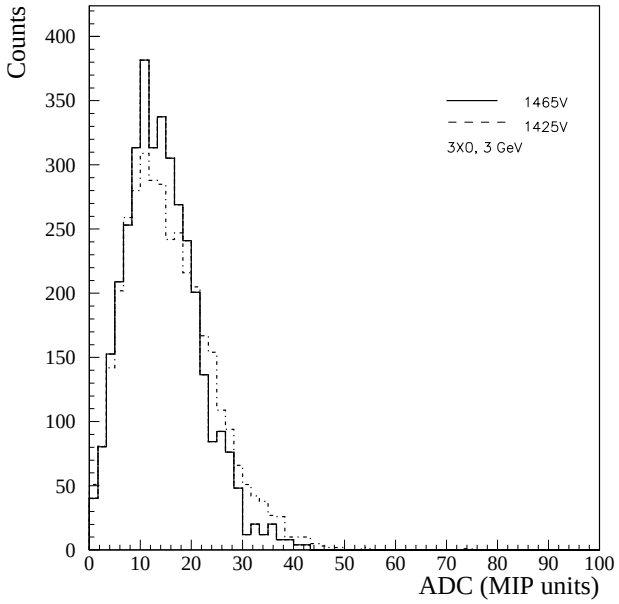

Figure 2.31: Preshower spectra for 3 GeV electrons with a 3 X_0 thick converter at two different voltages. The X-axis is expressed in MIP units.

2.4.2 Calibration relation

A relation between the deposited energy and mean pulse height can be obtained from the mean positions of spectra obtained in simulation and test beams. A comparison of test data and simulation also allows us to understand features specific to the readout system and crosstalk, if any, and to parametrize the effects.

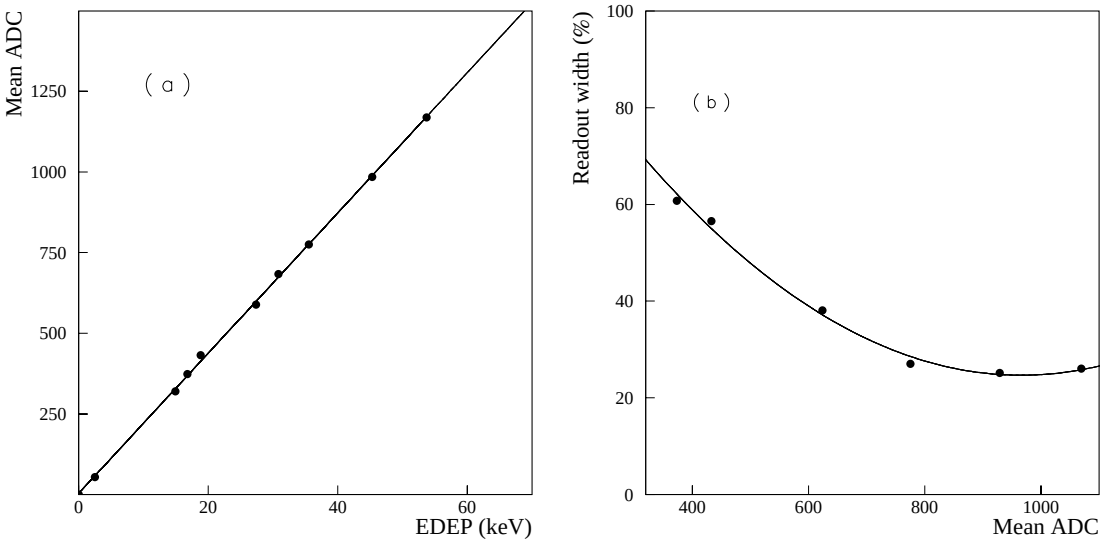

Figure 2.32: (a)Average ADC vs. energy deposition for various combinations of electron energy and converter thickness used in preshower studies at 1465 V. (b) Readout width in percentage as a function of energy deposition in ADC units derived from preshower spectra.

Figure 2.32(a) shows the calibration relation for an operating voltage of 1465 V using the PS data for old electronics. The response of the detector and readout is quite linear in the range of energy deposition studied.

2.4.3 Readout width

The GEANT simulated preshower spectra shown in Fig. 2.30 correspond only to the energy deposition in the sensitive medium, the detector effects being absent. Comparing these spectra with the test beam pulse height spectra it is observed that the widths of the distribution in the test beam data are larger than those of simulated distributions in all the cases. The increased width in the test beam data arises because of extra fluctuations in the gas ionization, signal generation, and transmission processes. The combined effect of these extra fluctuations is called *readout width* [17]. Assuming that various contributions to the fluctuations are uncorrelated, one can deduce that

$$\text{Readout width} = \sqrt{\left(\frac{\sigma_{\text{test}}}{\Delta E_{\text{test}}}\right)^2 - \left(\frac{\sigma_{\text{sim}}}{\Delta E_{\text{sim}}}\right)^2}$$

where ΔE_{test} and ΔE_{sim} are the mean energy deposition obtained from test results and simulation, respectively, and σ_{test} and σ_{sim} are the corresponding widths of the distributions in the two cases.

The readout width as a function of energy deposition, as represented by the total ADC of the cluster, is shown in Fig. 2.32(b) for the various cases of preshower studies. A polynomial fit is made to the above data for extrapolation to intermediate values of the preshower signal. The trend of values is similar to that observed earlier [17]. It is higher at lower energies because of larger fluctuations in the number of primary ionization electrons.

2.4.4 Study of dynamic range

The dynamic range of the readout electronics required for a preshower detector has to be very large. However, such an electronics in ASIC form is normally not available and would be very expensive to develop only for the present requirements of the PMD. We have studied the effect of the limited dynamic range offered by both the old (1.5 μm version) and the new (0.7 μm version) GASSIPLEX chips in preshower applications.

2.4.4.1 Level of saturation

A typical ADC spectrum of a cell for a preshower of 3 GeV electrons taken with the old chip is shown in Fig. 2.33(a). For comparison, the simulated spectrum of energy deposition in a cell is shown in Fig. 2.33(b). The experimental spectrum shows saturation around 700 ADC channels due to the limited dynamic range of the electronics.

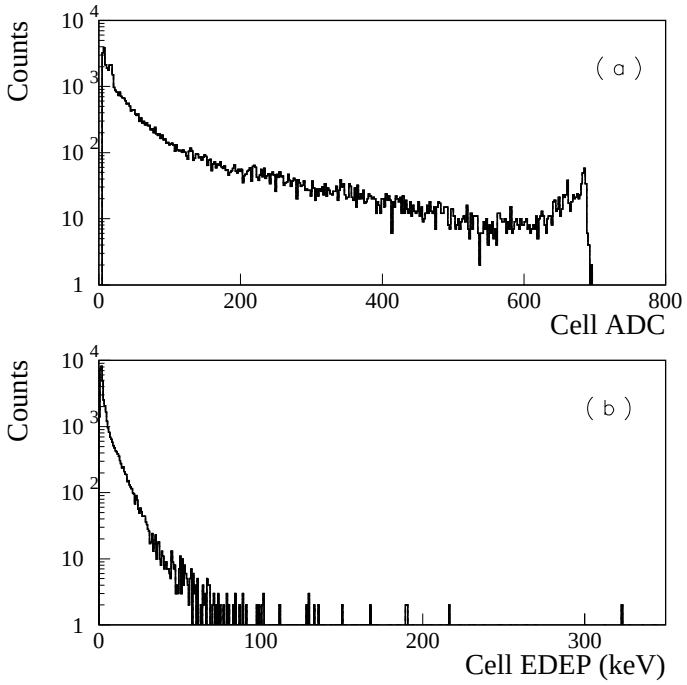

Figure 2.33: Test beam data and simulated spectra for 3 GeV electrons passing a 3 X_0 thick converter: (a) Typical cell ADC spectrum showing saturation around channel 700 at 1425 V (1 ADC channel $\approx$ 0.1 fC.); (b) energy deposition (EDEP) in a cell from GEANT simulation.

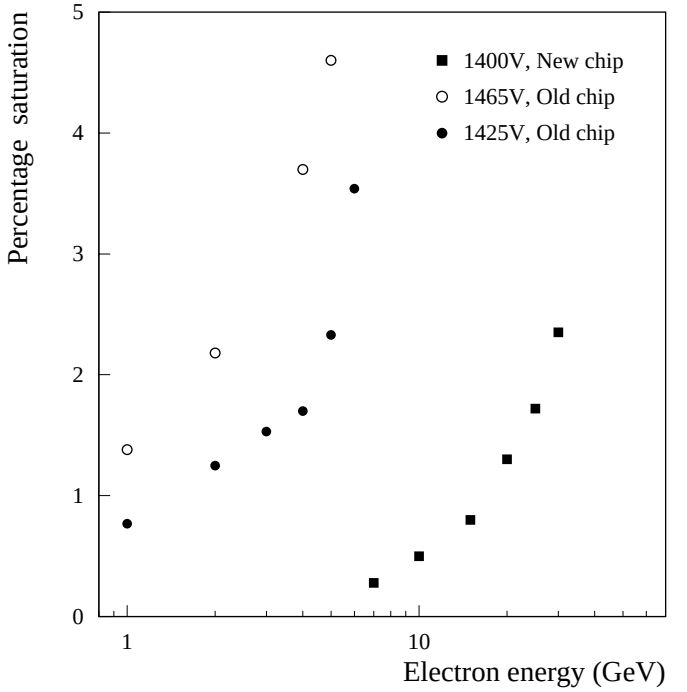

Figure 2.34: Percent saturation for preshower cell ADCs and 3 X_0 thick converter as a function of electron energy for different gains.

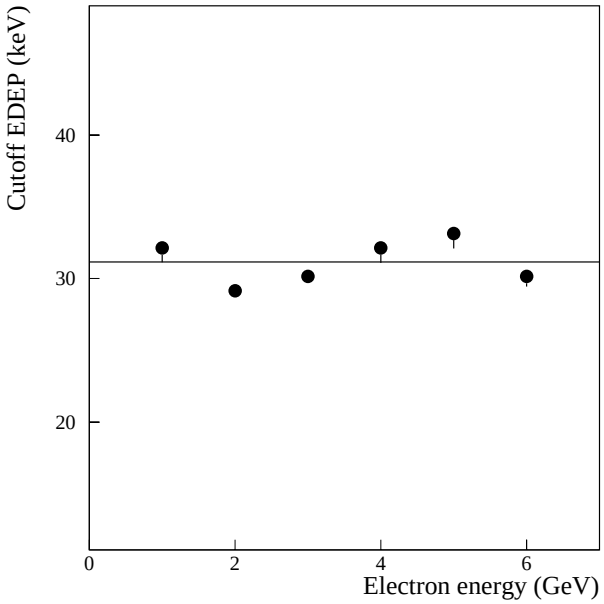

Figure 2.35: The cutoff value of energy deposition as a function of electron energy for PS data at 1425 V taken with old GASSIPLEX chip.

By parametrizing the distribution in Fig. 2.33(a) between 200 and 500 ADC channels and extrapolating to saturation region, we have estimated the percentage of cell hits going into saturation. This is taken as a measure of the level of saturation. The percentage of saturation was evaluated for all cases studied at the PS (with old chip) and at the SPS (with new chip). Figure 2.34 summarizes the results for the PS data of electrons taken at 1425 V and at 1465 V, and the SPS data taken at 1400 V. In these cases the level of saturation is below 5%.

2.4.4.2 Estimate of the cutoff energy deposition

The saturation in the cell ADC spectrum occurs when the energy deposition in a cell exceeds a certain limit and the charge collected is higher than what can be handled by the analog signal processing circuit. This value of energy deposition, referred to as the cutoff value, depends only on the gain (i.e. voltage applied) and not on the incident electron energy. The higher the gain of the detector, the lower the cutoff value of the energy deposition will be.

To estimate the cutoff value of the energy deposition, we compare the cell ADC and the EDEP spectra for various incident electron energies. The cell energy deposition value (in keV) beyond which the area under the tail part in simulated distribution equals the percentage saturation observed in test beam data is a measure of the cutoff value. The results for the old chip with the chamber operating at 1425 V are shown in Fig. 2.35. The cutoff values thus obtained are independent of the electron energy.

The average values of the cutoff energy deposition for various gains and GASSIPLEX versions obtained in the above way are presented in Table 2.2. This suggests that at present the dynamic range of the new GASSIPLEX chip is $\sim$ 75 keV (equivalent to 30 MIPs) at an operating voltage of 1425 V. The corresponding value at 1465 V is estimated to be 60 keV.

Table 2.2: Dynamic range of GASSIPLEX as deduced from test runs. The last entry shows the value for the silicon mode of operation of the new version of the GASSIPLEX chip.

Chip version	Voltage (V)	Dynamic range (keV)	Efficiency (%)
Old	1425	31	94
Old	1465	24	96
New	1400	88	86
New	1425	77	91
New (Si)	1475	120	93

2.4.4.3 Modelling the energy deposition

For the same thickness of the converter, the average energy deposited by a photon of given energy is considerably less than that by an electron of the same energy. The spectrum of the energy deposition in about 0.3 million cells, taken from VENUS + GEANT simulation of a large number of events, is shown in Fig. 2.36(a). The percentage of cells going into saturation due to the limited dynamic range is presented in Table 2.3. This suggests that in the actual experiment the present dynamic range of 30 MIPs will result in only 0.4% of cells being in saturation. For clustering of hits this is a small effect. This will not affect the performance of the detector.

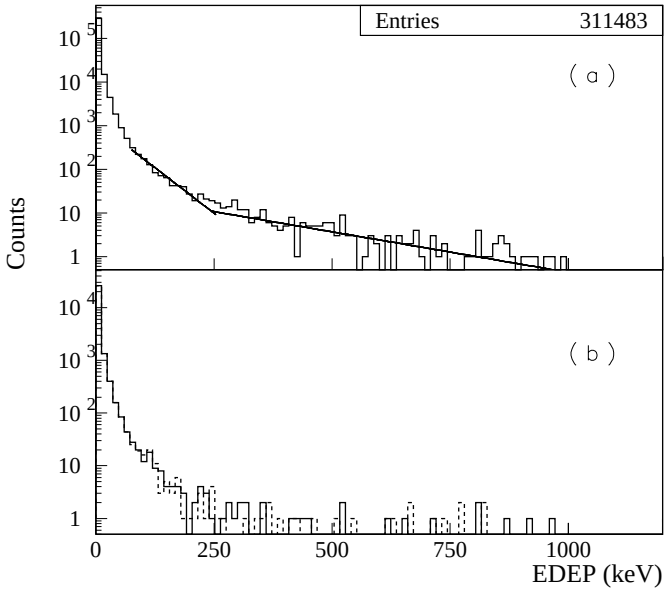

Figure 2.36: (a) The cell EDEP spectra from GEANT simulation in histogram form. The two-piece straight line represents a fit to the spectrum in the tail part beyond the cutoff EDEP. (b) Simulated cell EDEP spectrum for an event (solid histogram) and extrapolated EDEP spectrum (dashed histogram) after modelling the region above the cutoff energy deposition.

Table 2.3: Effect of different dynamic ranges on saturation (1 MIP unit = 2.5 keV).

Dynamic range (MIP units)	% of cells in saturation	% error on total energy before modelling	% error on total energy after modelling
25	0.56	9.5	1.5
30	0.42	8.9	1.6
40	0.28	7.1	1.4

However, the total energy in an event, which is required for estimating the transverse electromagnetic energy, will be underestimated. Column 3 of Table 2.3 shows the error introduced in the total energy due to saturation.

We have studied a simple modelling of the tail part of the cell energy deposition. The tail beyond the cutoff energy deposition dictated by dynamic range is fitted with a sum of two exponential functions. Random numbers are then generated following the fitted distribution to redistribute the saturated part into the tail. This is shown for a typical event in Fig. 2.36(b). The error introduced in total energy deposition in an event after modelling is considerably reduced and is found to be independent of the dynamic range, as shown in the last column of Table 2.3.

2.4.5 Production of mock data

The final stage for simulation will be the production of a data set identical in structure with the actual experimental data. This data, called ‘mock data’, allows a rigorous testing and tuning of all the analysis software prior to the start of the experiment. This data set will also be used for the training of the neural network algorithm and for estimating the photon counting efficiency. Such a scheme has already been employed for the WA98 PMD [17].

The scheme for generating mock data is presented in Fig. 2.37. Starting from the energy deposition values for each track, we generate zero-suppressed data, where the cell coordinates and the cell signal (ADC) are packed into one word. For each cell, another word containing the parameters of the incident track (e.g. energy, angles, particle type) will also be stored in digitized form with a flag. An important use of the mock data will be the study of various algorithms for data compression in order to reduce data volume.

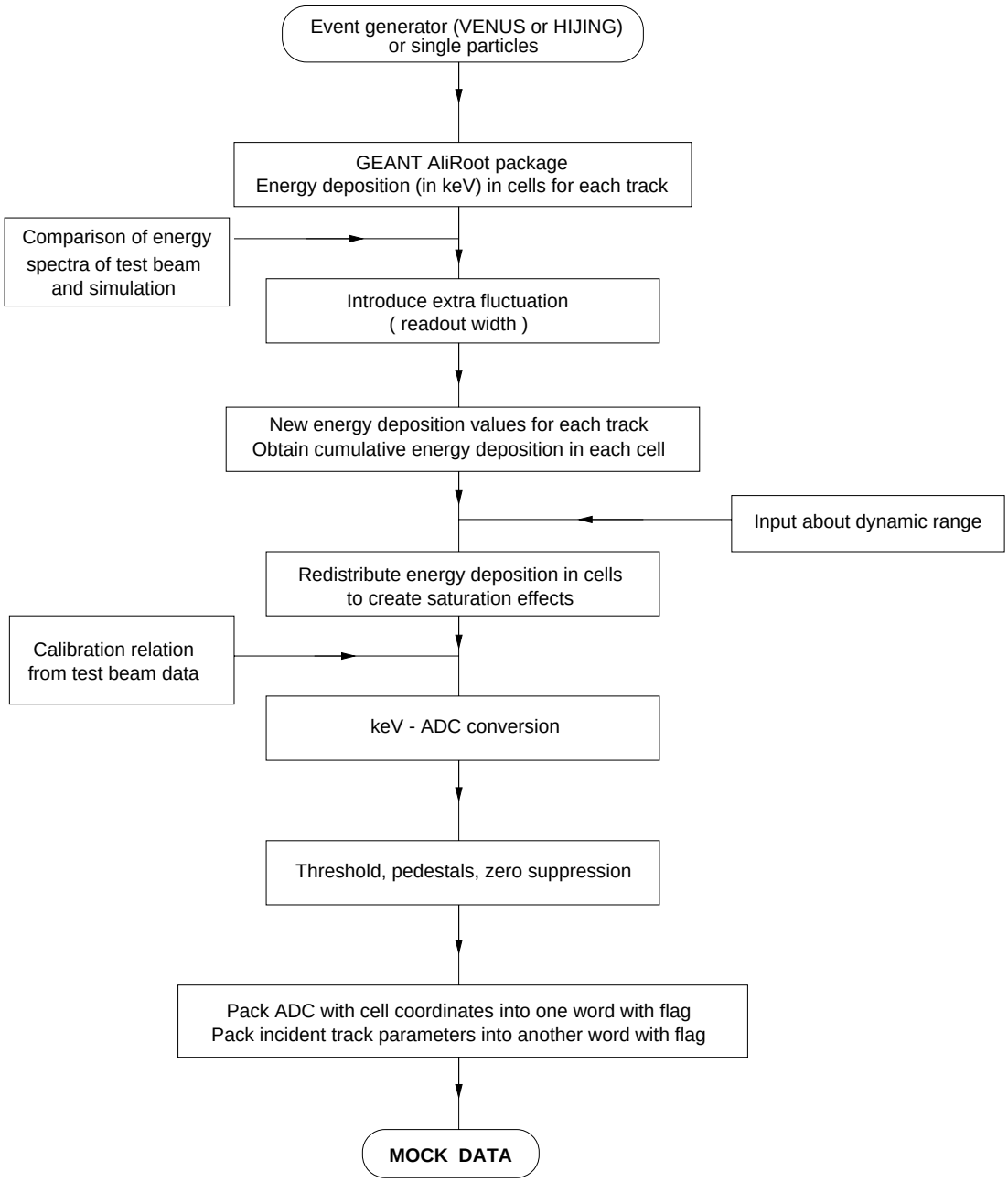

Figure 2.37: The flow diagram to produce mock data including all the effects of the detector and the readout.

3 Description of the PMD

The present chapter describes the mechanical design, fabrication and assembly procedures for the detector. The scheme for the implementation of the front-end electronics and data acquisition systems, trigger requirements for the PMD, and the procedure for on-line and off-line calibration of the detector are also discussed.

3.1 Mechanical design and construction

The PMD consists of the following mechanical parts [1]:

- honeycomb chambers (identical for the preshower and charged particle veto);
- lead converter plates;
- support assembly.

All the mechanical parts are made exclusively of non-magnetic materials. The entire detector is designed to have a vertical axis of symmetry, and the two halves can be independently assembled and installed. They have independent movements to open on the two sides of the beam pipe.

3.1.1 Honeycomb chambers

The honeycomb chambers will be fabricated in the form of unit modules which can be handled conveniently. These unit modules are designed for seamless integration with each other and several of them can be placed in a gas-tight supermodule. The supermodules will be transported to CERN.

3.1.1.1 Unit module

The unit module has been designed with the following considerations:

(a) ease of mechanical handling, fabrication and assembly,

(b) seamless joining with other modules to form a large uniform array and to have minimum dead spaces at the boundaries,

(c) number of channels in multiples of 64 for using multi-chip module (MCM) boards with 4-chip GASSIPLEX readout electronics.

A rectangular shaped hexagonal array has non-identical adjacent boundaries and cannot be joined without leaving considerable dead spaces. This can be seen from the picture in Fig. 2.8. Considering these aspects, a rhombus shaped module with 24×24 cells has been designed (see Fig. 3.1). This shape has identical boundaries on all four sides. The wall thickness at the boundaries is half that of the inner walls. When such arrays are joined together to form a supermodule, the half-thick boundary walls merge to form a seamless array of hexagonal cells as shown in Fig. 3.2.

3.1.1.2 Supermodule

The unit module with 576 cells is a rhombus of side approx. 260 mm. If one uses such modules as independent gas-tight units in a large number to cover the entire region of acceptance, the number of cells falling on the borders of the modules will be high. This will cause a large fraction of clusters to split at the boundaries, resulting in a reduction in the efficiency of photon counting. However, fabrication and assembly of a single large module in a clean environment involves a considerable increase in cost. In a rhombus structure the size is dictated by the larger diagonal. As a compromise we have adopted a scheme of building a supermodule with 3×3 unit modules joined together in a gas-tight enclosure.

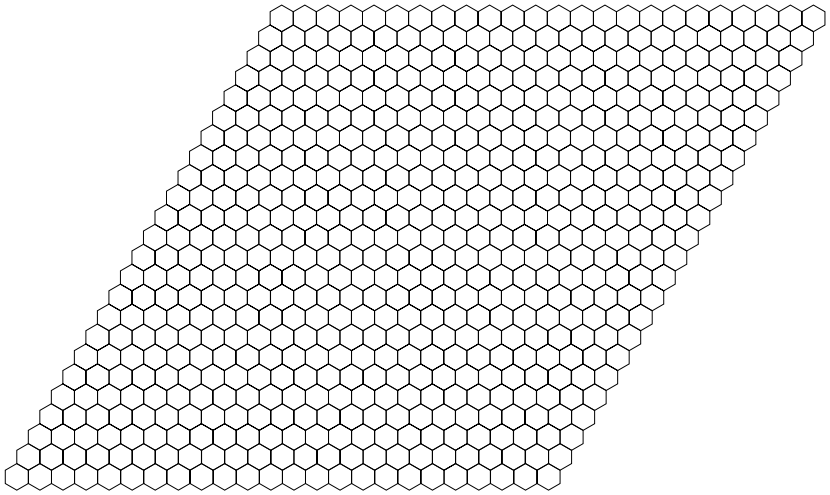

Figure 3.1: Rhombus shaped unit module containing an array of 24×24 hexagonal cells.

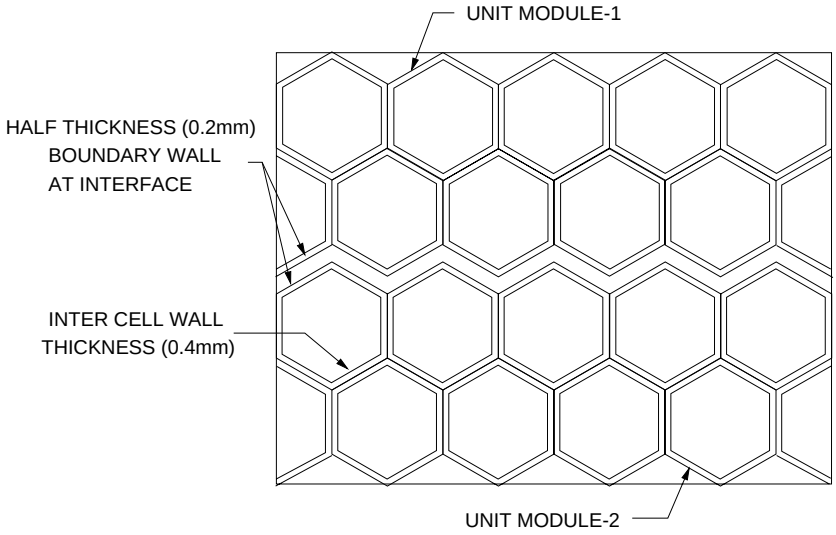

Figure 3.2: Expanded view showing the junction of two unit modules. The cell walls at the boundaries are half as thick as those inside and make a seamless joint with cells from the other unit module.

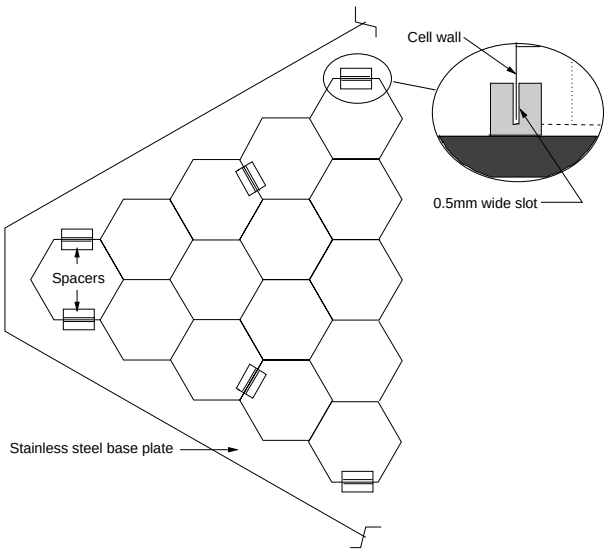

Figure 3.3: A schematic drawing of a 'go/no-go' jig used for testing the mechanical tolerances of the honeycomb array.

3.1.2 Fabrication of honeycomb array

The present requirements of a honeycomb are not readily available in industry. They only have aluminium honeycombs with very thin cell walls (0.075 mm). It was therefore decided to indigenously fabricate the honeycomb for this purpose using 0.2 mm thick ETP grade copper sheets.

Individual cells will be fabricated using a die-forming technique. The cells will be arranged in a high precision jig and spot-soldered to form a row of 24 cells. Twenty-four rows will be arranged in another fixture with proper staggering and joined together to produce a rhombus-shaped unit module. The finished unit module will be passed through a go/no-go type testing jig to check the dimensional tolerances as specified.

The 'go/no-go' jig consists of a flat machined stainless steel plate which has the size of a unit module and on which several spacers are brazed. The spacers are in the shape of a small cubical block of 5 mm side and a 4 mm deep and 0.5 mm wide slot is cut into it as shown in Fig. 3.3. After fabrication, the honeycomb array will be tested for a snug fit into all the slots of the jig from both faces. The arrays which do not engage into all the slots properly will be rejected.

The unit honeycomb module has stiff 1 mm dia. copper studs (fiducials) which are attached by reflow soldering. These studs are situated at eight different locations, four at the corners of the rhombus and four at the centres of each edge (see Fig. 3.4). They are used to bring out the high voltage connections of the cathode onto the PCBs. They also act as guides for attaching the PCBs on both sides of the honeycomb array, which ensures proper alignment. Small notches will be provided at the corners of each cell so that gas flows from one cell to another smoothly.

The copper honeycomb obtained from the manufacturer will be cleaned using soap solution and water in ultrasonic cleaners and then dried in warm air. The honeycomb cathode structure will then be dip-coated with high conductivity graphite paint. The thickness of the graphite paint is $\sim$10 μm. The paint dries quickly in air at room temperature. After this operation the honeycomb will be ready for assembly.

3.1.3 Assembly of a unit module

The components of a unit module are shown in Fig. 3.5. The steps in the assembly of a unit module are described in the flow chart of Fig. 3.6.

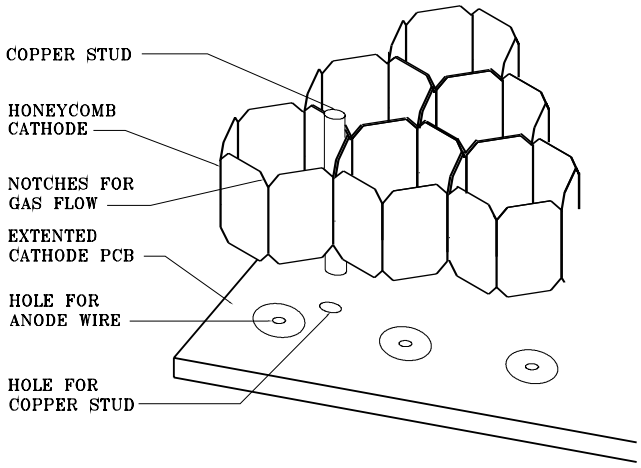

Figure 3.4: A close-up view of a small region of the cells in a unit module showing studs and notches in detail.

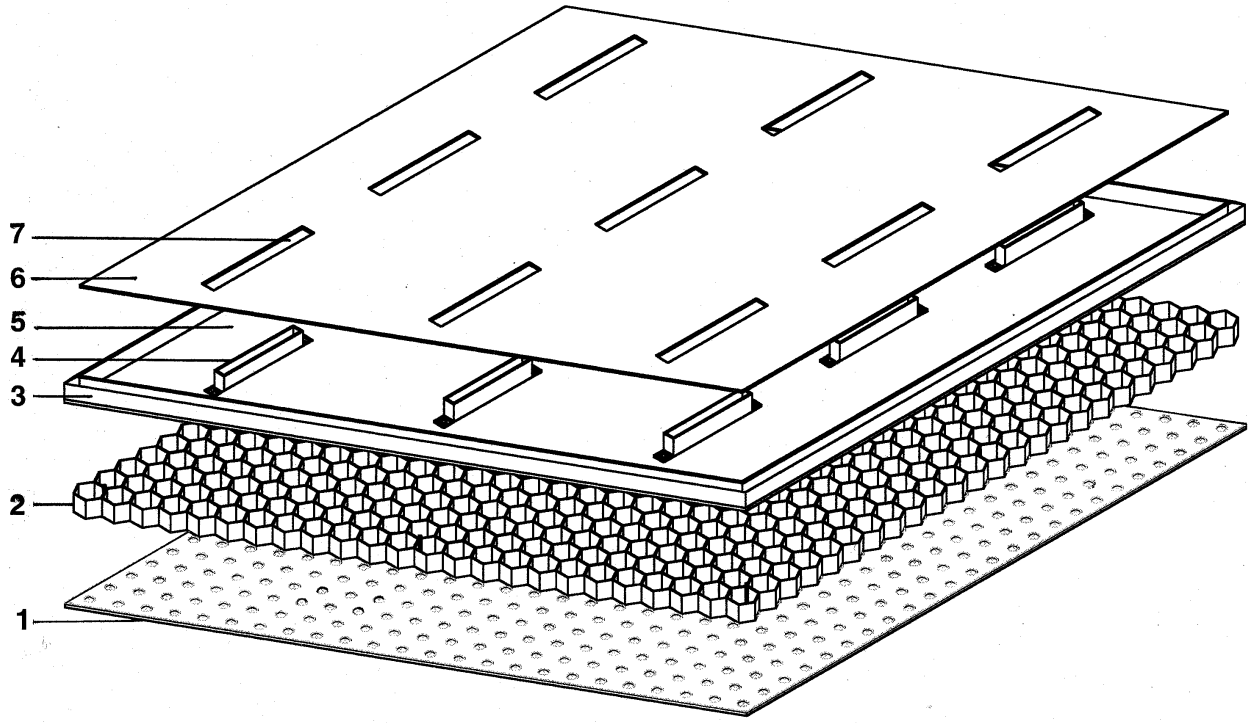

Figure 3.5: Expanded view of the unit module : (1) bottom PCB, (2) honeycomb cathode, (3) moulded frame, (4) ERNI connector, (5) top PCB, (6) shielding PCB, and (7) slot for connector.

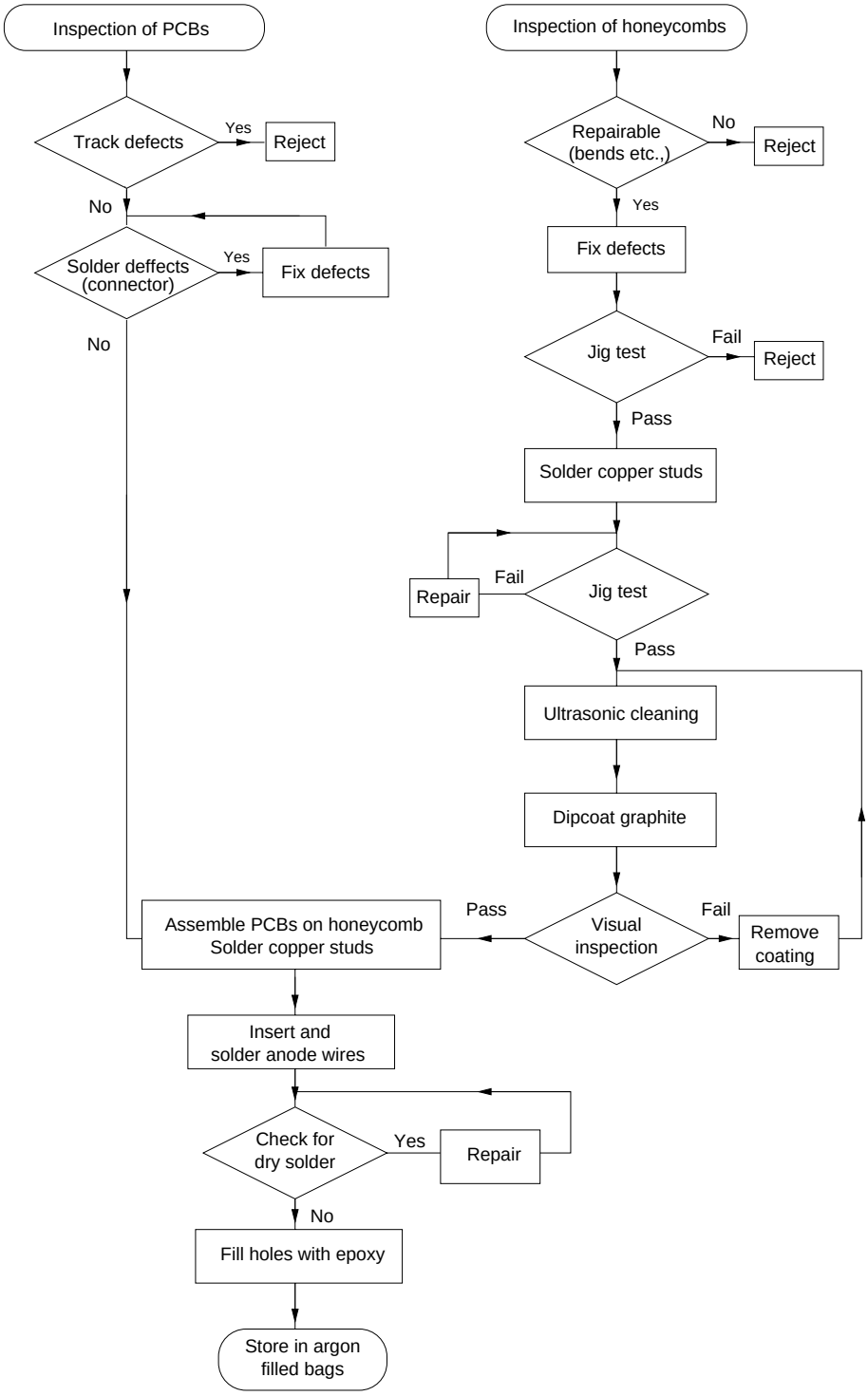

Figure 3.6: Flow chart showing various steps in the assembly of the unit modules.

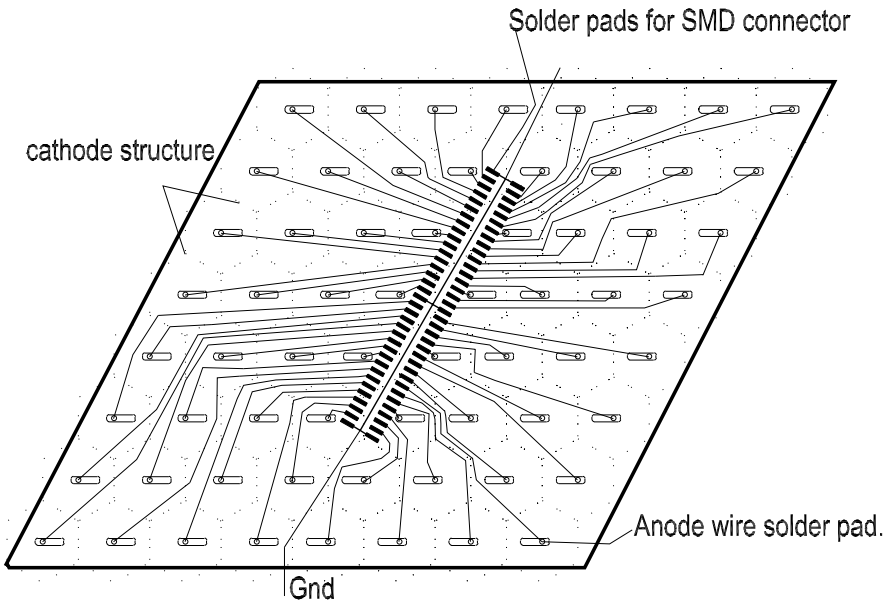

Figure 3.7: Wiring scheme for an array of 64 cells.

3.1.3.1 Clean area

In the present honeycomb design, contrary to large-area parallel geometry chambers, the cell boundaries have limited conductance for gas flow. Thus dust trapped within a cell during assembly may not be easily expelled by gas flushing and conditioning operations. The unit modules will therefore be assembled in a class 1000 clean environment to prevent dust entering the cells. Such a clean environment will be provided by laminar flow tables kept in dust and humidity controlled laboratories. The laminar flow tables will have a minimum working dimension of 1.5 m $\times$ 0.5 m. This infrastructure will be maintained at all centres where unit modules will be assembled.

All the groups participating in the fabrication of unit modules will be equipped with laminar flow tables with a working surface area of 1.5 m $\times$ 0.5 m.

3.1.3.2 Mounting the PCBs

The top PCB, containing the electronics boards, has solder-islands at the centre of each cell with a 0.4 mm gold-plated through-hole. Signal tracks from 64 cells are brought to a 70-pin 1.27 mm pitch surface mounted ERNI connector, as shown in Fig. 3.7. The PCBs on the bottom side have only soldering islands without signal tracks, serving as anchor points.

The moulded plastic edge frame is bonded to the top PCB plane of the unit module. This frame has a bevelled outer wall which provides a V-shaped cavity between the boundaries of the unit modules when brought in contact with another similar unit module.

The two PCBs are attached on both sides of the honeycomb, aligning with the copper studs. These studs protrude only 0.5 mm above the PCB surface and are soldered on the surrounding islands. The area is covered with insulated polyimide pads. This unit is now ready for anode wire insertion.

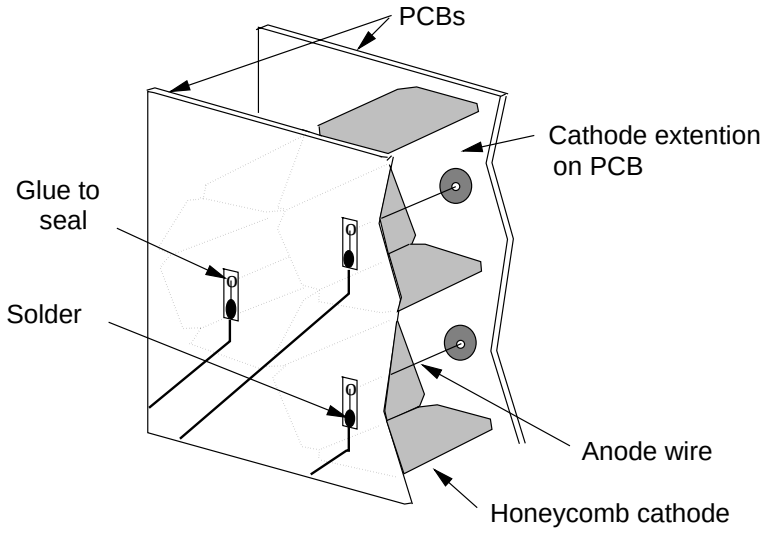

Figure 3.8: Expanded view showing details of wire soldering. The shaded circle around the anode wire represents the area where copper has been removed on the inner face of the PCB. Copper is present on the rest of the inner surface of the entire PCB and acts as an extension of the honeycomb cathode.

3.1.3.3 Wire insertion

The gold-plated tungsten wires (20 μm dia.) are first cleaned and wound onto a smaller spool as described in Sec. 2.2.2.2. This wire is then stretched through the holes on the PCBs, using a simple jig which provides tension to the wire. This is shown schematically in Fig. 2.10.

After applying tension to $\sim$ 30% of the elastic limit, the wires are soldered onto the islands on the PCBs about 3 mm away from the hole, as shown in detail in Fig. 3.8. The plated through-holes, where wires emerge, are then closed with a tiny amount of fast-setting epoxy to make them gas-tight. This scheme prevents creepage of solder flux into the cell and makes soldering easier.

At the end of the assembly, all the soldered joints are tested for dry solder using a milli-ohmmeter. Defects, if any, are repaired at this stage.

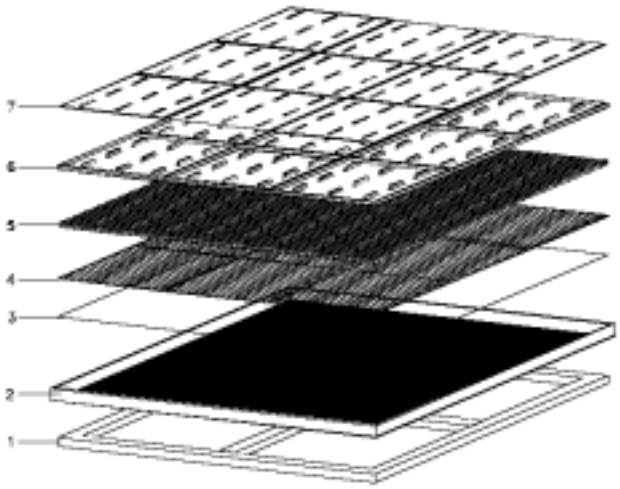

Figure 3.9: Expanded view of the components of a supermodule: (1) base frame, (2) bottom plate with boundary wall, (3) insulating sheet, (4) lower PCBs, (5) honeycomb chambers, (6) top PCBs, and (7) shielding planes.

3.1.4 Assembly of a supermodule

Each assembled unit module will be sealed in a plastic enclosure, formed to match the shape and contours of the module, using thin rigid plastic packaging material. The enclosures will be filled with argon gas before sealing for transportation and storage before assembly into supermodules.

A supermodule consists of a 3×3 array of unit modules bonded in a gas-tight enclosure made of 2 mm thick SS sheet with a 6 mm thick and 30 mm high aluminium boundary wall. The components of a supermodule are shown in Fig. 3.9. One cell each at the four corners of the supermodule is retained without anode wire, to allow screws to pass through a welded gas-tight SS tube for fixing the supermodules onto the support plate.

3.1.4.1 Assembly procedure

The flow-chart for the assembly of a supermodule is shown in Fig. 3.10. These are explained in the following paragraphs.

- The supermodule chamber is prepared by attaching the boundary wall to the bottom plate with screws and epoxy. The bottom plane is insulated with 50 μm thick polyimide film. The opposite boundary walls are prefixed with gas feed and return connectors.

- A base frame made of 50 mm $\times$ 25 mm aluminium channels is fixed to the bottom to retain the planarity of the bottom sheet during further operations.

- The chamber is placed on a planar graphite table. Nine assembled unit modules are placed to fill the inner area of the supermodule enclosure, leaving a 1 mm gap on all sides to accommodate general assembly tolerance and to provide insulation between the honeycomb cathode and the boundary. Several polyimide spacers are inserted into this gap all along the boundary to arrest any movement of the unit modules and also to insulate the honeycomb cathode from the walls.

- The V-shape groove formed at the junctions of all the unit modules are filled with high viscosity silicone adhesive compound. The contact area between the outermost boundaries of the unit modules and the inner boundary wall of the supermodule enclosure is also filled with silicone adhesive. Retaining clips are then attached to the adjacent unit module frames to add to the mechanical strength. This is shown in Fig. 3.11.

- One corner of the supermodule chamber is marked to denote the origin of the rhombus array. The x-coordinate increases towards the right and the y-coordinate increases upwards. The origin mark is used to orient the supermodule during installation so that one-to-one correspondence is established between the physical coordinates of the cells and the coordinates implemented in simulation.

- Three aluminium channels are then fixed across the supermodule surface to retain all the unit modules firmly in position. These cross-members are anchored at the sides of the 6 mm boundary frame and on top of each retaining clip at the unit module junctions.

- A small plastic enclosure containing one SHV connector, an HV limiting resistor (2.2 MΩ) and decoupling capacitor (2.2 nF) is now fixed at one corner of the supermodule very close to the HV tapping point.

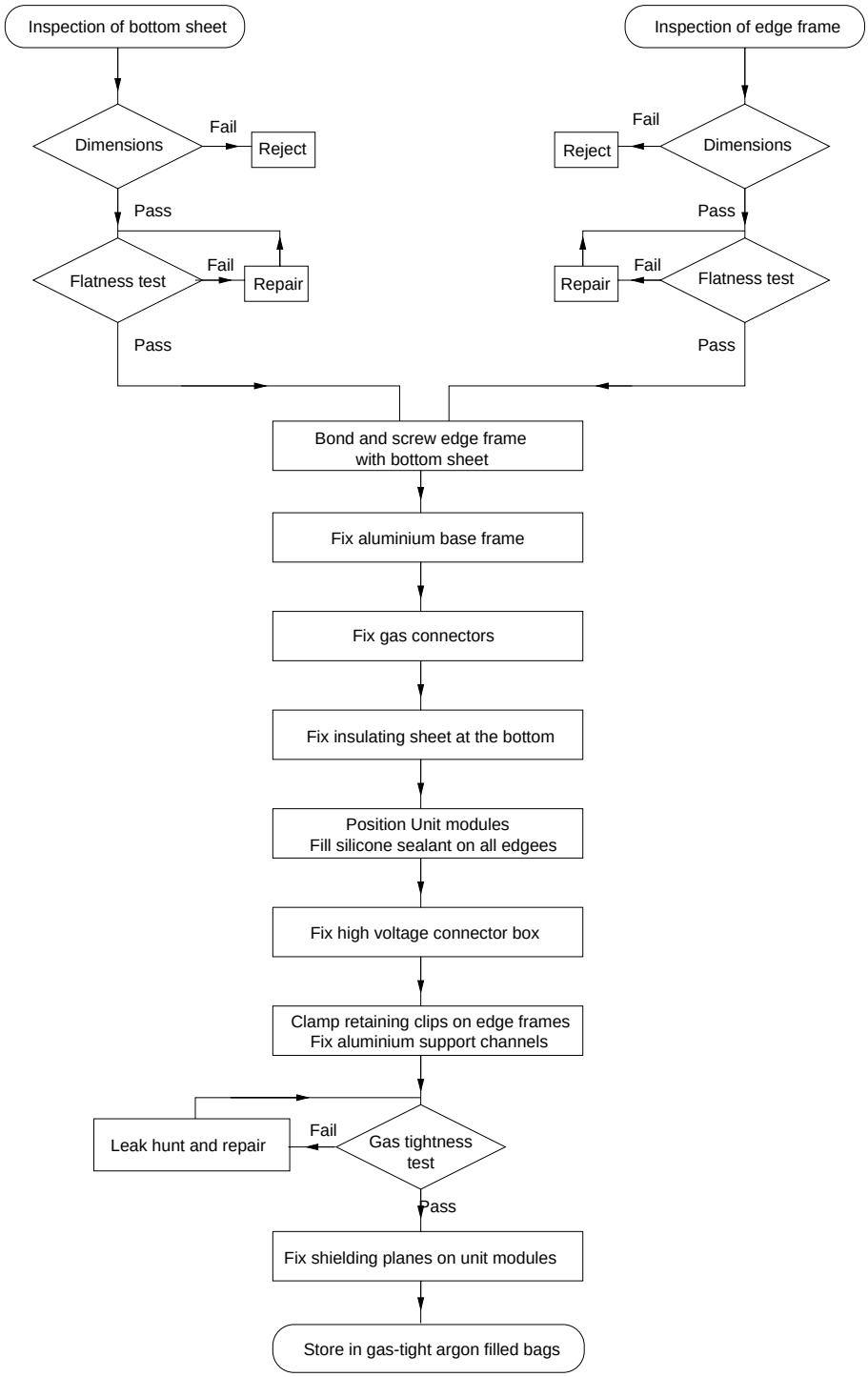

Figure 3.10: Flow chart showing various steps in the assembly of the supermodules.

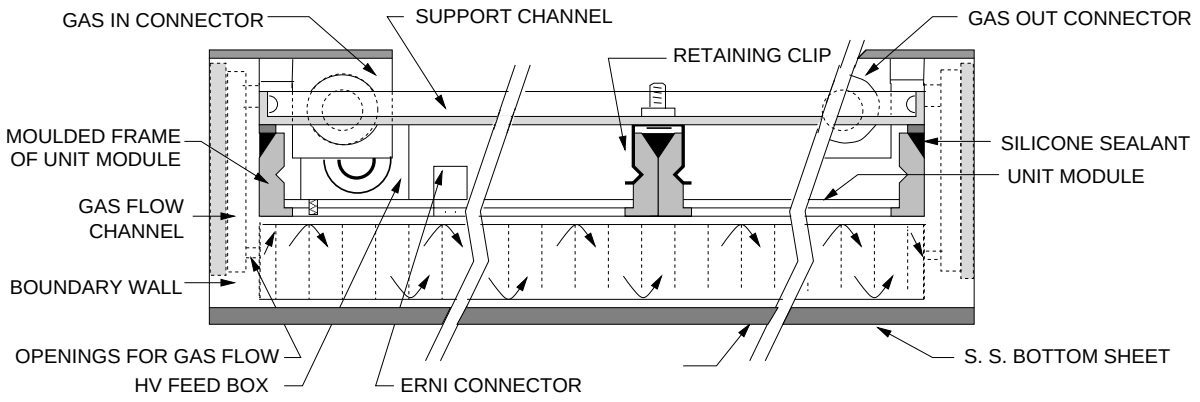

Figure 3.11: Schematic of a section of the supermodule showing different components such as gas inlet, high voltage feeder, support channels, and sealing for gas tightness.

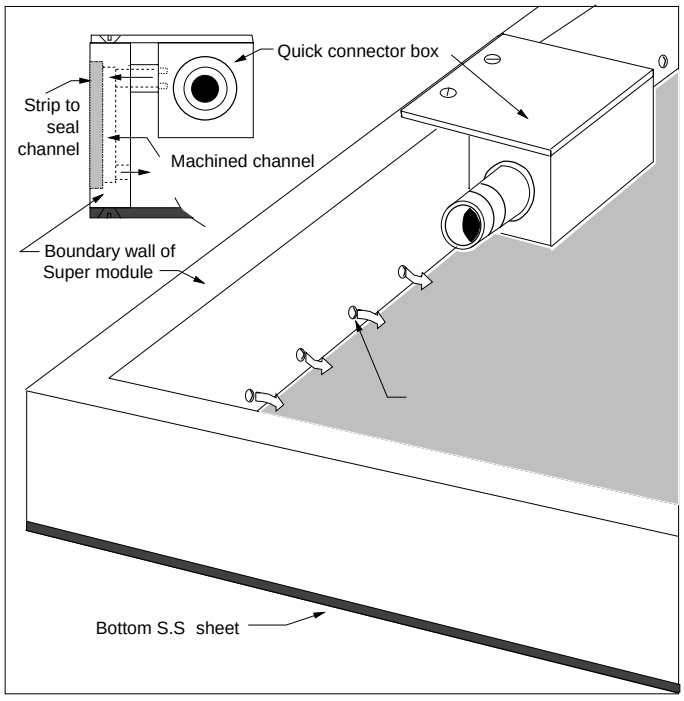

Figure 3.12: Gas feed sub-assembly placed at the top of a supermodule.

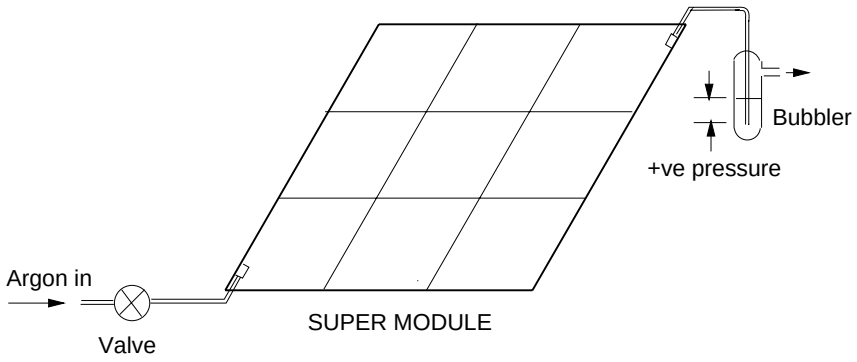

Figure 3.13: Set-up for leak detection in a supermodule.

3.1.4.2 Gas flow within a supermodule

The opposite sides of the boundary wall of the supermodule enclosure have gas-feed channels as shown in Fig. 3.12. Each channel has 24 openings into the chamber. The gas flow impedance for the entire chamber is kept low by incorporating the following schemes:

– small notches are provided at the corners of each cell (as described previously, see Fig. 3.4) so that gas flows from one cell to another smoothly,

– gas is fed through the connector at the end of the long gas feed channel. It enters all the entry points in the channel simultaneously, at a depth of 4 mm from the bottom of the chamber. It then flows through the notches and exits at the other edge of the supermodule through the 24 output channels.

3.1.4.3 Leak detection

The leak rate of the assembled supermodule is tested using the scheme shown in Fig. 3.13. The chamber is filled with Ar by connecting it to the gas supply line through a valve. The bubbler on the return line has silicone oil filled up to 20 mm above the outlet nozzle, representing 2 mbar of over-pressure. After a steady flow rate is established in the chamber, the valve is closed and the chamber kept under observation for a drop in pressure. By measuring the time required for a 1 mbar drop in pressure and knowing the volume of the chamber, the leak rate can be estimated.

If the leak rate is found to be beyond the specified limit, further tests will be carried out with a portable gas leak detector, having a sensitivity of 10^{-3} cc/s for argon, all along the joints of the unit modules. Corrective measures will be taken to make the chamber gas-tight within the allowable limits.

3.1.4.4 Wire testing

The PMD chambers will be operated at $\sim$ 2 mbar above atmospheric pressure. This may lead to some extra stretching of the wire and subsequently the tension may fall below the desired level affecting the performance of the chamber. In addition, some wires may slacken or even break during transportation. Hence tests of broken and loosened wires are necessary.

After the unit modules are inserted in the supermodule chambers, only one end of the wire is available for contact through the ERNI connectors. This imposes constraints on the methods of testing. Several methods are under investigation.

Tests using an audio signal

Figure 3.14 shows two test set-ups using an audio signal, the one on the left can be used when both ends of the wire are accessible, and the one on the right can be used with supermodules when only one end is accessible. The method is based on the principle that (a) a peak exists near resonant frequency of

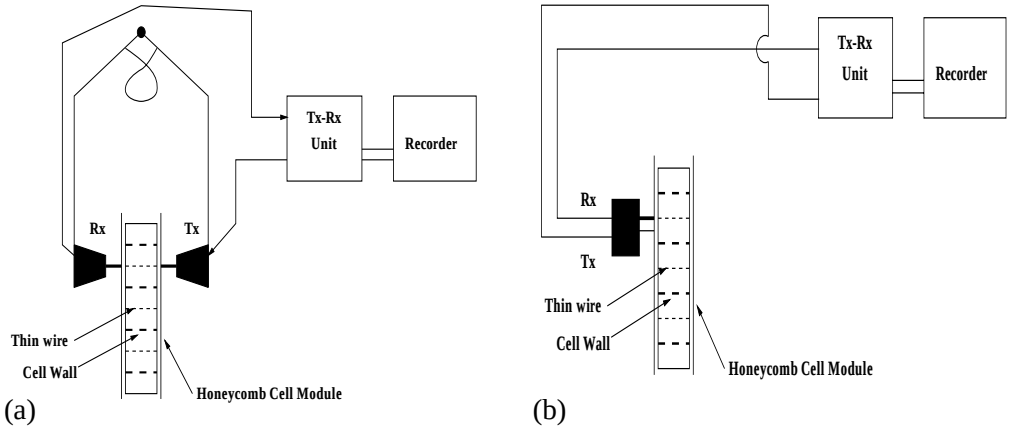

Figure 3.14: Wire testing using an audio signal: (a) when both ends are accessible and (b) when only one end is accessible.

the thin wire, (b) the path length for sound propagation along the thin wire is very small compared to the path lengths in other media, and (c) the velocity of sound in the respective media are very different.

The basic electronic circuitry for both methods are identical, but the sound wave injection and reception are different. The set-up requires a wide-range audio oscillator with buffer amplifier for audio signal generation, and a precision audio amplifier with a narrow-band pass filter and a phase-locked loop amplifier in the reception stage.

Tests using magnetic field

A Lorentz force is generated to excite the wire mechanically by sending an impulse current through the wire kept in a magnetic field. The induced signal on the wire due to damped transverse oscillations of the wire are analysed to obtain an estimate of the tension [2]. In the present chambers the wires are transverse to the larger area surface. Hence the magnetic field cannot be applied perpendicular to the wire unless one uses a magnet with a very large pole gap. The chamber will be placed at an inclination so that a component of the magnetic field is applied perpendicular to the wire.

Replacement of unit modules

The supermodules will be subjected to several cycles of over-pressurization during leak tests. This will also allow us to assess the strength of the chamber. After this cycle all the wires will be tested for tension. Although repair of broken/loosened wires is not foreseen after assembly of the supermodules, unit modules will be replaced if the number of broken wires exceeds 5%.

Disassembly, if required for the replacement of the unit modules, can be performed by following the procedure given below:

- remove all the retaining clips and aluminium channels,
- scoop out the silicone adhesive around the defective unit module, and simultaneously remove the debris with vacuum suction, and
- lift the defective unit module for replacement.

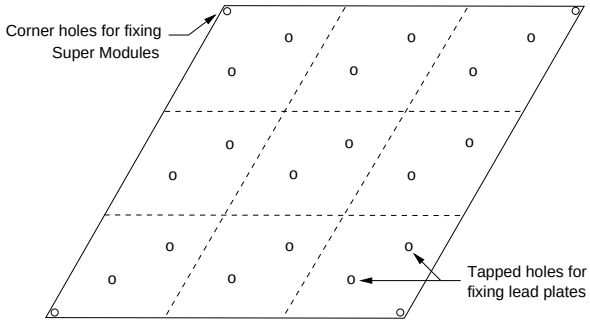

Figure 3.15: A section of the support plate with holes for lead plates and honeycomb chambers.

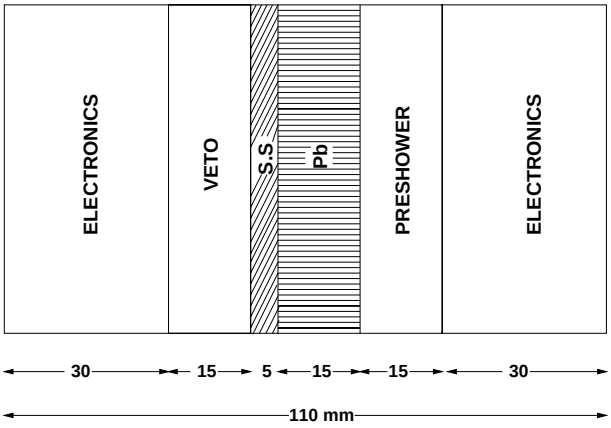

Figure 3.16: A cross-sectional view of the PMD.

3.1.4.5 Handling and transportation

The supermodules will be stored within argon-filled plastic enclosures. The base frame will remain attached during storage and transportation to CERN. This frame will be removed only at the time of mounting the modules onto the support plate during installation at the experimental site. Packaging will be provided to prevent any undue pressure and jerks during transportation and handling.

3.1.5 Support assembly

The support assembly has two parts [1]: (a) the support plates, and (b) the suspension and movement mechanisms.

3.1.5.1 Support plate

A 5 mm thick flat stainless steel plate is used to support the lead converter plates and the supermodules in each half of the PMD. A section of the support plate covering the area of a supermodule is shown in Fig. 3.15. Each small rhombus represents one lead plate. The lead plates are fixed with the help of two bolts. The holes at the corners are used to fix the supermodules onto the support plate. A cross-sectional view of the PMD is shown in Fig. 3.16. The procedure for mounting the converter plates and the supermodules onto the support plate is described in Chapter 5.

3.1.5.2 Suspension and movement mechanism

The suspension mechanism for the PMD is designed to handle a total weight of 6000 kg and will be fabricated from exclusively non-magnetic components. It is shown in Fig. 3.17.

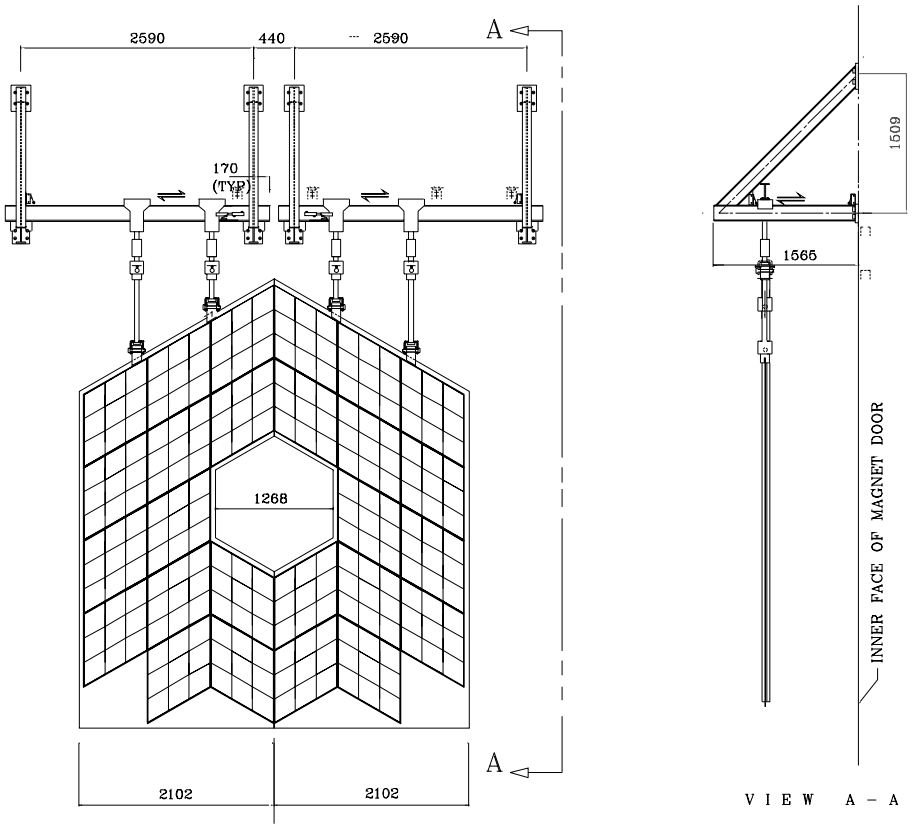

Figure 3.17: Hanging mechanism of the PMD.

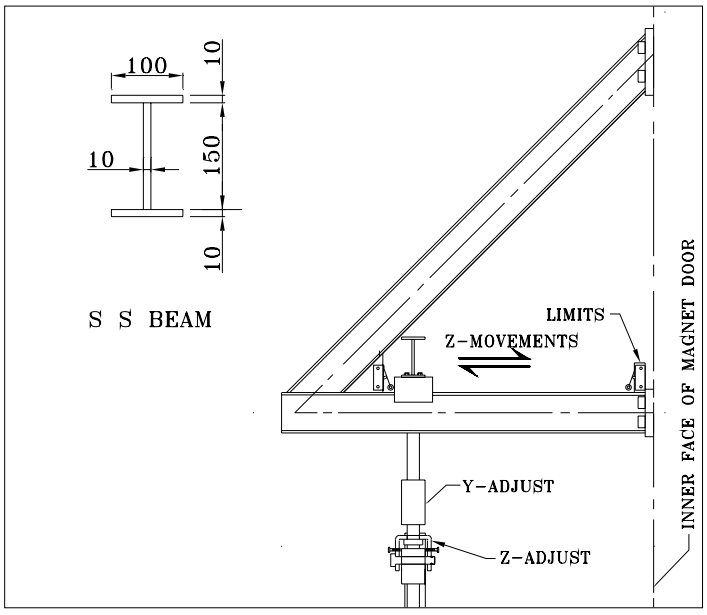

Figure 3.18: Hanging mechanism of the PMD showing movement along the *z*-direction.

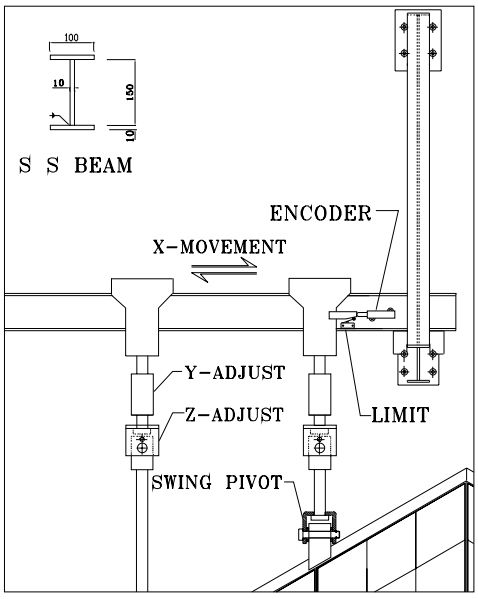

Figure 3.19: Hanging mechanism of the PMD showing movement along the *x*-direction.

This structure consists of four 'V'-shaped, load bearing 'I' beam supports fixed firmly to the magnet doors (two on each side). Two cross 'I' beams, supported on these structures, move along the *z*-direction to a span of 1 m from the face of the magnet door (see Fig. 3.18) to generate access space behind the detector for maintenance. The two halves of the detector are supported on the cross beams and hang freely in a vertical position. Each half of the detector can be separated for access by a smooth independent *x*-movement on the cross beam. The hanging elements have free swinging pivots, fine adjustments for horizontal motion, and plane position adjustments for alignment of the detector (see Fig. 3.19). The services for the two halves (cables, gas lines, etc.) are also independent.

The two halves will hang with a 2 mm separation between them. This will be controlled using limit switches. All movements will be carried out by hydraulic motors. The details of non-magnetic hydraulic components are being worked out.

3.1.5.3 Repositioning and calibration

The two halves of the PMD will require frequent *x*-movement to allow short-time access to the magnetic cave. The movement will be remotely controlled and the halves must be returned to their original position. A cumulative tolerance of 5 mm will be provided for repositioning. The final position of the two halves will be read through linear encoders situated on the beams. The motion is controlled by a coarse and a fine movement. Using coarse movement the two halves are brought within 25 mm when limit switches placed on both halves are actuated. This allows switching over to fine movement along with linear encoder reading. The two halves are brought to the final position by using feedback from the encoder.

3.1.6 Converter plates

Lead converter plates will be machined in the form of rhombuses of side 265 mm. This size has been selected so that (a) an integral number of lead plates fill the area of a supermodule, and (b) each piece weighs around 10 kg which is convenient to handle during installation. There will be through-holes in the lead plates at the positions where the supermodules will be fixed with the support plate. The supermodules for the preshower and the veto detectors will be mounted back-to-back on a support plate.

3.2 Front-end electronics and readout

The front-end electronics for the readout of the PMD signals is based on the use of 16-channel GASSIPLEX chips [3]. The suitability of this chip in terms of linearity and dynamic range has already been discussed in Chapter 2. The implementation of the front-end electronics and data handling will be closely based on the scheme developed for the tracking chambers of the dimuon spectrometer [4] which also use the same signal processing electronics. We describe here the features specific to the PMD detector and the procedure for tests and assembly of the electronics.

3.2.1 General structure of the readout system

The readout system is structured in three levels:

- Level 1: Multi-chip module (MCM). This resides closest to the detector. One MCM handles up to 64 analog inputs. It performs analog processing, ADC conversion, pedestal subtraction, zero suppression, data formatting, and transmission to the digital signal processor (DSP) via the digital local bus.
- Level 2: Digital Signal Processor (DSP). The local buses collect the data from MCMs. A maximum of 24 MCMs can be connected to a bus. Several buses run through each chamber, making the data available to DSPs located on the edge of the detector. Each DSP can handle up to 6 buses.
- Level 3: Cluster. The DSPs are assembled onto cluster boards. Each cluster contains up to 6 DSPs. The whole cluster board can hence process up to 36 buses. The cluster boards communicate with the PMD's top level read-out receiver cards (RORCs) cards through optical links. These links, called detector-data link (DDL) have a bandwidth of 100 MHz.

3.2.2 Multi-Chip Module

The function of the multichip module is to gather signals from 64 cells, process the analog signals through charge amplifiers/shapers, convert the data into digital values, remove the pedestal, and transmit the zero-suppressed data to the upper level. It is embedded directly on top of the detector.

The module is composed of three sections:

- A set of four 16-channel preamplifier/shaper/multiplexers (GASSIPLEX or MANAS-16).
- A 12 bit Analog to Digital Converter (ADC).
- A complete custom designed digital processor (MARC).

3.2.2.1 Analog front-end electronics (GASSIPLEX and MANAS-16)

The GASSIPLEX signal processor, developed at CERN [3], is well adapted to gaseous detectors. Whereas for prototype tests we have used both old and new versions of GASSIPLEX, we propose to use the version MANAS-16, being developed in India, for the final detector.

MANAS-16 (Multiplexed ANAlog Signal processor), a new version of the front-end electronics, is conceptually similar to GASSIPLEX. With useful modifications like high-voltage isolation and a calibration capacitor on each channel, it is under development by the Indian team of the ALICE experiment. It comprises 16 charge preamplifier/shapers, each followed by a track and hold gate. An analog multiplexer, with its associated control logic makes the signals available at the output. It is described in detail in Ref. [4].

MANAS-16 has been designed taking into consideration its application for negative input signals for use in the PMD. Simulation results for negative input are shown in Fig. 3.20. The chip is expected to be

Table 3.1: Specifications of MANAS-16 chip

Item	Value
Dynamic range	–250 fC
Gain	3.3 mV/fC
Peaking time	1.2 μs
Baseline recovery (1%)	4.5 μs
Power dissipation	9 mW/ch
Analog readout speed	10 MHz
V_{dd}/V_{ss}	$\pm$2.5 V

linear up to 300 fC of input charge as in the parent GASSIPLEX chip. The specifications of MANAS-16 for negative input signal are given in Table 3.1.

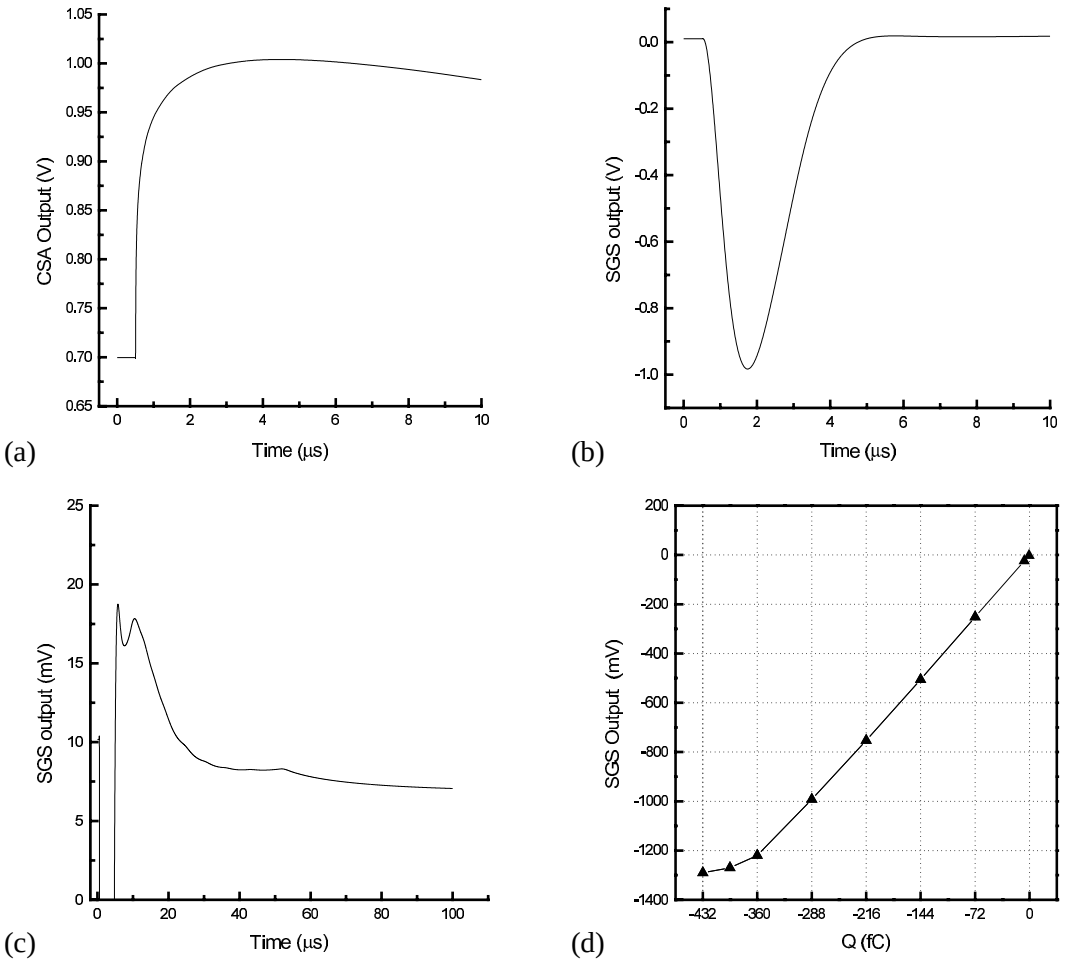

Figure 3.20: MANAS-16 simulation results for negative input from a gaseous detector: (a) charge sensitive amplifier (CSA) stage, (b) pulse from the semi-gaussian shaper (SGS), (c) baseline restoration, and (d) SGS output vs input charge showing linearity of response up to 300 fC.

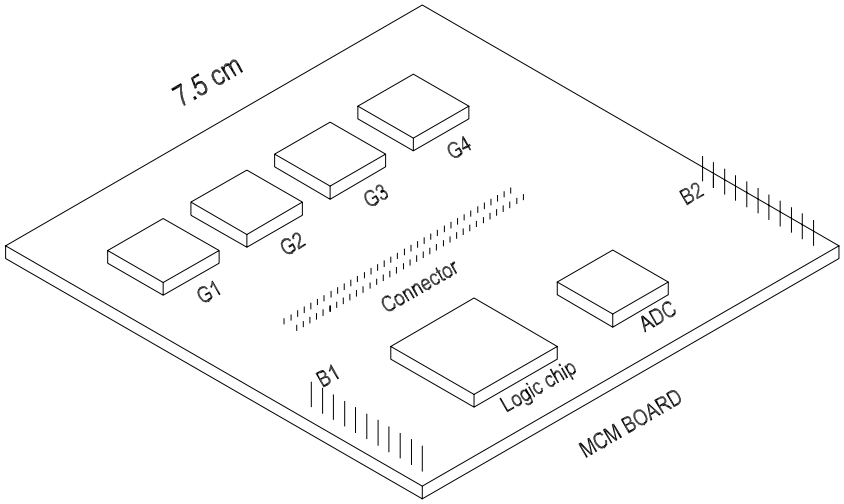

* **Figure 3.21:** PCB layout for the MCM board of the PMD.

3.2.2.2 Digitizer (ADC)

The digitizing function is performed by a commercially available 12 bit successive approximation ADC. The conversion time is 500 ns per channel.

3.2.2.3 Digital readout chip (MARC)

Each MCM contains a digital readout chip (MARC - Muon Arm Readout Chip) which controls the four GASSIPLEX and the ADC, performs zero suppression on the data, and communicates with the DSP through a 4-bit bidirectional bus.

The pedestal values are stored in a 64 word $\times$ 12 bit RAM. The 12 bit ADC words are latched in a temporary input register and compared with the pedestals. Data above threshold are then stored in a 64 words $\times$ 18 bit FIFO together with the 6 bit channel address. The data extracted from the FIFO are merged with the 11 bit MCM address word, a parity bit, and two control bits. The resulting 32 bit word is sent to the DSP as 8 nibbles of 4 bits each.

The chip can be configured and controlled by the DSP through a command-based protocol.

3.2.2.4 MCM board

The cells in a supermodule are organized in rhombus arrays. Thus a cluster of 8 $\times$ 8 cells also forms a rhombus shape. Hence the PCB layout of the MCM board designed for rectangular segmentation in Muon Arm tracking chambers has to be modified for use in the honeycomb chambers of the PMD.

A block diagram of the modified MCM board is shown in Fig. 3.21. The board is a rhombus of 75 mm side. The 70-pin ERNI connector is located at the centre of the board. The analog chips G1–G4 are located on one side of the connector and the digitizer and the logic chips as well as daisy-chaining connectors B1, B2 are located on the opposite side.

The board area is $\sim$ 48 cm^2 which is twice the area of the MCM board of the Muon Arm tracking chambers. Thus there will be less heat per unit area in the present case. The heat load will be uniform throughout the surface on both sides of the detector. Heat will be removed by water cooling.

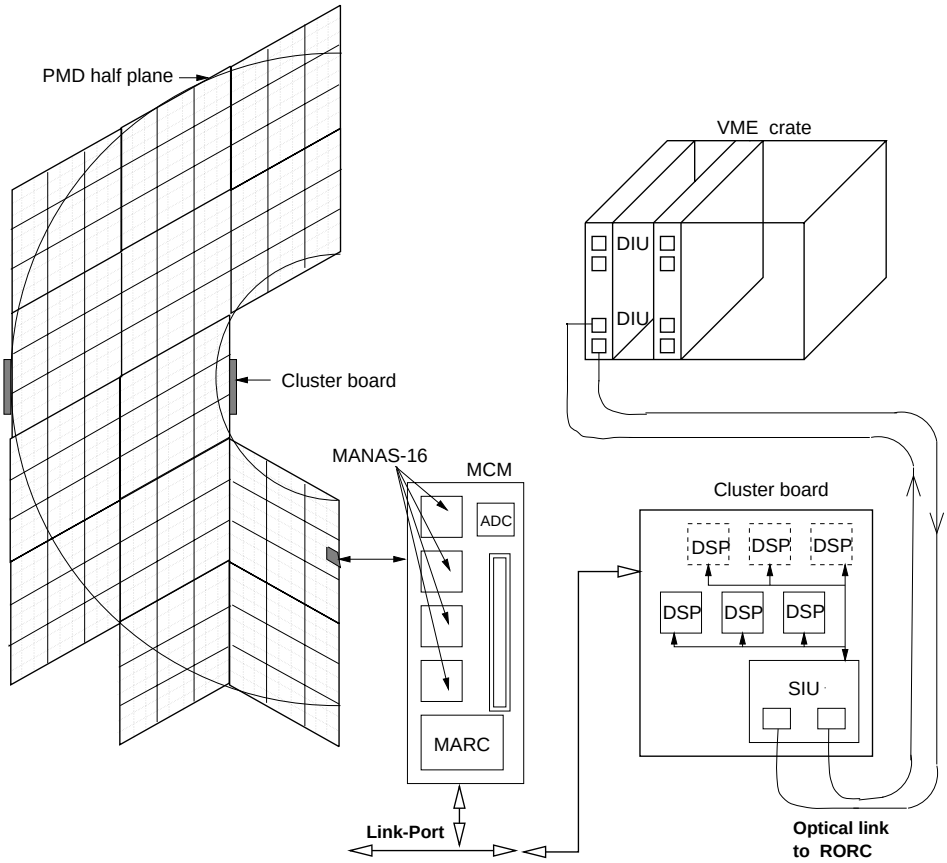

Figure 3.22: Schematic layout of the readout scheme for one-half plane of the PMD showing the requirements of the MCMs and DSPs. Each small rhombus represents one MCM board. There will be three DSPs in the cluster board for the preshower plane and six DSPs for those of the veto. In total there will be six cluster boards, four on the preshower and two on the veto.

3.2.3 Cluster board

The valid data from the MCM boards are transmitted onwards by the use of DSPs located on the cluster boards and connected with the MCMs by local buses. Each DSP board will in turn be connected to a DDL card for onward connection to the ALICE data acquisition system.

3.2.3.1 Cluster processor board

The scheme of connections from the MCM on the detector to the DSP cluster board situated at the inner and outer edges of the support plate are shown in Fig. 3.22. The purpose of this board is to handle the local buses, gather several DSP processors together, receive and distribute the hardware trigger signals, and communicate with the upper level through a DDL optical link.

The board will comprise a total of 4 DSPs for the preshower plane and 7 DSPs for the charged particle veto. In each case, one of the DSPs will act as the master processor and will manage the DDL communication through an SIU daughter card. All low-level hardware interfacing will be performed by programmable logic devices.

The DSPs will be of the ADSP-2106x series (SHARC) from Analog Devices. All processors on a cluster board will be linked together, using the cluster multiprocessing concept. One of the DSPs will act as the host processor. In this mode of operation, all the DSPs have access to a single unified memory space, allowing for common memory communication and process synchronization with no overhead. The link-port high speed serial link will be used for direct interface with the chambers MCMs. All the

ports can transmit data simultaneously at full speed, including within the same DSP.

3.2.3.2 Local data bus

The bus is of single-master multi-slave configuration. It features bidirectional communication between the DSP and the MCM. In one direction it permits the downloading of parameters such as threshold and individual pedestal values for each channel into the MCMs. In the other direction, the MCMs communicate the zero-suppressed readout data and status information to the DSPs.

The elementary communication data consist of a 32-bit frame divided into eight 4-bit bus transactions. A readout datum contains four fields: header, address, channel id, and 12-bit data. The data is transferred at the rate of 20 Mbyte/s. The details of the hardware implementation and protocol can be found in Ref. [4].

3.2.3.3 Isolation of MCM

The complete MCM comprises 4 MANAS-16 chips connected together by their analog bus. In order to improve reliability, each chip is controlled separately and not through daisy-chaining. This allows the software disable of a single unit in case of failure.

3.2.3.4 DDL interface

The DDL is a standard ALICE DAQ component that connects the front-end electronics of the detectors to the main DAQ system [5]. The DDL will be handled by the master processor through a SIU daughter board which will form a part of the cluster board on the PMD.

3.2.4 MCM assembly and tests

The MCM assembly consists of testing the chip and categorization according to pedestal values, assembly of board, and testing of the assembled board.

3.2.4.1 Chip tests and sorting

A comprehensive set-up for testing individual chips has been developed at VECC in collaboration with CERN [6]. The test set-up including the test board (CERN-ECP-680-1058-800) is shown in Fig. 3.23. The chip to be tested is mounted on the test board.

An indigenously developed control unit generates the control signals (Clock, Clear, Track/Hold) in NIM fast logic standard on receipt of a trigger input. This can be fed from a Tail Pulse Generator (BNC-BH1). These control signals must be connected to the Level shifter/Repeater board. The repeater has been used to allow parallel operation of many chips by duplicating the low voltages and control signals. The level shifter has been used to shift the control signals to the levels operated by GASSIPLEX operation i.e. +2.75 V, -2.75 V and GND. A minor adjustment will be required for the new chips operating at ± 2.5 V.

The trigger output of the pulse generator is connected to the second pulse generator input (EXT TRIG IN) keeping it in Ext Trig/SC mode and also to an oscilloscope for monitoring. The negative (or Positive) output of this pulse generator (BNC 9010) is used as a test signal. The control unit can be used to select the number of clocks up to a maximum of 256, i.e. 16 chips can be daisy-chained. The control unit is being modified to incorporate a self trigger. This will avoid the need of a tail pulse generator. The modifications will also incorporate clock selection up to a maximum of 1024 channels so that a large number of chips can be chained for tests.

With this test set-up one can test the chips individually for power consumption, full functionality, clock-out, output d.c. level measurement, pedestal spread, sensitivity, linearity, peaking time measurement with bias resistance, variation of d.c. level with temperature, and dynamic range. The test pulses

can be sent to all the channels through a calibrated capacitance via a common test input line. While doing this the control signal from the level shifter and repeater boards must be connected to corresponding LEMO connectors on the test board.

Before the chips are mounted on the MCM board, they are grouped into three classes depending on pedestal spread: (a) pedestal spread < 80 mV, (b) pedestal spread between 80–120 mV, and (c) pedestal spread > 120 mV. Large discrepancies in the pedestal values among chips lead to loss of dynamic range. Only chips from the same group are mounted on the MCM board.

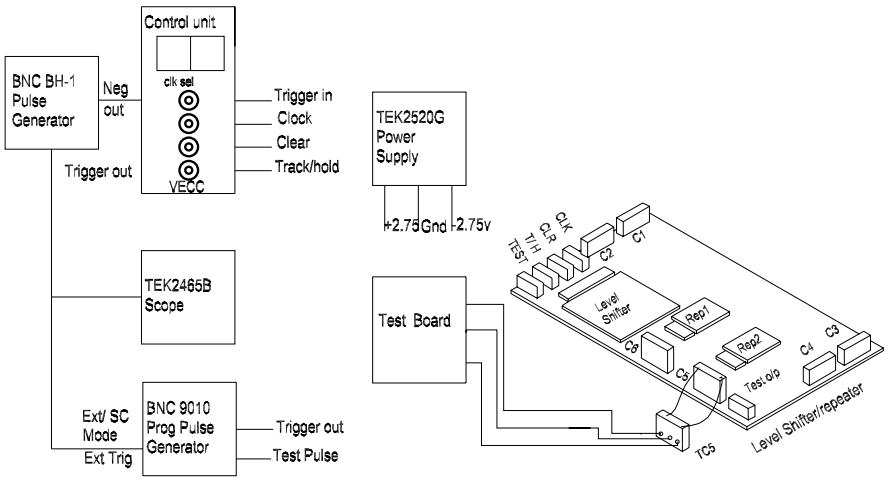

Figure 3.23: Block diagram of the test set-up for GASSIPLEX chips.

3.2.4.2 Assembly and tests of the MCM board

The assembly of the MCM boards will be carried out by industry using automatic surface mount and hot-air soldering techniques. Testing procedures for the assembled board containing MANAS-16, ADC and MARC will be developed in collaboration with the Muon Arm tracking chamber groups.

3.2.5 Trigger and data acquisition

3.2.5.1 Trigger requirements for the PMD

The PMD is designed to take data at the highest possible rate available in ALICE. This is required to achieve high statistics for searching exotic events. The trigger rates are described in detail in Ref. [4]. The expected rate will be about 650 Hz, although a maximum rate of 1000 Hz is foreseen. The PMD will take data in conjunction with the barrel detectors as well as with the Muon Spectrometer.

The PMD employs GASSIPLEX electronics for readout. It requires all three triggers for the following functions:

- Level 0: to strobe the track/hold stage of GASSIPLEX.
- Level 1: to clear the electronics if interaction is discarded.
- Level 2: to start transfer of data from the DSP to DDL if the event is accepted for recording (L2y) or to clear the entire buffer if the event is rejected (L2n).

Table 3.2: Data volume and time of transfer for PMD

Parameter	Pb+Pb Central	Pb+Pb Min. Bias
Data rate		
Event size	120 Kbytes	30 Kbytes
L2 rate (TPC)	40 Hz	40 Hz
L2 rate (Muon)	300 Hz	700 Hz
Total L2 rate	340 Hz	740 Hz
Data volume	40.8 Mbytes	22.2 Mbytes
Time of transfer		
Average no. of words per MCM	12	3
No. of words per bus	288	72
Start of digitization	2 μs	2 μs
MCM digitization	32 μs	32 μs
Transfer to DSP	58 μs	15 μs
Overhead	5 μs	5 μs
Total time of transfer to DSP	97 μs	54 μs

3.2.5.2 Data acquisition

The data acquisition for the PMD consists of standard components having six DDLs, two RORCs, one front-end digital crate (FEDC), and one local data concentrator (LDC). This will be adequate for building the PMD subevent. It will be further connected to the main data acquisition system of the ALICE experiment.

3.2.5.3 Data volume and time of transfer

The average occupancies of the preshower and the veto chambers in central Pb+Pb collisions are 20% and 10%, respectively. With this occupancy, the data volume generated and time of transfer are summarized in Table 3.2. The data will be available at the DSP 100 μs after the interaction. The data transfer beyond this point is asynchronous and should not affect the detector operation. Thus the maximum dead time of the detector will be 100 μs, which is adequate to match with the L2 timings.

The cluster boards for the PMD have been optimized so that an almost uniform volume of data is handled by each cluster board. We have selected a scheme in which there will be three DSPs per cluster board for the preshower plane and six DSPs per cluster board for the veto one. There will be six cluster boards in total and each board handles a maximum of 20 Kbytes of data for the central trigger. This can be transferred through the DDL link to data acquisition in 200 μs. This will require three buffers on the cluster boards.

The total data volume will be 63 Mbytes distributed almost evenly over six DDLs. This volume of data can be easily handled using one FEDC.

3.3 Calibration and monitoring

The knowledge of the gains of the PMD cells is very important for the clustering of hits and for estimating the transverse electromagnetic energy. Calibration of the PMD will be done both in test beam and during real data-taking.

The response of the detector to MIPs is a good reference for the gain of the cells. This has been discussed in detail in Chapter 2. When data have sufficient statistics, MIP peak and shape can be determined

to an accuracy of better than 5%.

3.3.1 Calibration at test beams

As the number of channels in the PMD are large, it is not practical to put every cell in the test beam. Instead, about 10% of the cells will be randomly selected in each supermodule and exposed to a hadron beam to study the response to MIPs. This will be done using a computer-controlled movable table as used in the PHOS calibration [7]. These cells will be treated as references while comparing them with other cells for the MIP responses deduced during on-line data-taking. This will require about two weeks of test beam time.

3.3.2 Calibration in ALICE environment

The method for the selection of hadrons in actual experimental events has been successfully used in the WA98 PMD [8]. In the present case, one can select hadrons with very small photon admixture (see Chapter 4). The response of the cells to such selected hadrons will provide the calibration on-line and will be checked with the values measured with test beams. Remaining cells can then be calibrated using on-line data and the values of the reference cells.

4 Detector Performance

The performance of the PMD in the ALICE environment has been studied extensively using event generators and the GEANT simulation package. Simulated data have been used to deduce the photon counting efficiency and purity of the photon sample. The results are described in Section 4.1. The ALICE experiment does not have any electromagnetic calorimeter of sizeable coverage, particularly in the forward region [1]. We have, therefore, investigated the possibility of estimating the transverse electromagnetic energy using the preshower PMD. This is described in Section 4.2. The capability of the PMD for pursuing the physics topics outlined in Chapter 1 is described in Section 4.3.

4.1 Photon counting

4.1.1 Event generators

To optimise the pseudorapidity coverage and granularity, we used events that were generated using VENUS [2] and parametrized multiplicity and kinematic distributions from HIJING [3] A charged-particle pseudorapidity density of 8000 in central Pb+Pb collisions at the centre-of-mass rapidity has been used.

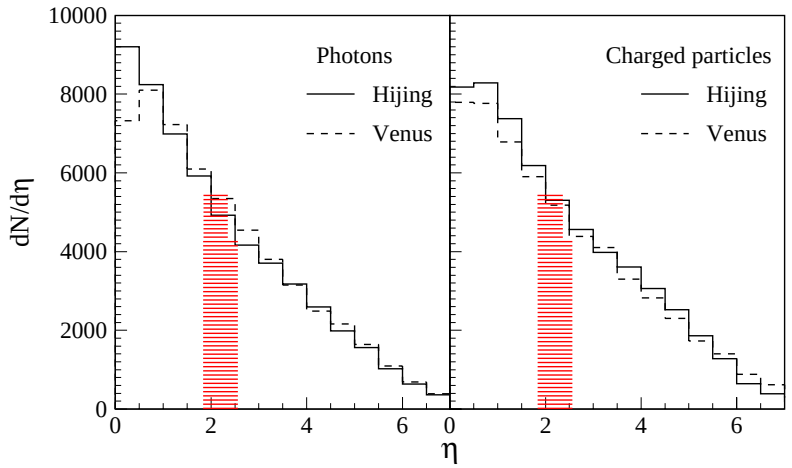

Figure 4.1: Pseudorapidity distribution of photons and charged particles in the two event generators.

The pseudorapidity distributions from the two generators are shown in Fig. 4.1. In the region of the PMD acceptance ($1.8 \leq \eta \leq 2.6$) the two distributions give comparable numbers for charged particles and photons. Using parametrized HIJING, the average number of photons and charged particles produced within this acceptance are found to be 4000 and 4250, respectively. The particle density of photons, 5.8 m from the interaction point is shown in Fig. 4.2. The large density of photons per cm^2 and the fact that the shower of the incident photons spreads to an average of four cells (see Chapter 2) constrains the geometrical parameters of the detector.

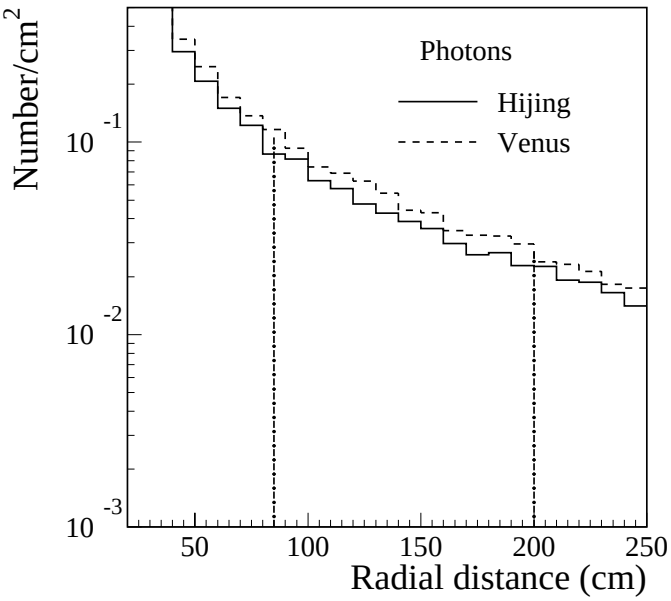

Figure 4.2: Photon-density distribution at the PMD location.

4.1.2 PMD within the AliRoot framework

AliRoot is the GEANT simulation framework of the detectors in the ALICE experiment. The geometry of the PMD has been implemented in AliRoot. A 5 mm thick steel support plate and 15 mm thick lead plate together form a converter of thickness 3 X_0. As discussed in Chapter 3, both the preshower and the veto parts of the PMD consist of honeycomb cells contained in gas-tight chambers called supermodules. Each supermodule is made of 72 $\times$ 72 hexagonal cells. Each cell consists of a gas volume of 8 mm thickness with inner circle of radius 5.1 mm. Implementation of the cell wall is achieved by positioning the gas hexagon inside a copper hexagon of 5.3 mm inner radius. The total wall thickness between two gas cells becomes 0.4 mm. The materials for the base plate and printed circuit boards in the supermodules have been included. The material budget in the supermodule layers as implemented in AliRoot is given in Fig. 4.3. Figure 4.4 shows a complete supermodule implemented in AliRoot.

These supermodules are placed inside an imaginary cylindrical volume at the position of the PMD. The entire detector consists of 26 supermodules in each plane. The plane of the veto detector is positioned in front of the converter and that of the preshower detector behind the converter.

Figure 4.5 shows the complete PMD set-up in AliRoot along with the vacuum chamber and a part of the ALICE baseline detectors. The central coordinate of each supermodule is adjusted such that the entire detector has full azimuthal coverage within the pseudorapidity range of interest. There exists a mirror symmetry about a plane defined by the beam and the vertical direction.

The ALICE vacuum chamber, described in Chapter 5, has an undulated section after the beryllium and aluminium sections. This has been specially provided to reduce the background to the PMD. All the components of the vacuum chamber, including flanges, bellows and undulated sections, have been implemented in AliRoot. Figure 4.6 shows an expanded view of a small section of the undulated chamber created through GEANT.

The correspondence between the coordinates of the cells in the veto and the preshower planes is made after digitization. The digitization of the GEANT output gives a unique coordinate for each cell.

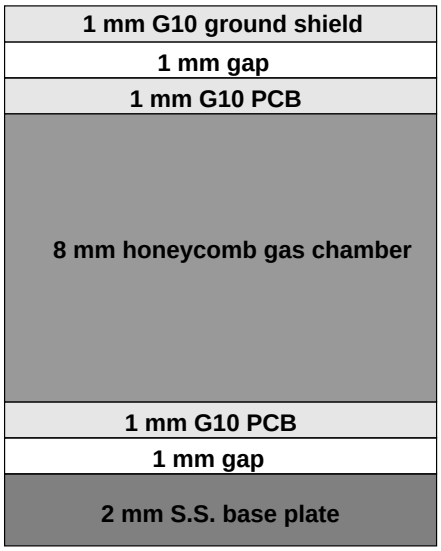

Figure 4.3: List of components in the supermodule as implemented in AliRoot.

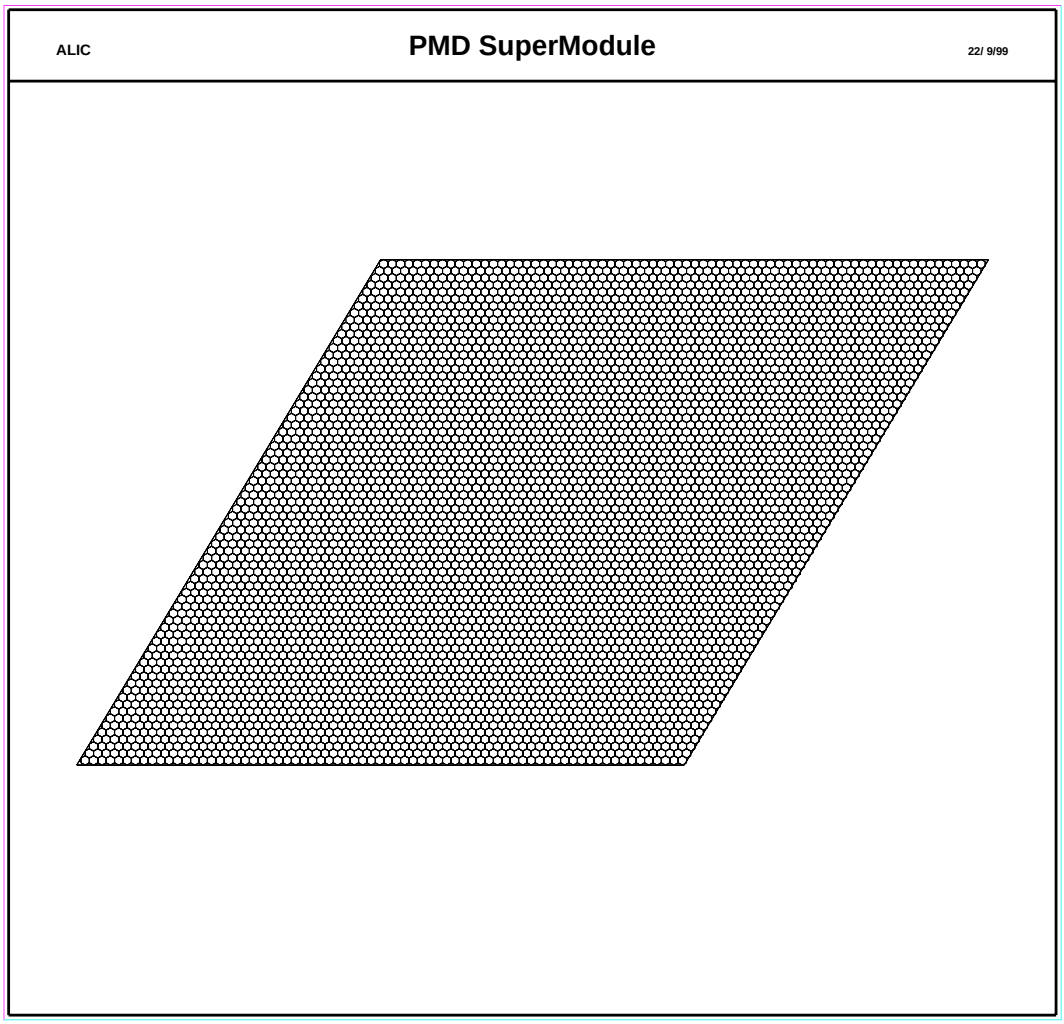

Figure 4.4: Implementation of a PMD supermodule in AliRoot.

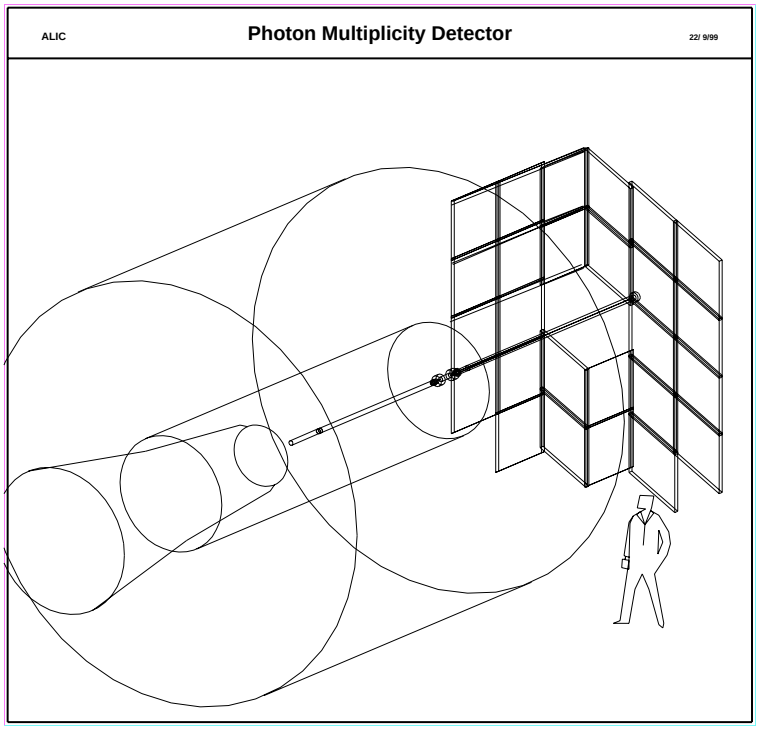

Figure 4.5: The ALICE set-up in AliRoot showing the PMD supermodules along with the vacuum chamber, part of the TPC and the dimuon spectrometer. The picture has been produced from an earlier version of the PMD geometry where supermodules in the central column were slightly moved to provide full azimuthal coverage up to $\eta = 2.8$.

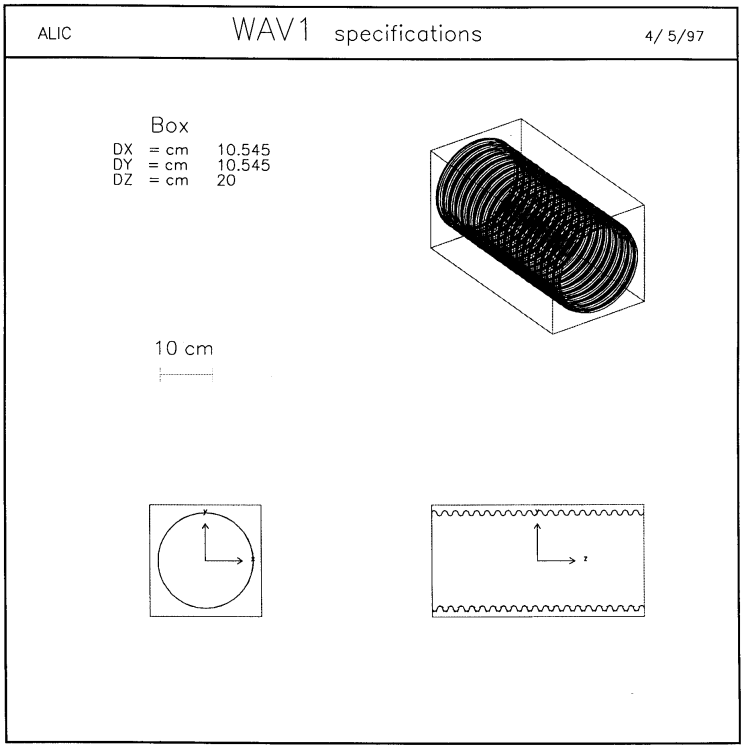

Figure 4.6: Implementation of the undulated vacuum chamber in AliRoot.

4.1.3 Reconstruction procedure

Reconstruction of photons in a preshower detector is achieved by folding the signals from neighbouring hits into a cluster and applying appropriate criteria to reject hadrons.

4.1.3.1 Clustering

The clustering procedure used currently is similar to that developed for the WA93/WA98 PMDs and is based on a nearest-neighbour algorithm. The algorithm has been modified to look at neighbouring cells in a honeycomb array. Corresponding changes in modelling the shower profile have also been incorporated.

In the first pass a search is made for local maxima. After the search for all the maxima in the entire detector, the energy depositions in cells, which are common to more than one local maximum, are redistributed by assuming a Gaussian energy deposition profile. The parameters of the profile are obtained from the test data for preshower energy deposition. Finer tuning of the parameters is made by adopting an iterative approach. Clustering of hits is performed separately for each supermodule. After rejection of hadrons, the cluster centroids yield the positions of photon hits.

4.1.3.2 Hadron rejection using neural network technique

In a preshower detector photons produce large signals after showering and non-interacting hadrons produce signals corresponding to those of minimum ionising particles (MIPs). A threshold on the cluster signal is able to reject most of the charged hadrons. Such a scheme of hadron rejection has been applied in the case of the PMD in the WA93 and the WA98 experiments [4, 5]. In this scheme, however, low-energy photons also get rejected as their signals fall within the threshold.

In the present case we have used a charged particle veto detector for hadron rejection for the following reasons.

- The average energies of photons are smaller in the region of pseudorapidity where the PMD can be implemented as compared to the case of fixed-target experiments. Rejection of hadrons using threshold on the cluster signal will lead to a loss of low-energy photons.

- A significant number of electrons are also produced in nuclear collisions at the LHC energy. In the preshower detector they will produce large photon-like signals. They are to be rejected.

- Interesting physics with low-p_{T} particles makes it necessary to use hadron rejection schemes which are more efficient in retaining low-energy photons.

We have used neural-network (NN) algorithms for photon–hadron discrimination using the veto and preshower signals. The method is described in detail in Ref. [6].

The technique consists of a standard feed-forward network using the following 17 inputs derived from the preshower and the veto hits of each observed cluster of photons and hadrons:
(i) signal strengths in seven cells in and around the cluster maximum of the preshower detector,
(ii) signal strengths in seven cells in the veto detector situated opposite the cluster maximum mentioned in (i),
(iii) total number of cells affected by the cluster in the preshower part,
(iv) total signal strength of the preshower cluster, and
(v) total signal in seven cells of the veto detector mentioned in (ii).

Both hidden layer and functional link approaches of training the network produce similar results.

A typical spectrum of NN output, showing the discrimination possibilities is shown in Fig. 4.7 for the case of PMD alone in AliRoot. By applying a suitable cut on the NN output one can reject a major part of the hadron contamination. The threshold on the NN output value is selected for maximizing the photon content and minimizing the contamination.

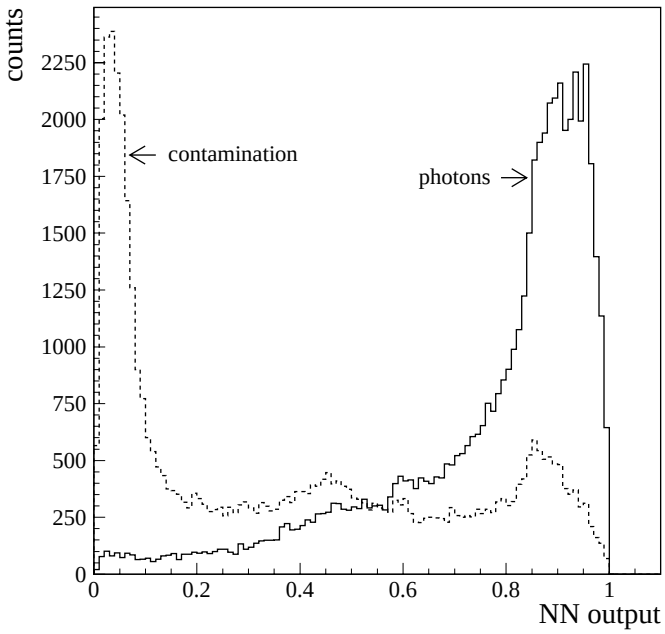

Figure 4.7: A typical neural-network spectrum showing discrimination between photons and hadrons. The solid line denotes photons and dashed line denotes hadrons.

4.1.4 Photon counting efficiency and purity

4.1.4.1 Definitions

The results are described using the following quantities.

$N^{\gamma}_{\rm inc}$: number of incident photons from the event generator.
$N^{\gamma,{\rm th}}_{\rm cls}$: number of photon clusters above the hadron rejection threshold.
$N_{\gamma-{\rm like}}$: total number of clusters above the hadron rejection threshold.

Clusters on the preshower plane are labelled as contaminants if

- they originate from an incident particle other than a photon;
- there is more than one cluster for a photon track, in which case only one cluster may be assigned to the incident track.

The photon counting efficiency, ε_γ and fractional purity of the photon sample, f_p are defined by the following relations [5] :

$$\varepsilon_\gamma = N^{\gamma,{\rm th}}_{\rm cls}/N^{\gamma}_{\rm inc}\ , \tag{4.1}$$

$$f_p = N^{\gamma,{\rm th}}_{\rm cls}/N_{\gamma-{\rm like}}\ . \tag{4.2}$$

$(1-f_p)$ is the fractional contamination in the $N_{\gamma-{\rm like}}$ sample.

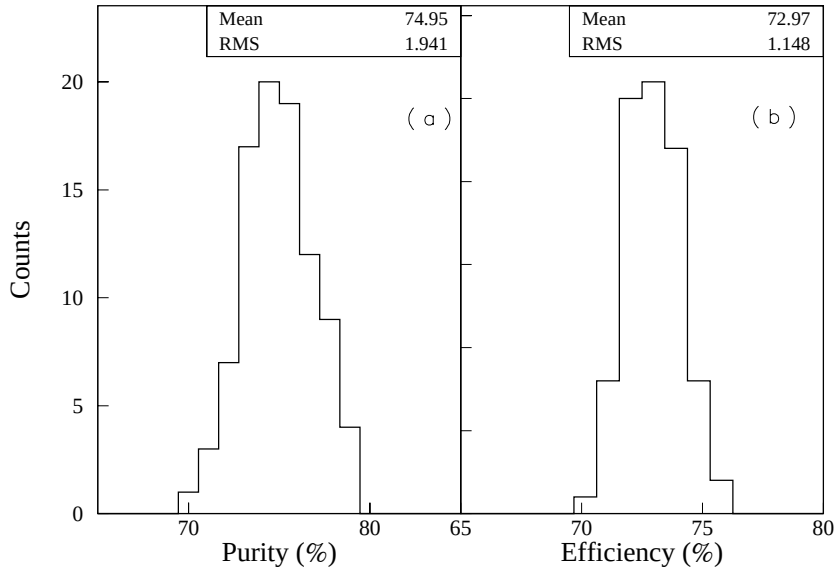

Figure 4.8: Purity and photon counting efficiency for the case of PMD alone in AliRoot.

4.1.4.2 Results

The event-by-event distribution of photon counting efficiency and purity for the case of PMD alone in AliRoot is shown in Fig. 4.8. The average values of the efficiency and purity are 73% and 75%, respectively. The distributions are quite narrow and have widths (σ) of $<$3%. This suggests that these quantities are well determined and have very little event-to-event fluctuation.

The photon counting efficiency and purity depend on several factors, e.g, the conversion probability, hadron rejection criteria applied, granularity and the track reconstruction efficiency. These in turn depend on centrality and pseudorapidity because of changing particle multiplicity and energy. These are described in the following paragraphs along with the effect of upstream material.

4.1.5 Effect of material

The particles produced in the interaction have to pass through some material before impinging on the detector. The ALICE vacuum chamber described in Chapter 5 is one of the important components of upstream material. The support structures of the barrel detectors (TPC, ITS) add more material. The effect of all upstream material is described in terms of changes in occupancy, deviation of incoming particles and finally the effect on the photon counting efficiency and purity.

4.1.5.1 Occupancy

The cell occupancies for both the preshower and the veto detector planes are plotted in Fig. 4.9 as a function of pseudorapidity. This demonstrates the effect of upstream material. Compared to the case of PMD alone, the occupancy in the preshower plane increases by at least 5% at all η in the presence of material. This happens due to extra particle tracks reaching the detector after interaction. The relative increase in occupancy in the veto plane is much more for the case of PMD with all the material as compared to the PMD alone.

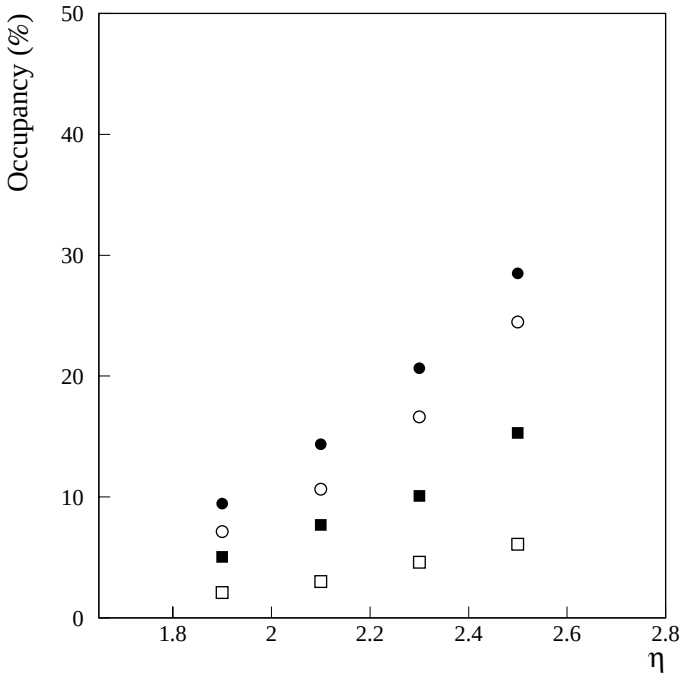

Figure 4.9: η-distribution of occupancy in the PMD: preshower plane PMD alone (open circle); veto plane for PMD alone (open square); preshower plane for PMD with all the material (filled circle); and veto plane for the PMD with all the material (filled square).

4.1.5.2 Contaminants arising due to large angle deflection

The most important effect of upstream material is to scatter particles so that they land on the detector after large deflection.

Distributions of $\delta\eta$ $(= \eta - \eta_{\rm orig})$ and $\delta\phi$ $(= \phi - \phi_{\rm orig})$ for the PMD alone and for the PMD in the presence of all the upstream material are shown in Fig. 4.10. The $\delta\phi$ distribution is symmetric but much wider for the case of PMD with all the material than for the case of PMD alone. A large number of photons appears on the PMD after scattering from the beam pipe, as seen on the negative $\delta\eta$ values. These large angle deflections worsen the capability of the PMD for the determination of spatial distribution of particles on an event-by-event basis.

We set a threshold for event-by-event fluctuation studies using the PMD at $\delta\eta = 0.1$ and $\delta\phi = 20^\circ$. The granularity of the FMD, which may be required for the study of isospin fluctuations, is also coarse [1]. Cosmic-ray observations by the JACEE Collaboration suggest pairing and clustering of tracks at scales $\delta\eta \sim 0.2$ and $\delta\phi \sim 30^\circ$ [7]. There have been theoretical suggestions [8] to look for fluctuations at similar scales. Hence the present constraint should not affect the capability of the PMD for event-by-event physics.

To account for the effect of large angle scattering, we include all clusters having $\delta\eta > 0.1$ or $\delta\phi > 20^\circ$ as contaminants, in addition to those included in Section 4.1.4.1. This condition further reduces the efficiency and purity of the photon sample.

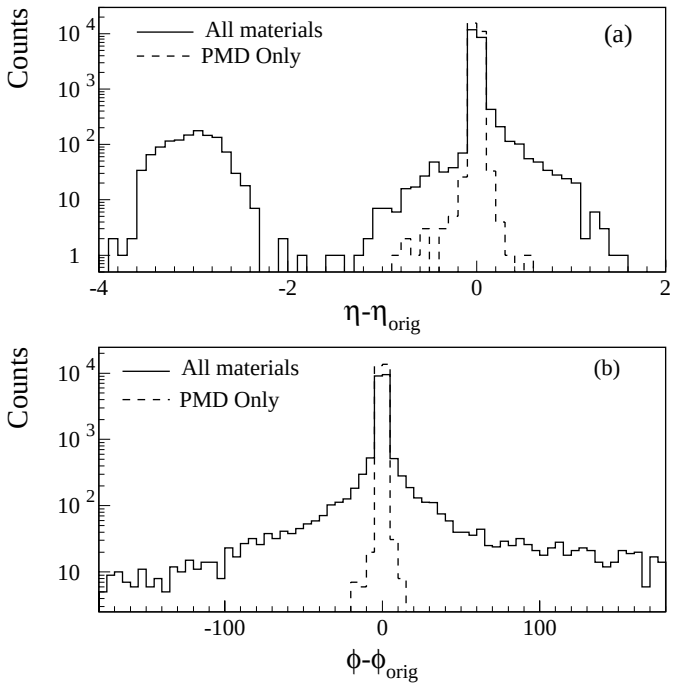

Figure 4.10: $\delta\eta$ and $\delta\phi$ distribution (the difference between the original η, ϕ of the track and the η, ϕ of the corresponding cluster position) for photons for (a) PMD alone and (b) PMD with all the material.

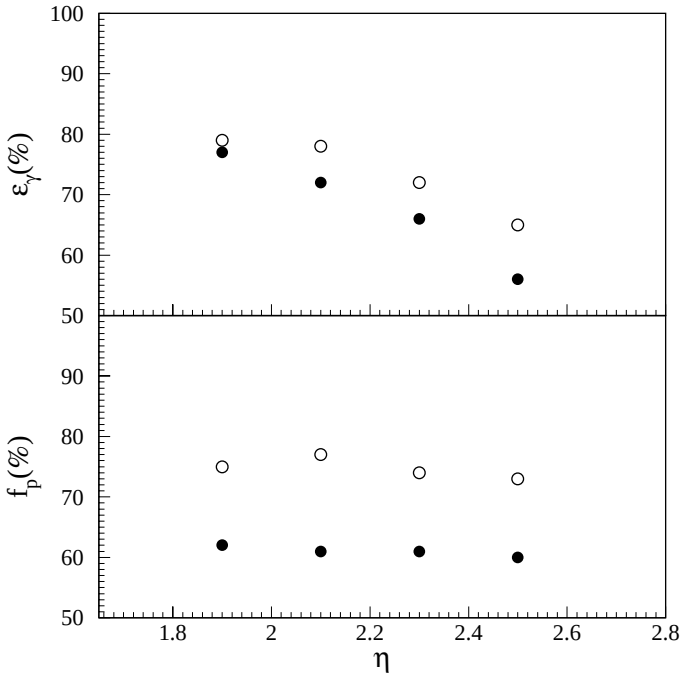

Figure 4.11: η-dependence of photon counting efficiency (top) and purity (bottom). Open symbols denote the case of PMD alone, and filled symbols are for the case of the PMD in the presence of all upstream material.

4.1.5.3 η-dependence

The pseudorapidity dependence of photon counting efficiency and purity is displayed in Fig. 4.11. For the PMD alone, the efficiency decreases at the highest η by about 15% compared to the maximum value. For the PMD with all material, the efficiency at the smallest η in the acceptance region is comparable to that of the PMD alone case. At the highest η this decreases by about 23% compared to the maximum value. The purity value is almost independent of η in both cases. However, in the presence of material, the purity decreases by about 15% uniformly over the entire region.

4.1.5.4 Other sources of background

Background from the ALICE environment, like the magnet wall and the outside concrete shields, is negligible. Neutron background is not a problem because of the insensitivity of the chamber gas to neutrons.

4.1.5.5 Comparison of results

Average values of the photon counting efficiency and purity are summarized in Table 4.1 for various cases. For comparison, the values for the WA98 PMD are also included [5]. It is observed that a 3 MIP threshold on the cluster signal considerably reduces the photon counting efficiency. The NN method gives higher efficiency although purity values are comparable. Improvement in NN techniques will be pursued to obtain better results. Even in the high particle density environment and in the presence of upstream material of the ALICE experiment, the efficiency and purity values are comparable to those obtained for the WA98 PMD.

Table 4.1: Photon counting efficiency and purity for different configurations of upstream material and different criteria for hadron rejection.

Case	Method	ε_γ (%)	f_p (%)
PMD alone	NN	73	75
PMD + all materials	NN	68	61
PMD alone	3 MIPs	46	76
PMD + all materials	3 MIPs	47	61
WA98 PMD	3 MIPs	68	65

4.1.6 Acceptance

4.1.6.1 $(\eta - \phi)$ acceptance

The PMD has full azimuthal coverage in the pseudorapidity range $1.8 \leq \eta \leq 2.6$ as seen from Fig. 1.1. The pseudorapidity coverage has been reduced by 0.2 units compared with the earlier value [9] because of reduced photon counting efficiency in the highest η-region.

4.1.6.2 Two-track separation

Figure 4.12 displays the distribution of distance (δr) between neighbouring pairs of clusters. The most probable value of two-track separation is found to be ~ 3 cm.

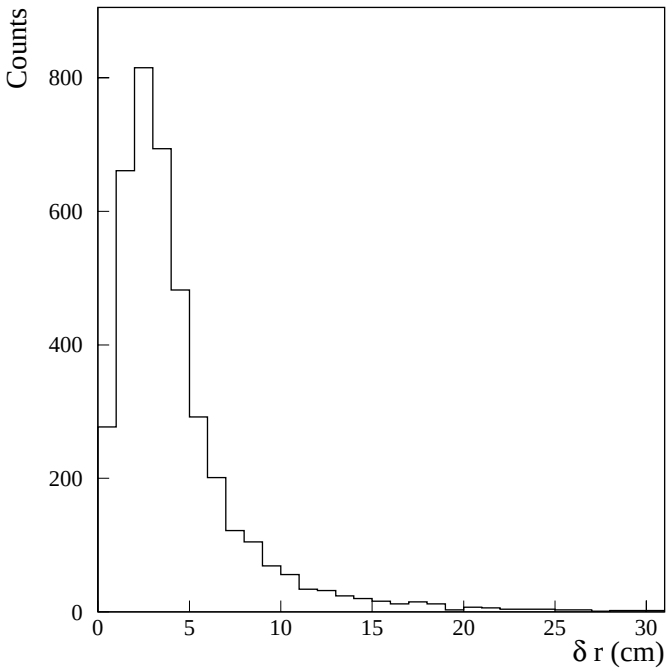

Figure 4.12: Separation (δr) between two clusters on the PMD.

4.1.6.3 p_{T} acceptance

The p_{T} acceptance of the PMD for photons is shown in Fig. 4.13. The upper curve represents the fraction of photon clusters remaining after applying NN threshold for hadron discrimination and the lower curve represents the same quantity obtained after applying a 3 MIP threshold on the cluster signal for hadron rejection [10]. It is seen that the PMD is capable of detecting very low-p_{T} particles, up to 25 MeV/c. The NN method of hadron discrimination retains a much larger fraction of low-p_{T} particles. For $p_{\mathrm{T}} <$ 150 MeV/c, this is about 25% higher than with the application of the 3 MIP threshold on the cluster signal.

4.1.6.4 Dead area

The thickness of the honeycomb cell walls corresponds to a dead area of $\sim$ 7% for normal incidence of charged particles. When particles are incident at larger angles the contribution of the cell wall to the dead area is considerably reduced. The walls of the supermodules contribute only $\sim$ 2.5% to the dead area. In the preshower part there are a large number of shower particles travelling at different angles and several cells are affected. Hence there is no dead area within a preshower supermodule.

4.1.7 MIP sample from the preshower hits

The data on Pb+Pb collisions will be used for online checking of the relative gains of the cells within the detector [5]. Whereas there is no problem in identifying good MIP hits in the veto chambers, one needs to have a good algorithm to select MIP hits in a given event for the preshower part. Based on the results of test beam data and neural-network analysis we have developed an algorithm to select MIP candidates. It is estimated that the selected MIP sample will have less than 5% photon contamination.

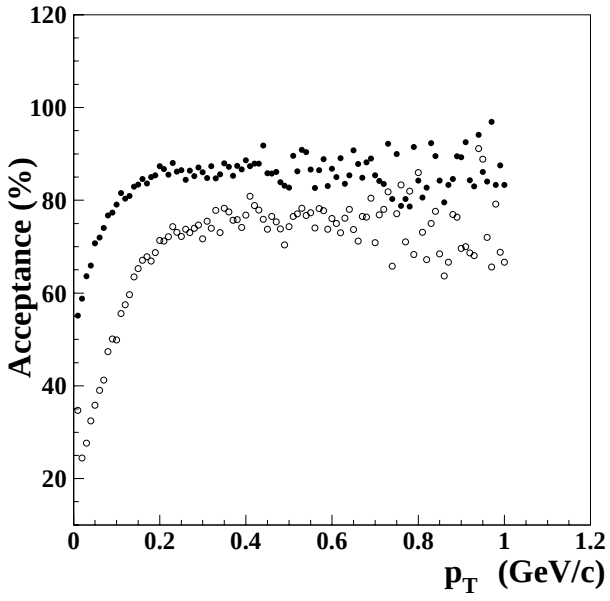

Figure 4.13: p_{T} acceptance of the PMD: Open circles represent hadron rejection by threshold on the cluster signal without the charged particle veto and filled circles denote the neural-network method using the veto.

4.2 Transverse electromagnetic energy

4.2.1 Introduction

Calorimetry in the ALICE experiment is restricted to a small-acceptance photon spectrometer [11] in the barrel region and the zero-degree calorimeters in the extreme forward regions [12]. The proposed CASTOR detector will cover only the region $\eta > 5.5$ [13]. In this section we investigate the possibility of using the preshower signal for estimating the transverse electromagnetic energy. The acceptance of the PMD was $1.8 \leq \eta \leq 2.8$ for the results presented here. The present acceptance, as described in Section 4.1.6.1 is 0.2 units smaller. This is not expected to affect the results qualitatively.

The PMD can be used to provide an estimate of the transverse electromagnetic energy $E_{\mathrm{T}}^{\mathrm{em}}$ using the measured preshower signals. Although there are large fluctuations in the energy deposited by individual photons in a preshower detector, the fluctuation reduces substantially when the energy depositions of a large number of photons are added.

The effect of summation is shown in Fig. 4.14 where the simulation results of 100,000 single photons are presented for two different energies. The top frame shows the spectra of energy depositions due to individual photons. The middle frame shows the results after averaging over 100 particles. The bottom frame shows the average taken for 1000 particles. It can be seen that while in the top frame the distinction between the energy depositions for 1 GeV and 2 GeV photons can hardly be seen, the summation procedure greatly reduces the fluctuation. It is also found that the width of the distribution becomes smaller when the summation contains a larger number of particles.

4.2.2 Estimation of $E_{\mathrm{T}}^{\mathrm{em}}$

The above observation has been used to estimate the transverse electromagnetic energy $E_{\mathrm{T}}^{\mathrm{em}}$ on an event-by-event basis using the photon signals in a preshower detector. Within the acceptance of the PMD, the $E_{\mathrm{T}}^{\mathrm{em}}$ can be approximated by the relation [4]

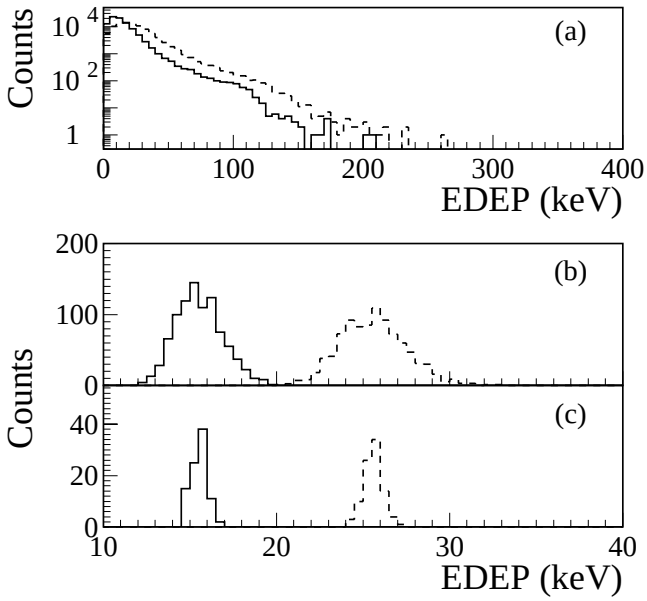

Figure 4.14: Histogram of energy deposition in PMD for (a) 100,000 photons of 1 GeV (solid lines) and 2 GeV (dashed lines), (b) the average value of 100 photons, and (c) the average value of 1000 photons.

$$\hat{E}_{\mathrm{T}} = \sum_i \Delta E_i . \sin\theta_i \ , \tag{4.3}$$

where θ_i is the angle at which the i^{th} γ-like cluster appears, ΔE_i is the energy deposited in the sensitive volume of the PMD corresponding to the i^{th} cluster, and the sum runs over all the observed γ-like clusters. We denote $E_{\mathrm{T}}^{\mathrm{em}}$ measured by the PMD as $\hat{E}_{\mathrm{T}}$ to distinguish it from the calorimetric measurement of $E_{\mathrm{T}}^{\mathrm{em}}$.

Figure 4.15 shows the event-to-event fluctuation in $\hat{E}_{\mathrm{T}}$ values along with that of $N_{\gamma-\mathrm{like}}$ for a given set of central VENUS events. The width of the $\hat{E}_{\mathrm{T}}$ distribution is found to be slightly larger than that of the $N_{\gamma-\mathrm{like}}$ distribution because of fluctuations in the process of energy deposition. Considering the contribution of fluctuation in the input multiplicity, the event-to-event fluctuation in $\hat{E}_{\mathrm{T}}$ for a fixed multiplicity is estimated to be 3%.

4.2.3 Sensitivity to changes in $E_{\mathrm{T}}^{\mathrm{em}}$

The estimated $\hat{E}_{\mathrm{T}}$ value is expected to be sensitive to changes in the transverse energy in the event. To study the sensitivity of the preshower signal to variations in the $E_{\mathrm{T}}^{\mathrm{em}}$ in the event, we have modified a set of central Pb+Pb events obtained from the VENUS event generator [2]. The momenta of all the particles are multiplied by an arbitrary factor so that the transverse energy in the events is increased by the corresponding factor. As the multiplicity of the group of events remains unaltered, the effect of this modification on the preshower signal should provide a measure of the sensitivity independent of multiplicity. Results of earlier investigations can be found in Ref. [14].

The results obtained are shown in Fig. 4.16 for several factors varying from 0.5 to 1.25. The scatter plot also displays the correlation between the $\hat{E}_{\mathrm{T}}$ and the $E_{\mathrm{T}}^{\mathrm{em}}$ for each set of events. The straight line

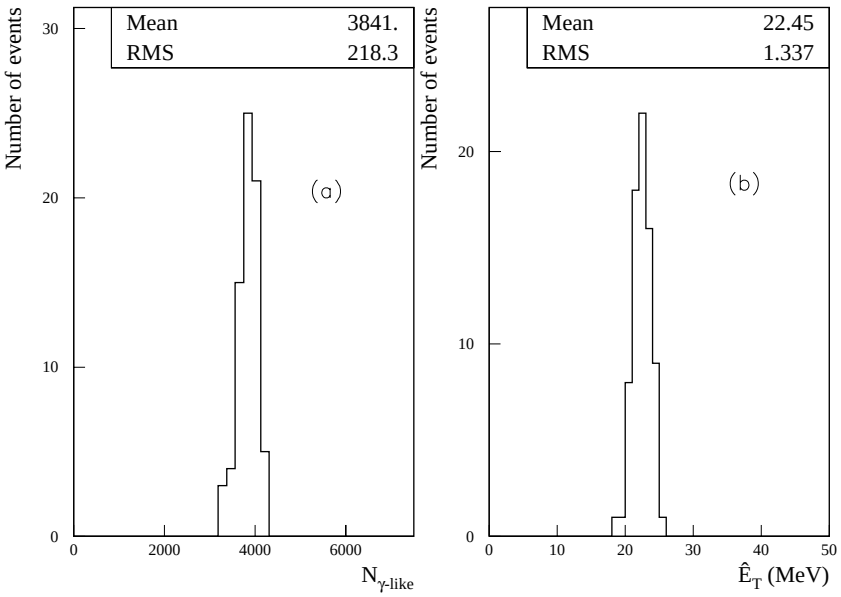

Figure 4.15: Histrogram showing $N_{\gamma-\text{like}}$ and $\hat{E}_{\text{T}}$ for a set of central VENUS events.

drawn through one set indicates correlation for the minimum-bias case. For each group of events the slope of the minimum-bias line is different.

Figure 4.17 shows the mean values of the $\hat{E}_{\text{T}}$ for the four groups of events. The values are normalized to unity for the normal VENUS events (factor = 1.0). Values obtained from an earlier simulation [14] for momentum factors 1.5 and 2.0 are also shown in the figure. There is a linear relation between the fractional increase in $\hat{E}_{\text{T}}$ and corresponding increase in E_{T}^{em} of the event in the entire range investigated. We deduce that

$$\Delta E_{\text{T}}^{\text{em}} \cong 2\Delta\hat{E}_{\text{T}} \; . \tag{4.4}$$

The linearity of response over such a wide range suggests that it may be possible to use the preshower detector as a calorimeter. The event-to-event fluctuation in $\hat{E}_{\text{T}}$ values of $\sim 3\%$ leads to about 6% fluctuation in the E_{T}^{em} value estimated using the preshower detector. Considering that there is only one plane of a preshower detector, this result suggests that relative changes in E_{T}^{em} can be determined well.

4.2.4 Hadronic contamination

The hadronic contamination in the estimated $\hat{E}_{\text{T}}$ values using γ-like clusters is found to be 22% and 38%, respectively, for the PMD alone and for the PMD with all the upstream material. This is of the same order as the hadronic contamination in γ-like clusters in the two cases.

4.2.5 η-distribution of $\hat{E}_{\text{T}}$

The pseudorapidity distribution of $\hat{E}_{\text{T}}$ can also be obtained in a manner similar to the integral quantity by summing over particles in a given $\eta-$bin. However as the number of particles decreases, the fluctuation of $\hat{E}_{\text{T}}$ values increases. The widths for event-by-event fluctuation in η-bins of size 0.1 units are found to be $\sim 10\%$, including the contribution of fluctuation in input multiplicity [15]. This fluctuation may be adequate to distinguish the effects for a certain range of exotic events where the transverse electromagnetic energy may change by more than 20% within small pseudorapidity bins.

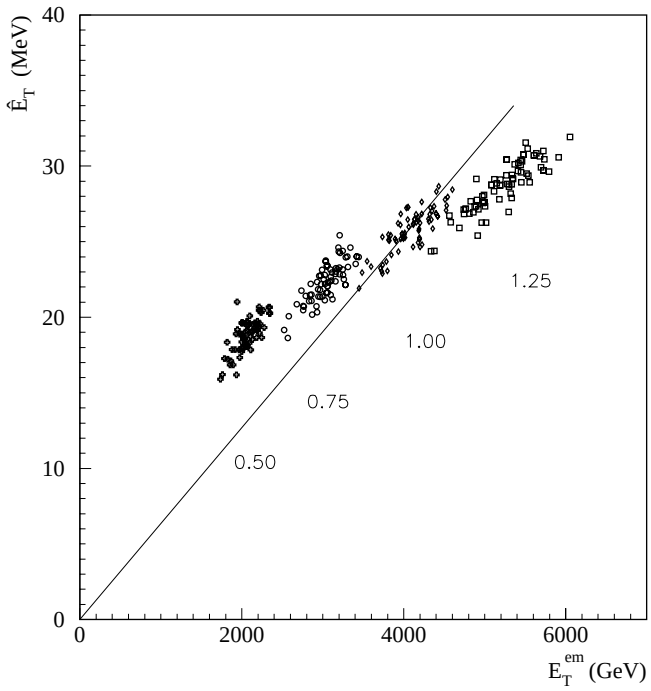

Figure 4.16: Scatter plot of $\hat{E}_T$ vs. E_T^{em} for a group of central VENUS events. The momenta of each particle in the events have been modified by a suitable factor as indicated on the figure.

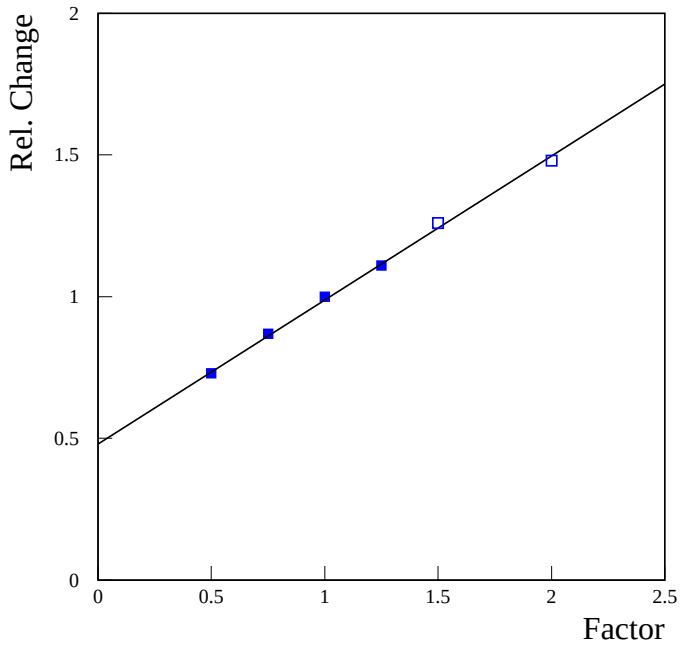

Figure 4.17: Mean values of the $\hat{E}_T$ distributions for the four sets corresponding to different momentum factors in VENUS. These are normalized to unity for the normal VENUS events. Open symbols are the values taken from Ref. [14].

4.3 Physics performance

The results presented in this section have been obtained using fast simulations in addition to using the event generators and the GEANT package. Physics performance has been studied in several cases by assuming that the coverage of the PMD extends to the pseudorapidity range $1.8 \leq \eta \leq 2.8$ as given in an earlier document [9]. The pseudorapidity acceptance is now 0.2 units lower as explained in Section 4.1.6.1. Physics results presented here are not expected to be qualitatively affected by this slight reduction in acceptance.

4.3.1 Azimuthal anisotropy and flow

4.3.1.1 Introduction

Photon multiplicity measurements using a preshower PMD have already been used to study collective flow at the SPS energies [16, 17] using the Fourier expansion technique. Here we explore the possibility of studying azimuthal anisotropy using the PMD in ALICE. The photons measured in the PMD originate predominantly from π^0 decay. The decay introduces non-flow correlations due to four-momentum conservation. The decay has another effect also: it dilutes the correlation in azimuthal angles. Using the measured value of anisotropy in the photon data, we also try to estimate the amount of anisotropy in neutral pions. The results are compared with those for charged particles. Using a fast simulation we systematically study the effect of multiplicity, amount of initial flow, detector imperfections and upstream material. The results are described for first- and second-order flow. We also evaluate the possibility of estimating the event plane. A knowledge of the event plane will enable a study of correlated particle production, as measured in other ALICE detectors, with respect to the event-plane direction.

4.3.1.2 Methodology

Events have been generated using parametrizations as described in Ref. [18] for a set of multiplicities in the range 200–4000. The wide range of multiplicities serves to determine the effect of fluctuations due to a finite number of particles in varying centrality conditions in the collisions.

The azimuthal angles are generated according to the probability distribution

$$r(\phi) = \frac{1}{2\pi}\left[1 + 2v_1\cos(\phi - \psi_1) + 2v_2\cos 2(\phi - \psi_2)\right] , \tag{4.5}$$

where ψ_m is chosen randomly. Within the present theoretical understanding, the first-order event plane ψ_1 coincides with the reaction plane ψ_R. v_1 and v_2 denote the first- and second-order flow components corresponding to directed and elliptic flow respectively. v_1 measures the shift of the centroid of the azimuthal distributions and v_2 is a measure of the difference between the major and minor axes of the elliptic event shape. Because of finite particle multiplicity, the estimated event plane $\psi_m^{\rm est}$ does not coincide with the actual plane, as defined by ψ_m.

The simulation results are described for (a) directed flow, (b) elliptic flow and (c) both directed and elliptic flow. In the last case the major axis of the ellipse is assumed to be in the direction of the first-order event plane. This corresponds to in-plane flow, i.e. $\psi_2 = \psi_1$.

The present analysis is based on 2000 events in each case. The generated data have been analysed to obtain the following:

- $v_1^{\rm est}$, the multiplicity weighted average of $v_1^{\rm event}$ for each data sample.
- $\psi_1^{\rm est}$, the estimated event plane for first-order Fourier coefficient, also estimates the direction of ψ_R. Because of finite particle multiplicity the estimated event plane $\psi_m^{\rm est}$ in the generated data fluctuates about the actual event plane ψ_m, with a spread determined by the amount of initial flow and the multiplicity. The event-plane resolution correction factor (RCF) estimates the deviation of the estimated plane from the actual plane, and is calculated as per the prescription of Ref. [19].

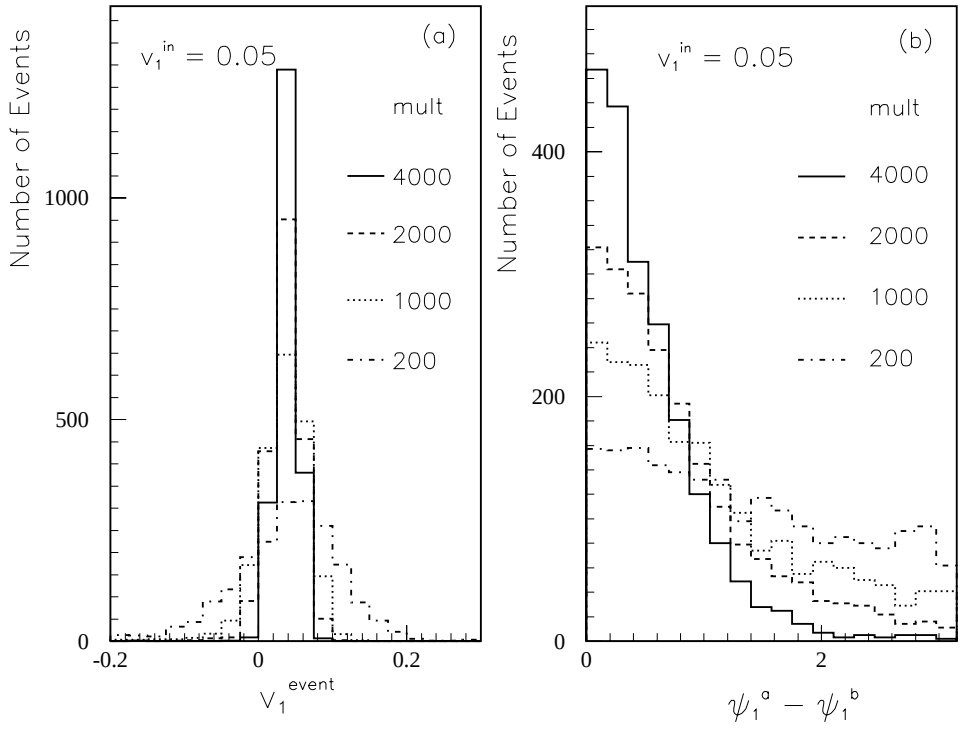

Figure 4.18: (a) v_1^{event} distribution for various multiplicities of photons. (b) Distribution of the angle $\psi_1^a - \psi_1^b$ between the randomly chosen subevents for first order. Angles ψ_1^a and ψ_1^b are expressed in radians.

- v_2^{est}, the magnitude of the second coefficient, estimated using the event plane determined for the first order and for the second order. The coefficients v_m are better determined by using the event plane (ψ_m) of the same harmonic [19]. When v_2 is determined with respect to the first-order event plane, the sign of v_2 determines whether the flow is in-plane or out-of-plane, and the magnitude of v_2 with respect to the second-order event plane is a measure of the ellipticity of the event shape. In the present work we determine this measure.

- ψ_2^{est}, the second-order event plane estimates the direction of the major axis of the ellipse.

The calculated values of v_m^{est} are corrected for by the resolution factor for the event-plane determination.

4.3.1.3 Directed flow

Effect of multiplicity on v_1^{est}

The distribution of v_1^{event} for a set of events of varying multiplicities of photons are shown in Fig. 4.18(a). The distribution becomes narrower with increasing multiplicity, showing the expected decrease in the errors on the estimated values of flow. The distribution of the angle between the subevents ($\psi_1^a - \psi_1^b$) becomes flatter with decreasing multiplicity as seen in Fig. 4.18(b).

Figure 4.19 shows the values of the estimated flow and the RCFs, both for charged particles and photons for an input anisotropy of 0.05. The v_1^{est} values include the actual contribution of flow of π^0, and the effect due to decay. The resolution of the event-plane determination improves with multiplicity and

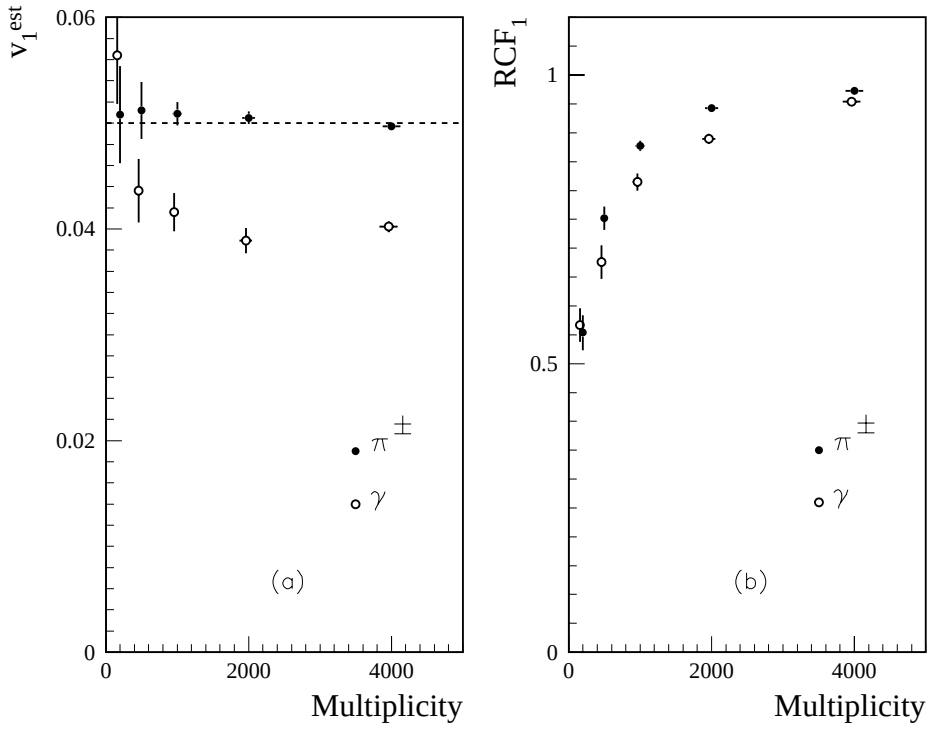

Figure 4.19: (a) Estimated values of v_1 as a function of multiplicity for a value of input anisotropy v_1 = 0.05 (b) Resolution correction factor as a function of multiplicity. The error bars are statistical.

moves closer to unity. However, the RCF values deduced from photons are smaller than those deduced from charged particles.

At low multiplicities the v_1^{est} values for photons are found to be larger than even the input value. This arises due to the correlation among the kinematic variables of decay products due to energy and momentum conservation. The contribution to anisotropy due to momentum conservation correlation decreases with increasing multiplicity, since the effect due to correlations varies as $1/N$ [19].

Amount of initial flow present in the sample

The sensitivity of the PMD for detecting a small amount of directed flow is demonstrated in Table 4.2. It is found that the effect observed with photons is generally a little lower compared to that of charged particles, and persists even at values of v_1^{in} = 0.025.

To estimate the background due to decay on the observed values of v_1 we generated an azimuthally symmetric distribution ($v_1^{in} = 0$) and calculated values of v_1 for different multiplicities. These are also presented in Table 4.2. Removing the effect of auto correlations in a symmetric distribution results in negative values of v_1. There is a small contribution to v_2 for low values of multiplicity due to the momentum conservation correlation. It may not be possible to discern the values of v_1 below 0.02 for a photon multiplicity of 500 or below. For larger multiplicities the threshold for detection decreases.

Table 4.2: Estimated directed flow (v_1^{est}) and event-plane RCF for various multiplicities, and for different initial anisotropies.

		$\pi^{\pm}$		γ	
Mult.	v_1^{in}	v_1^{est}	RCF	v_1^{est}	RCF
500	0.0	–0.007	–	0.0162	0.411
2000	0.0	–0.005	–	0.0124	0.368
2000	0.01	0.007	0.345	0.0129	0.457
2000	0.025	0.024	0.734	0.023	0.685
2000	0.100	0.099	1.000	0.080	0.976

4.3.1.4 Elliptic flow

The simulation has also been performed for investigating the sensitivity of the PMD for studying elliptic event shapes. The observed v_2^{est} and the RCF values have been estimated for various input v_2^{in} values and multiplicities [18]. In the case of elliptic flow, the RCF represents the correction factor for determining the direction of the major axis of ellipse.

It was found that the values of v_2^{est} obtained using photons are lower than the initial anisotropy in pions, the reason being dilution of flow due to decay of π^0. It was also seen that the decay dilutes the elliptic flow more than it dilutes the directed flow. At low multiplicities, the observed dilution due to decay is partially offset by the correlation due to energy momentum conservation, which is known to contribute to the observed flow of all orders.

Table 4.3: Comparison of elliptic flow observable using $\pi^{\pm}$ and γ for different initial anisotropies

		$\pi^{\pm}$		γ	
Mult.	v_2^{in}	v_2^{est}	RCF	v_2^{est}	RCF
500	0.0	–0.002	–	0.015	0.181
2000	0.0	–0.004	–	0.003	0.219
2000	0.025	0.025	0.765	0.018	0.588
2000	0.05	0.050	0.942	0.032	0.833
2000	0.10	0.10	0.982	0.062	0.960

Table 4.3 shows the estimated values for varying input flow, and the values of the background due to finite multiplicity (v_2^{in} = 0). For multiplicities lower than 500, anisotropy values of 0.025 may not be observable using the PMD. The RCF for an azimuthally symmetric distribution for charged particles cannot be determined because the event plane cannot be determined in this case.

4.3.1.5 Inclusion of both directed and elliptic flow

The analysis was also repeated for data that include both the directed and the elliptic flow. The data were generated such that for every event, the major axis of the ellipse is aligned along the reaction plane (the first-order event plane). The higher-order anisotropy is obtained using the event plane of the lower order. However, better accuracy is obtained if the event plane of the same order is used. The results confirm the naive expectation that the estimated anisotropy of order *m* is unaffected by initial anisotropy of any order other than *m*.

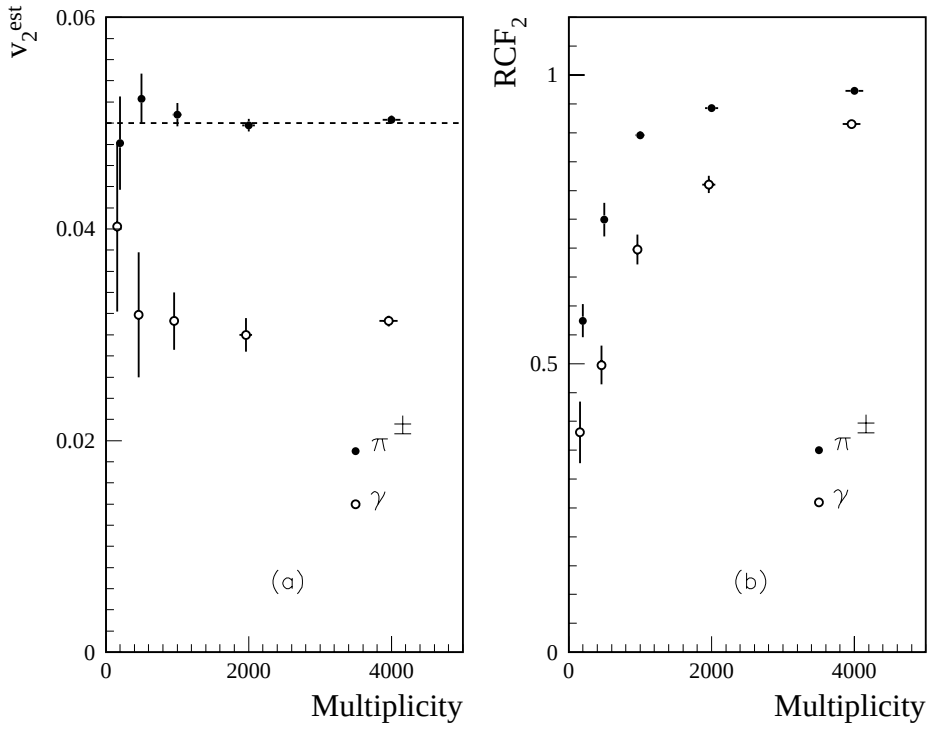

Figure 4.20: (a) Estimated values of v_2^{est} as a function of multiplicity, and (b) Resolution correction factor for the determination of the orientation of the ellipse. The generated data corresponds to $v_2 = 0.05$. The error bars are statistical.

The results remain the same as long as the major axis of the ellipse is along or perpendicular to the direction of the event plane. The estimated RCF is a quantitative measure of how well the event plane can be determined. Figure 4.20(a) shows v_2^{est} for different multiplicities. The initial anisotropy in the generated data is $v_1 = 0.05$ and $v_2 = 0.05$. One observes that the v_2^{est} for the photons is lower than that for charged particles except at low multiplicities. A measurable flow signal survives in photons. Figure 4.20(b) shows the estimated RCF for different multiplicities, both for $\pi^{\pm}$ and photons. The increased indeterminacy in the orientation of the ellipse for photons is again due to the effect of decay.

4.3.1.6 Effect of upstream materials and dead area on the detector

In the actual environment of the ALICE experiment, particles reaching the PMD may suffer scattering in the upstream materials. In addition, a part of the detector may be dead for various reasons, and may have to be excluded from the analysis.

To investigate the effect of the upstream material, we have assumed that every incoming particle is scattered so that its η and ϕ change by $\delta\eta$ and $\delta\phi$, respectively. We further assume Gaussian distributions for $\delta\eta$ and $\delta\phi$ with widths 0.1 units and 10 degrees, respectively. The particles now incident within the PMD acceptance are reanalysed to look for anisotropic behaviour.

During data-taking a supermodule could go dead. In such a case, analysis of the data for flow requires a detector correction by one of the methods in Ref. [19] to estimate the reaction plane and subsequently the anisotropic parameters.

We present the results in terms of the accuracy of the reaction plane determined from the PMD, since the actual reaction plane in generated data is known. The reaction plane is estimated once using the

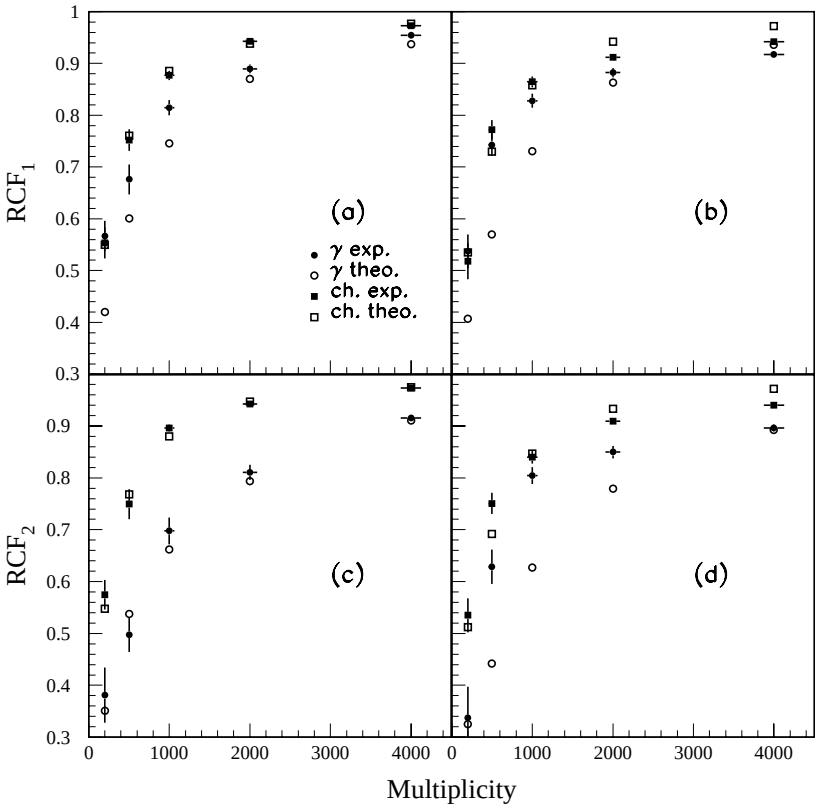

Figure 4.21: Resolution correction factor for various cases and different multiplicities for charged particles and photons : (a) directed flow, ideal case, (b) directed flow, imperfect detector, (c) elliptic flow, ideal case, (d) elliptic flow, imperfect detector.

charged particles and next using the photons in the following assumed situations:

(a) Ideal case: the kinematic quantities of the particles do not change before falling on the detector and the detector has 2π coverage.

(b) Imperfect detector: incident particles are scattered and a part of the detector is dead.

In both cases we determine also the RCF by dividing the event randomly into two subevents and measuring the correlation between them. This method is useful for determining the $\mathrm{RCF_{ex}}$ in experimental data. This $\mathrm{RCF_{ex}}$ estimates the deviation of the estimated plane ψ_m^{est} from the actual plane ψ_m. In the generated data, we know the precise amount by which the estimated reaction plane deviates from the actual plane, and can obtain $\mathrm{RCF_{th}}$ ($\equiv \langle\cos(\psi_m - \psi_m^{\mathrm{est}})\rangle$). We have determined both $\mathrm{RCF_{ex}}$ and $\mathrm{RCF_{th}}$ for the various samples of charged particles and photons for varying multiplicities.

Figure 4.21 shows the $\mathrm{RCF_{ex}}$ and $\mathrm{RCF_{th}}$ for both charged particles and photons for an ideal detector and an imperfect detector. For the imperfect detector the calculations were made after correcting for the ϕ asymmetry. The upper two figures show the results for directed flow, and the lower ones show the results for elliptic flow. One observes that in all cases, the effect on photons is more than that on the charged particles. One further observes that the difference between the $\mathrm{RCF_{ex}}$ and $\mathrm{RCF_{th}}$ decreases with increasing multiplicity of the particles. For the multiplicities likely to be achieved in the central and semi-central events in ALICE, the plane determined using photons appears to be as good as the one obtained using charged particles.

In all the above cases, the quantitative effect of scattering and dead channels on the anisotropy pa-

rameters is marginal. Scattering systematically causes the observed flow to be diluted. The ϕ asymmetry in the detector and the subsequent detector correction effect systematically increase the errors on the estimated values of the anisotropy parameters. This increase in error is caused by occasional over-correction (or under-correction) of the azimuthal angles of an event. For the sample of generated data with a multiplicity of 2000 and v_m = 0.05, the estimated values of anisotropy are listed in Table 4.4. The exercise was repeated for the determination of the major axis of the ellipse. The quantitative effect on v_2 is more than on v_1. The initial signal of flow still persists unambiguously.

A slight increase in the estimated values of v_m for lower efficiency and purity arises due to an increased content of charged particles. If in practice a part of the contaminants do not have the memory of initial anisotropy, the resulting observed signal will be further reduced.

Table 4.4: Effect of upstream materials and dead channels on v_1^{est} and v_2^{est} for different efficiencies and purities.

Input	Efficiency	Purity	PMD in air	PMD with upstream material and dead channels
v_1^{in} = 0.05	100	100	0.0406 $\pm$ 0.0006	0.0394 $\pm$ 0.0009
	80	80	0.0424 $\pm$ 0.0006	0.0407 $\pm$ 0.0008
	60	60	0.0443 $\pm$ 0.0005	0.0433 $\pm$ 0.0008
v_2^{in} = 0.05	100	100	0.0315 $\pm$ 0.0007	0.0304 $\pm$ 0.0009
	80	80	0.0355 $\pm$ 0.0006	0.0332 $\pm$ 0.0009
	60	60	0.0385 $\pm$ 0.0005	0.0364 $\pm$ 0.0008

4.3.1.7 Effect of decay

The quantitative effect of decay is seen to depend on both the values of multiplicity and the amount of initial flow. The fractional change in the observed anisotropy from the actual anisotropy is seen to scale with another measure of anisotropy χ. This quantity is determined experimentally from the distribution of angle between the subevents [19] :

$$e^{-\chi^2/4} = 2N_{>}/N_{\rm tot} \ , \tag{4.6}$$

where $N_{>}$ is the number of events which have an angle between subevents greater than $\pi/2m$ and $N_{\rm tot}$ is the total number of events.

Figure 4.22(a) shows the fractional change in the observed value of v_1 for photons as a function of χ for varying values of input flow and multiplicity. From the experimentally determined quantity χ and the estimated v_1 from the Fourier analysis, it is possible to determine the actual value of anisotropy present in the parent pions [20]. However, as can be seen from the local slope of the curve at different χ values, the error estimated on the v_m values for pions will be small for values of χ greater than about 1.5. In the ALICE environment, it should be possible to determine the actual anisotropy to an accuracy better than about 10%.

The fractional change in observed values of v_2 is also seen to scale with χ, as in the case of directed flow, enabling the determination of elliptic flow at the pion level. The distribution is shown in Fig. 4.22(b). For flow of both orders, it is further observed that the effect of the scattering and dead area is to broaden the distribution, causing a slight increase in the errors on the estimated values.

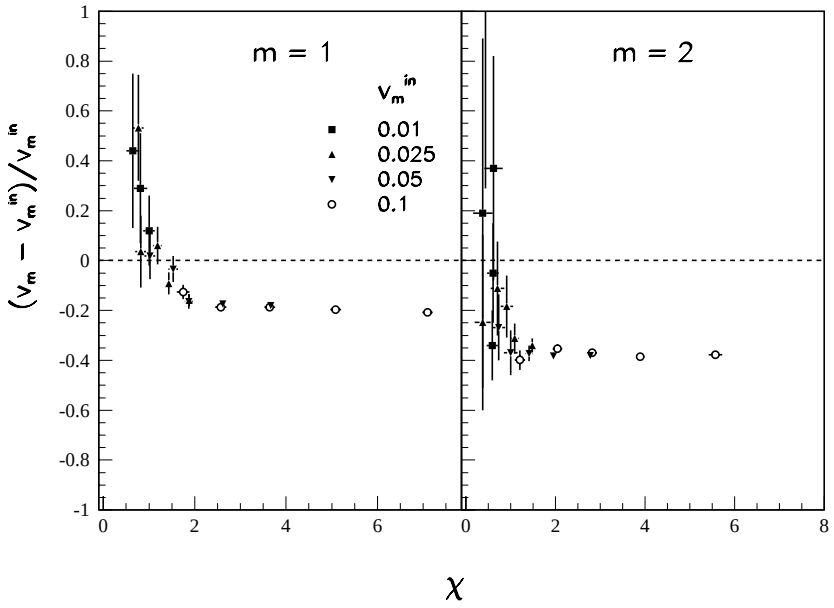

Figure 4.22: Fractional change in the observed value of v_m for photons as a function of measured anisotropy parameter χ, for different values of anisotropy and multiplicity. (a) for m = 1, directed flow, and (b) for m = 2, elliptic flow. The error bars are statistical.

4.3.2 Fluctuation in multiplicity and pseudorapidity distribution

4.3.2.1 Introduction

Recently the subject of event-by-event fluctuations of physical observables [21–24] such as particle multiplicity, transverse momenta, and the ratios of multiplicity of different particle species, have attracted a significant interest. The fluctuations in the above observables are related to fundamental properties of the system like specific heat, chemical potential, and matter compressibility. This may lead towards an understanding of thermalization and critical fluctuations at the QCD phase transition. Experimentally it is stimulated by the production of a large number of particles produced at such high energy collisions. This provides a unique opportunity for event-by-event analysis of fluctuations in such observables. The distributions of these observables are found to be near perfect Gaussian in experiments at SPS energies [25, 26].

Total particle multiplicity is sensitive to both initial-state and final-state interaction effects. The fluctuations in the initial stage arise due to (a) range of impact parameters, (b) fluctuations in the number of participants, and (c) fluctuations of the nucleon–nucleon cross section. The possible final-state effects are resonance production and rescattering. One can compare the experimental value with theoretical calculations taking the above factors into account to see whether the fluctuations are explained.

In a first-order phase transition, supercooling may lead to density fluctuations such as droplet formation and hot spots [27]. These may lead to rapidity fluctuations event-by-event. Rapidity fluctuations in the form of spikes and gaps have been observed in the $\overline{p}p$ experiment [28, 29]. Pseudorapidity distributions of charged particles observed in the JACEE experiment have also shown fluctuations [30]. In the present section we describe the power spectrum method to study fluctuations in pseudorapidty distributions.

4.3.2.2 Power spectrum technique

Event-by-event fluctuation in pseudorapidity distributions was studied using the power spectrum method [31–33]. The one-dimensional power spectrum for the rapidity distribution $f(y) = dN/dy$ can be written as [31]

$$\psi(\omega) = (2Y)^{-1} \left| \int_{-Y}^{Y} dy e^{2i\pi\omega y} [N f(y) - f_0(y)] \right|^2 , \tag{4.7}$$

where Y is the limit of acceptance, $f_0(y)$ is the average rapidity distribution of particles produced in a large number of events in the sample, and $N = \sum f_0(y) / \sum f(y)$ is a normalization factor which takes into account fluctuations in multiplicity in a given centrality window.

In a normal event $f(y)$ fluctuates around $f_0(y)$. These fluctuations constitute statistical noise. If an arbitrary non-statistical fluctuation (to be called 'signal') is superimposed above the noise, the power-spectrum can be used to extract the signal from the noise. A typical VENUS event modified to have an artificial spike in the pseudorapidity distribution within the PMD acceptance in the ALICE experiment is shown in Fig. 4.23. Such an event will henceforth be referred to as an 'exotic' event to distinguish it from normal VENUS events having only statistical fluctuation.

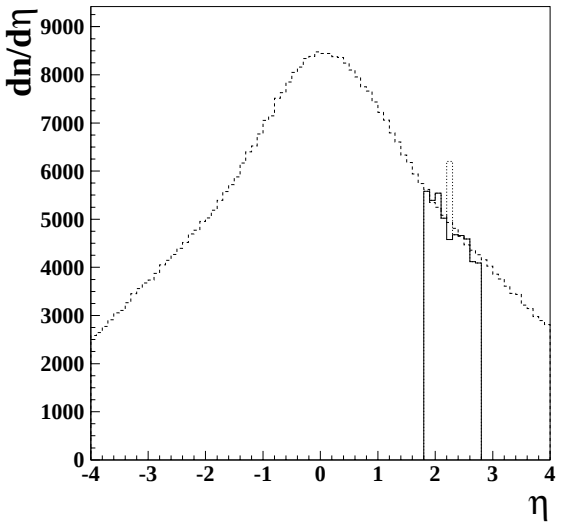

Figure 4.23: Pseudo-rapidity distribution of photons: the dashed line denotes the average for VENUS events, the solid line denotes one VENUS event in the PMD acceptance, and the dotted line shows a spike in one η-bin as described in the text.

Using the mixed event technique and artificially injected non-statistical fluctuations, it was demonstrated that a reference average power spectrum can be generated which is almost independent of the level of admixture of non-statistical fluctuation. This technique can be directly applied to the experimental data.

Figure 4.24(a) displays the mean power spectrum for 50 central Pb+Pb VENUS events at LHC energy (solid histogram). A peak is seen for a small value of ω, which arises due to correlations among photons. The mean power spectrum for 1000 mixed events generated from the above VENUS events is also shown by dashed lines. This is found to be quite flat. A dip observed at small ω is a characteristic of white noise. Similar behaviour is observed for the dispersion $D_\psi(\omega) = \sqrt{\langle \psi^2(\omega) \rangle - \langle \psi(\omega) \rangle^2}$.

The power spectrum of an event shows sharp peaks around the average value. One can select criteria in terms of the number of peaks above a designated threshold to reduce the statistical noise. It is found that normal events having more than three peaks above $\langle\psi(\omega)\rangle$ + 4 $D_\psi(\omega)$ are already below 0.2% for a sample of 1000 events. This can be taken as a criterion for labelling an exotic event.

Figure 4.24(b) shows the power spectrum for one event in which a non-statistical signal of strength 0.5% is injected in the form of a spike in one of the rapidity bins (solid histogram). For comparison, the threshold level at $\langle\psi(\omega)\rangle + 4D_\psi(\omega)$ is also displayed. It can be seen that the power spectrum of the exotic event shows prominent peaks beyond the threshold.

We have also investigated the possibility of detecting rapidity gaps by removing particles from a bin, randomly selected as earlier. We call this case a 'rapidity hole'. The above figure includes the power spectrum for one event with a rapidity hole (dash-dot histogram), which also shows prominent peaks.

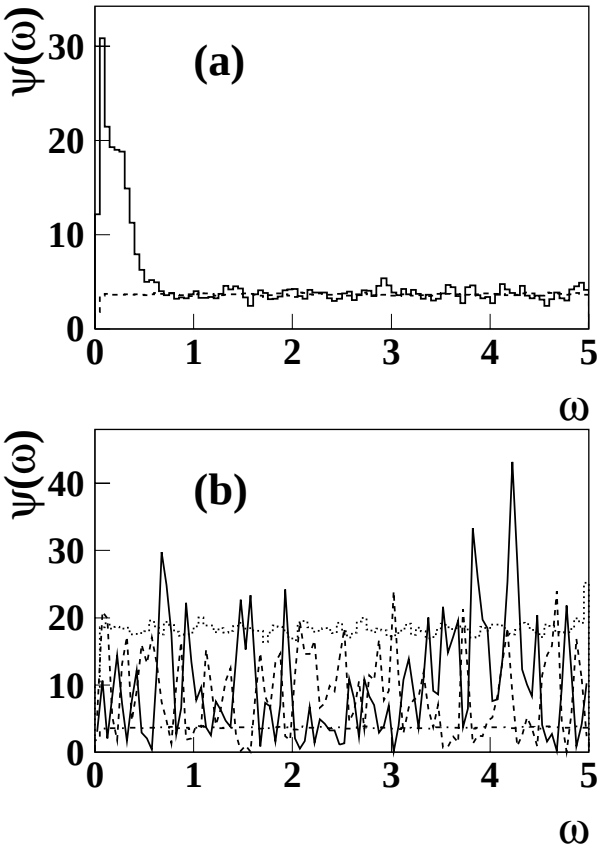

Figure 4.24: (a) Mean power spectrum for VENUS events (continuous line) and for mixed events (dashed line) at LHC energy. (b) Power spectrum of one event with a rapidity spike (continuous line) and a rapidity hole (dashed line). The dash-dot line represents $\langle\psi(\omega)\rangle$ and the dotted line is drawn at the threshold level $\langle\psi(\omega)\rangle$ + $4D_\psi(\omega)$.

4.3.2.3 Results

We present the results for filtering exotic events from a given sample of events. To quantify the efficacy of the method, we define the efficiency and impurity for selecting exotic events in the following way: Efficiency: the fraction of exotic events identified by the power spectrum method, Impurity: the fraction

Table 4.5: The efficiency (in the left column) and impurity (in the right column) for identifying exotic events at LHC energy for different values of P and R.

	Large coverage (–3:3)						PMD coverage					
R↓ \ P →	0.35		0.5		1		0.35		0.5		1	
1	37	33	93	13	100	12	20	50	73	28	100	33
5	35	11	89	5	100	4	25	13	86	4	82	4
10	31	7	90	2	100	3	28	6	87	2	83	3
20	27	4	89	1	100	1	33	2	84	1	87	2
30	33	2	90	1	100	1	23	2	82	1	84	1

of identified events belonging to non-exotic (i.e. statistical noise) category. We denote the strength of the signal by P. This is a small fraction of the multiplicity, added in a particular η-bin. R denotes the percentage of total events which are exotic. The results are presented for varying values of P and R in Table 4.5. It was found that the efficiency of selection is nearly independent of R, but the impurity is rather high for small values of P and R. Impurities are negligible at 5% level of admixture of exotic events, even for weak signals.

4.3.3 Disoriented chiral condensates

4.3.3.1 Introduction

Disoriented chiral condensates (DCC) have been predicted to form in high-energy nuclear collisions when the chiral symmetry is restored at high temperatures and densities. The formation of DCC may result in an excess of low momentum pions in a single direction in isospin space [34–38]. It has been estimated [34] that the neutral pion fraction, f, of pions from the DCC domain follows the probability distribution:

$$P(f) = \frac{1}{2\sqrt{f}} \qquad \text{where} \quad f = N_{\pi^0}/N_{\pi} \, . \tag{4.8}$$

N_{π^0} and N_{π} denote the number of neutral pions and total pions emitted from the domain, respectively. The pions in a normal event would follow a binomial distribution with a mean of 1/3. The formation of DCC would lead to event-by-event fluctuations in the number of charged particles and photons in a given phase space, since the majority of the photons originate from π^0 decay, and the contents of the charged particles are mostly charged pions.

In the ALICE experiment, the PMD, in conjunction with the FMD, should be able to effectively search for DCC. Here we describe some of the analysis methods developed for DCC search in the WA98 experiment and extrapolate the results to the LHC environment.

4.3.3.2 DCC search: methodology

The experimental observation of DCC depends on various factors, such as the probability of occurrence of DCC in a reaction, the number of possible DCC domains in an event, the size of the domains, the number of pions emitted from the domains, and the interaction of the DCC pions with the rest of the system [39–41]. In view of this, specific analysis techniques have been devised to search for DCC. The current techniques in DCC analysis [42] are the following:

- N_{γ} and $N_{\rm ch}$ correlation: a simple method to study the correlation of the number of photons and charged particles in an event over the entire phase space covered by the detectors, and also in smaller $\eta - \phi$ bins.

- Discrete Wavelet Analysis: a multi-resolution analysis technique capable of picking up fluctuations at different $\eta - \phi$ bins of phase space.
- Power spectrum analysis: a method for identifing interesting events with DCC.
- Robust observable: a method using various moments and combinations of these, calculated from the distribution of photons and charged particles in each bin.
- Event shape analysis: a method combining the wavelet technique and flow analysis.

Below we give details about each of these methods and discuss how they can be applied in the ALICE environment.

4.3.3.3 Simulation of DCC events

For simulations involving DCC domains, one needs to know the position of the domain, the size of the domain in (η, ϕ), and the number of DCC pions within the domain. The DCC events are generated from event generators (referred to as 'normal' events) by changing the relative population of charged and neutral pions [44] in the domain according to Eq. (4.8). Simulations were performed for the following three different scenarios [45].

- Assumption (1): All the pions within the chosen domain are assumed to be of DCC origin.
- Assumption (2): Since pions from DCC domains are of low p_{T}, we assume that out of all the pions present within the chosen domain, all pions with $p_{\mathrm{T}} <$150 MeV/c may be of DCC origin.
- Assumption (3): This corresponds to enhanced pion production in case of DCC formation. A number of low p_T pions, generated according to Eq. (4.8), are added within the chosen domain on top of the existing pions from normal events.

For Assumption (3), the number of additional pions depends on the size of the DCC domain and the energy density of the domain. DCC domain sizes of the order of $3-4$ fm in radius have been predicted by different theoretical models [46–48]. Assuming the energy density available for pion production within the DCC domain to be about 50–100 MeV/fm^3, the number of DCC pions is estimated to be between 50 and 200.

In order to be compatible with experimental observables, all simulations are carried out by taking detector effects such as acceptance and efficiency into account. With this, the simulated events are at par with the real data and can be analysed using common analysis tools.

4.3.3.4 DCC search using $N_\gamma - N_{\mathrm{ch}}$ correlation

In a given set of normal events, the N_γ and N_{ch} distributions are correlated. The presence of events with DCC would show up as deviations from this general correlation. The correlation between observed $N_{\gamma-\mathrm{like}}$ and N_{ch} can be studied using full detector coverage and also in smaller ϕ-segments. A common correlation axis (Z) can be obtained by fitting the above distributions. The closest distance (D_Z) of the data points to the correlation axis can be calculated with the convention that D_Z is positive for points below the Z-axis. The distribution of D_Z represents the relative fluctuations of $N_{\gamma-\mathrm{like}}$ and N_{ch} from the correlation axis at any given ϕ bin. In order to compare these fluctuations at different bins on the same level, one defines a scaled variable, $S_Z = D_Z/\sigma(D_Z)$, where $\sigma(D_Z)$ represents the width of the D_Z distribution for normal events. The presence of events with DCC domains of a particular size would result in a broader distribution of S_Z compared to those for normal events.

This method of analysis was applied to the data from the WA98 experiment [49, 50]. Preliminary results for the S_Z distributions for 2, 4, 8 and 16 bins in ϕ obtained for Pb+Pb collisions at 158·A GeV/c are shown in Fig. 4.25 where the data are compared to mixed events and simulation. The differences in the widths of the distributions can be quantified to indicate the presence of fluctuations.

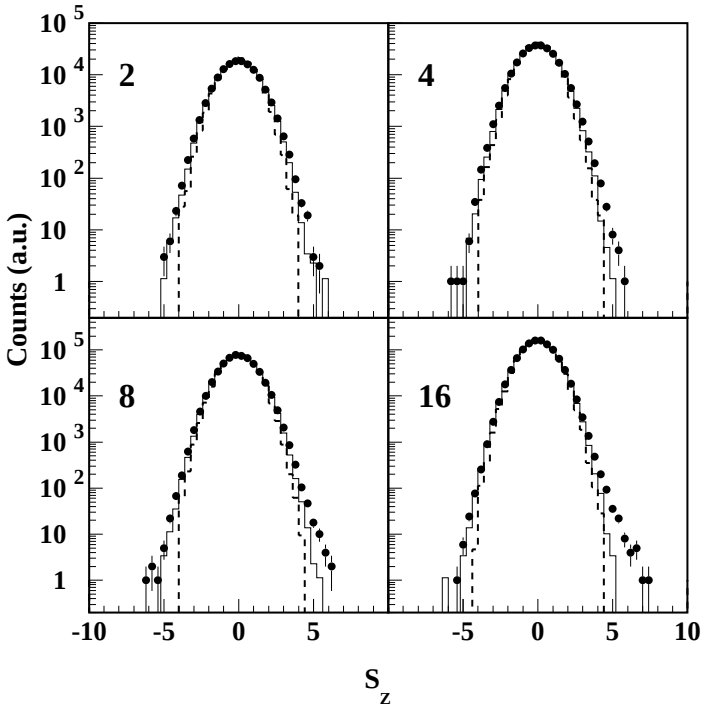

Figure 4.25: S_Z distributions for 2, 4, 8 and 16 divisions in azimuth. The solid circles denote the preliminary data from the WA98 experiment, the solid histograms are for mixed events, and the dashed histograms are for simulations using VENUS events processed through GEANT.

4.3.3.5 DCC search using DWT technique

The method of discrete wavelet transformation (DWT) can be adopted to search for fluctuation in the neutral pion fraction, f, at different scales. The ability of this technique to search for localized DCC domains has been demonstrated in Refs. [45, 51, 52].

The phase space of the PMD and the charged particle detector can be divided into small bins in ϕ, the number of bins in a given scale j being 2^j. The input to the DWT analysis is a spectrum of f at the smallest bin, corresponding to the highest resolution scale, $j_{\max}$. The output of the DWT consists of a set of wavelet or father function coefficients (FFCs) at each scale, from $j = 1,...,(j_{\max} - 1)$.

The distribution of FFCs for normal events is gaussian in nature. The presence of DCC-like fluctuation makes the FFC distribution non-gaussian, with a larger r.m.s. deviation, as shown in Fig. 4.26. The dotted histogram in the figure is for normal events for semi-central collisions at the LHC, and the solid histogram is for events with a DCC domain of 45° in ϕ.

Comparing the r.m.s. deviations of the FFC distribution of data, mixed, and simulated events, one can get an idea about the localized fluctuations in the distributions of $N_{\gamma-\text{like}}$ and N_{ch}. This technique has been effectively applied to the WA98 data to study the presence of non-statistical fluctuations [50].

A more quantitative way to analyse the fluctuations at each scale is the wavelet power spectrum, constructed from the corresponding FFC values [51, 52]. For normal events, the FFC power spectrum will show a flat distribution without a structure at any scale. But for events with DCC-like fluctuations, the power spectrum is expected to show an enhancement at scales below the specified domain size.

It has been observed that the majority of the DCC-type of events show up at the tails of the FFC and S_Z distributions. Using a high-statistics data set one can analyse only the tail part of the distribution to enhance the signal-to-background ratio.

The amount of broadening in the FFC distributions depends on various factors associated with DCC domains, and can be quantified by the r.m.s. deviations (ξ) of the distributions. One can then compare

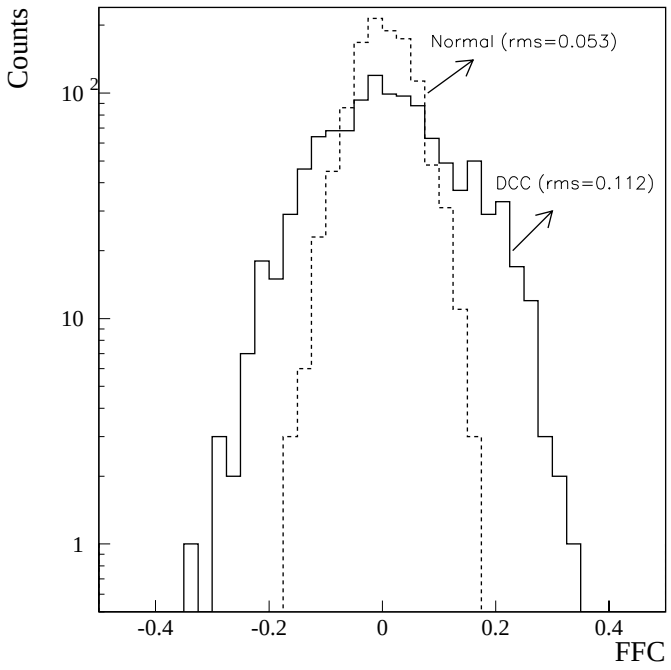

Figure 4.26: The FFC distributions at scale $j = 1$ for VENUS events (dotted histograms), and DCC type of events (solid histograms), with DCC domain size $\Delta\phi = 45^\circ$. The simulation is performed by taking $N_\gamma = 1250$ and $N_{\rm ch}$ = 1600.

different distributions by the strength parameter [45] defined by:

$$\zeta = \frac{\sqrt{(\xi^2_{\rm DCC} - \xi^2_{\rm normal})}}{\xi_{\rm normal}}\ , \tag{4.9}$$

where $\xi_{\rm normal}$ is the r.m.s. deviation for normal events, and $\xi_{\rm DCC}$ is the r.m.s. deviation for a sample of events having built-in DCC domains.

Figure 4.27 shows the simulation results on the strength contours [45] at SPS energy for different domain sizes and probabilities of occurrence of DCC-type events. The top panel of the figure shows the strength contours at two scales $j = 1$ and $j = 2$ for assumption (1), and the bottom panel shows the same for assumption (3), corresponding to 100 additional DCC pions at four scales.

The figures indicate that the method is sensitive to very low values of the probability of occurrence of DCC events ($\sim$ 1%) for domain sizes of 90° and above where $j = 1$, and $40-60^\circ$ for $j = 2$. From the values of ζ at different j's, one may draw inference about the size and probability of occurrence of a possible DCC domain. The sensitivity of the method has been seen to increase [45] with increasing multiplicity.

4.3.3.6 DCC search using power spectrum

The power spectrum technique can be easily applied to study event-by-event fluctuation in the azimuthal distribution of N_γ, $N_{\rm ch}$, and $N_\gamma/N_{\rm ch}$ over limited ϕ-regions typical of DCC domains.

The ratio $f_1 = N_{\gamma-{\rm like}}/N_{\rm ch}$ is computed for a window $\Delta\phi$ in azimuth starting from any selected ϕ-value. The window is then displaced by a small amount (usually by a few degrees) and f_1 is computed again for a window of the same size. In this way one obtains a set of f_1 values for one event, to construct

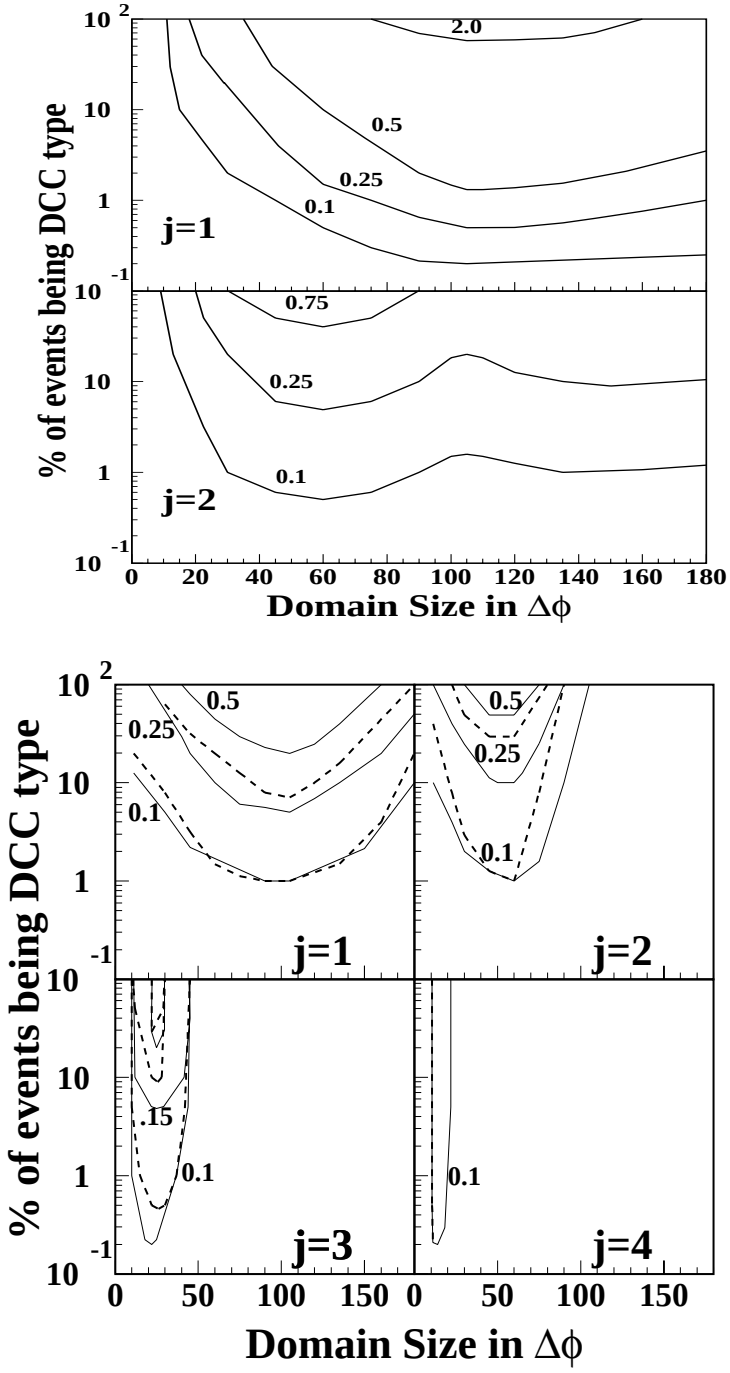

Figure 4.27: Strength contours derived from FFC distributions. Top: for assumption 1 at $j = 1$ and $j = 2$. Bottom: for assumption 3 at $j = 1 - 4$ (solid curves are for 100 additional pions and dashed ones are for 60).

a $df_1/d\phi$ distribution. The power spectrum of this distribution is then obtained in a manner similar to that described in Section 4.3.2.2. For finding DCC events, an average power spectrum is calculated and thresholds determined, so that normal events show very small statistical fluctuation above the selected threshold.

The capability of the method was tested by generating a set of 5000 events having a multiplicity of 4000 for both charged particles and photons within the PMD acceptance. The azimuthal distribution of particles within this set of events is uniform and these events are referred as 'normal' events. Another set of 5000 events are generated such that in each event a domain of size $\delta\eta$ = 0.1 and $\delta\phi$ = 40° represents a DCC distribution of particles according to Eq. (4.8). This domain represents 1% of the multiplicity within the PMD acceptance and is of the DCC type. The domain is selected randomly in azimuth, for each event.

The average power spectrum is generated for a set of normal events, and selection criteria for a small statistical fluctuation is determined. By taking a threshold at four standard deviations, it is found that only 3% of the normal events are selected. With the same selection criteria, the DCC events can be selected with 60% efficiency. The window size $\Delta\phi$ taken in the present investigation is arbitrary. One will have to study the selection efficiency for several values of $\Delta\phi$. The truly abnormal events will be selected in several window sizes.

4.3.3.7 DCC search using robust observables (moments analysis)

This is a multi-resolution analysis technique based on bi-variate factorial moments [53]. A set of robust observables is defined by:

$$R_{i,1} = \frac{F_{i,1}}{F_{i+1,0}} \tag{4.10}$$

where

$$F_i \equiv \frac{\langle N(N-1)\ldots(N-i+1)\rangle}{\langle N\rangle^i} \tag{4.11}$$

and

$$F_{i,j} = \frac{\left\langle N_{\rm ch}(N_{\rm ch}-1)\ldots(N_{\rm ch}-i+1)\; N_\gamma(N_\gamma-1)\ldots(N_\gamma-j+1)\right\rangle}{\langle N_{\rm ch}\rangle^i \left\langle N_\gamma\right\rangle^j} \,. \tag{4.12}$$

For an inclusive analysis, N denotes the particle multiplicity in an event and averages (denoted by $\langle..\rangle$) are taken over a large number of events. For event-by-event analysis, when the multiplicity is high, the phase space region is divided into a number of bins. In this case N denotes the multiplicity in a bin and averages are taken over the total number of bins [54].

The most interesting observation is that for all $i \geq 1$,

$$\begin{aligned} R_{i,1}(\text{normal events}) &= 1, \\ \text{and} \qquad R_{i,1}(\text{DCC}) &= \frac{1}{i+1} \,. \end{aligned} \tag{4.13}$$

There is a strong correlation between $R_{i,1}$ and i, which is absent for normal events. This behaviour is shown in Fig. 4.28 for inclusive analysis. Similar behaviour is expected for event-by-event analysis in the high multiplicity environment at LHC energies.

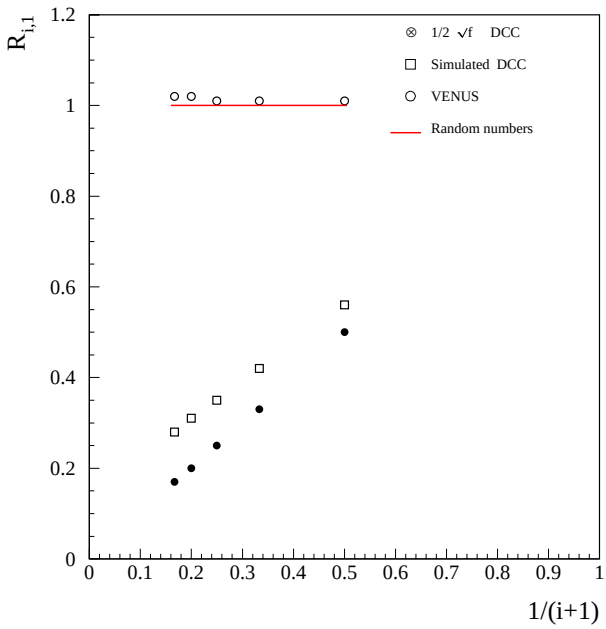

Figure 4.28: Results of inclusive DCC analysis using robust observables. Normal VENUS events do not show any correlation whereas pure DCC events follow the relationship given in Eq. (4.13). The simulated DCC events generated by taking detector effects into account follow a similar behaviour to that of pure DCC events.

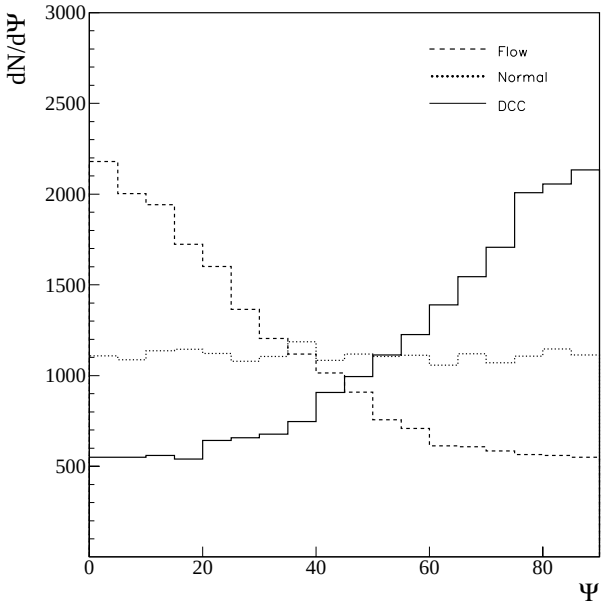

Figure 4.29: Ψ-distribution for normal, flow and DCC events.

4.3.3.8 DCC search through event shape analysis

With this method we search for DCC domains using established flow analysis techniques in heavy-ion experiments [44]. It is based on the realisation that localized DCC formation is expected to lead to an event shape anisotropy which is out of phase for charged particles and photons.

In the case of two detectors with the same phase space ($\eta - \phi$) coverage, one detecting photons and the other detecting charged particles, if there is a genuine flow in a particular event both detectors would show the effect in terms of respective flow angles (Ψ_m^{γ} and Ψ_m^{ch}) being aligned in the same direction. Therefore the distribution of $\Psi(= \Psi_m^{\gamma} - \Psi_m^{\mathrm{ch}})$, the difference between the flow angles, as obtained for the two detectors is expected to peak at zero. However, in the case of DCC being prominent in a particular region, more particles of one type will be detected in one of the detectors in the same region of phase space. The two flow angles in this case will be out of phase.

The results are shown in Fig. 4.29 for a second-order Fourier analysis. The dotted line corresponds to normal events which do not show any correlation. The dashed line corresponds to events with flow, and the solid histogram shows the case with only DCC. The presence of DCC leads to an anti-correlation of flow angles in the two detectors peaking at 90° in the second-order analysis.

In ALICE this technique can be easily applied to the $\eta - \phi$ particle distributions within the common coverage of the PMD and the FMD. Furthermore, higher multiplicity will lead to a better determination of the flow angle.

5 Installation and Organization

5.1 ALICE experimental area

5.1.1 Underground area

The ALICE detector will be installed at Point 2 of the LHC accelerator [1]. The Point 2 experimental area was designed for the L3 experiment. The main access shaft, 23 m in diameter, provides a 15×7 m^2 installation passage and space for counting rooms. The counting rooms are separated from the experimental area by a concrete shielding plug (see Fig. 5.1). The experimental cavern is 21.4 m in diameter and will be re-equipped with a 2×20 t crane having a clearance of about 3 m over the L3 magnet. The L3 magnet provides a 11.6 m long and 11.2 m diameter solenoidal field of up to 0.5 T. The end-caps have a door-like construction. The door frames will support large beams traversing the L3 magnet, from which the ALICE central detectors will be supported.

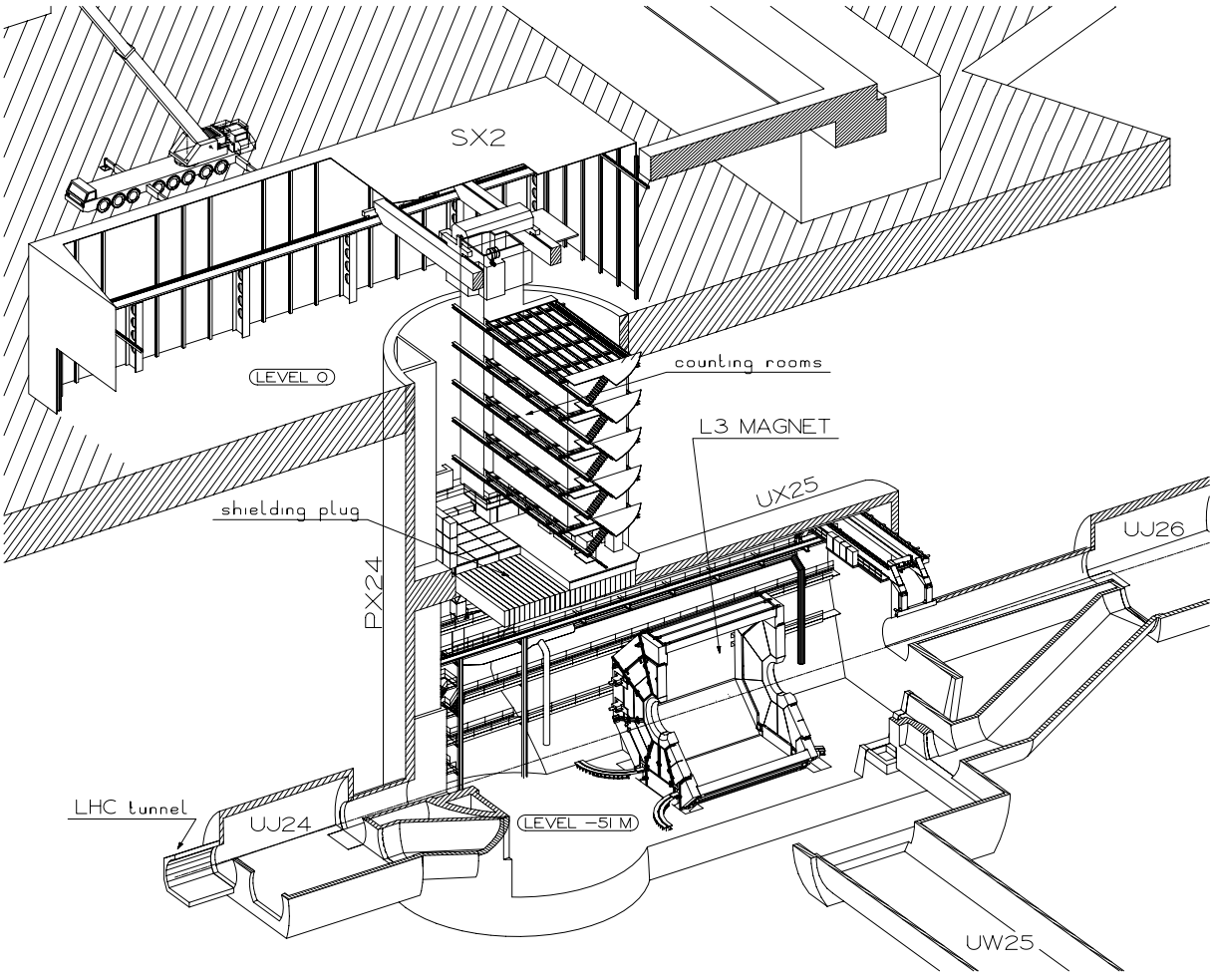

Figure 5.1: General layout of the basic underground structures at Point 2, showing the L3 magnet and the counting rooms.

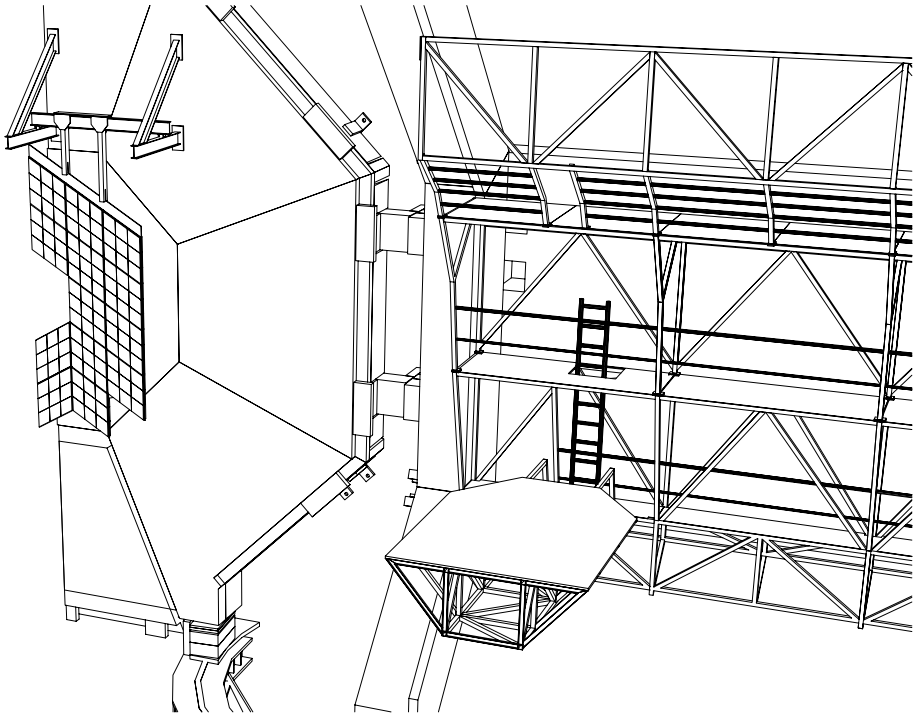

Figure 5.2: General layout of the PMD attached to the L3 magnet door structure.

5.1.2 Surface facilities

The present surface zone at Point 2 includes sufficient assembly-hall space to meet the ALICE requirements and no new hall construction will be necessary for the detector assembly. The overall ALICE work schedule foresees a pre-installation phase of the PMD, which will take place in the SXL2 assembly hall at Point 2. This will allow an early preparation of the different support structures and services, and the installation procedure to be analysed and corrected before integrating the detectors into the experimental area.

5.2 Integration and assembly of the PMD

5.2.1 General installation considerations

The PMD is divided into two identical half-planes, each attached to the two parts of the L3 door structures, as indicated in Fig. 5.2. In the closed position the PMD will obstruct the access into the L3 magnet volume and the PMD half-planes are therefore retractable perpendicular to the axis of the vacuum chamber. The PMD does not restrict the opening of the L3 magnet doors nor the displacement of the spaceframe.

5.2.2 Pre-installation phase

The supermodules and support structures will be delivered to Point 2 for final assembly in the SXL2 assembly hall prior to the installation in the underground area. This will allow an early preparation of the various detector services and permit the installation and access scenarios to be analysed and corrected before lowering the PMD planes into the experimental cavern. Since the PMD is independent of any new support structure or preparation in the experimental area it is conceivable that a pre-installation test of the PMD will be performed directly on the L3 magnet doors.

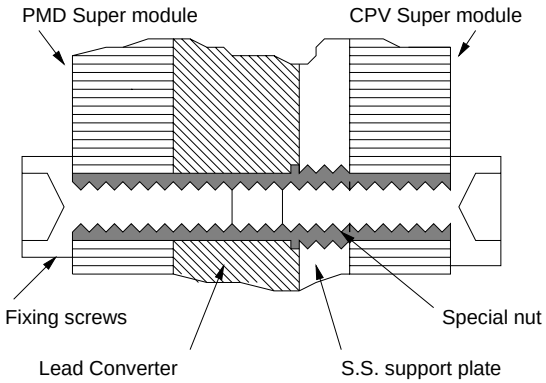

Figure 5.3: Special nut–bolt for fixing the supermodules on the SS plate.

5.2.3 Mounting of converter and supermodules

During the pre-installation phase the suspension beams and the support plates will be temporarily installed in the surface building.The lead-converter plates and the supermodules will be mounted on the support plates according to the following steps.

- Fixing the lead-converter pieces onto the support plate using the pre-fabricated tapped holes, as described in Chapter 3.
- Positioning and fixing the special studs at appropriate locations to fix the veto and preshower supermodules back-to-back.
- Fixing the supermodules using the special nut-bolt shown in Fig. 5.3. The outer threading of this bolt will be fastened to the tapped holes in the support plate. The supermodules will then be held in place with smaller (thinner) bolts inside the threaded hole.
- Fixing the preformed gas in/out piping on the boundary of the support plate (see Fig. 5.8). This piping is provided with a number of parallel feed points conveniently located to provide gas inlet to all supermodules in each half of the detector.

5.2.4 Installation in the underground cavern

The size and weight of the PMD permits the complete planes to be lowered into the experimental area and placed directly in their final position on the L3 magnet doors. The installation procedure can be divided into the following main phases:

- Installation of the support beams and hydraulic moving system on the L3 magnet door,
- Installation of the fully assembled PMD planes,
- Connection of services.

5.3 Interface with LHC: the ALICE vacuum chamber

A detailed description of the complete ALICE vacuum-chamber system can be found in Ref. [2]. An effort has been made to minimize the material in the part of the vacuum chamber on the PMD side of the interaction point in order to reduce the background in the PMD. A cost-effective solution has been found in using an undulated design as indicated in Fig. 5.4. Dimensional details of the vacuum chamber are given in Table 5.1.

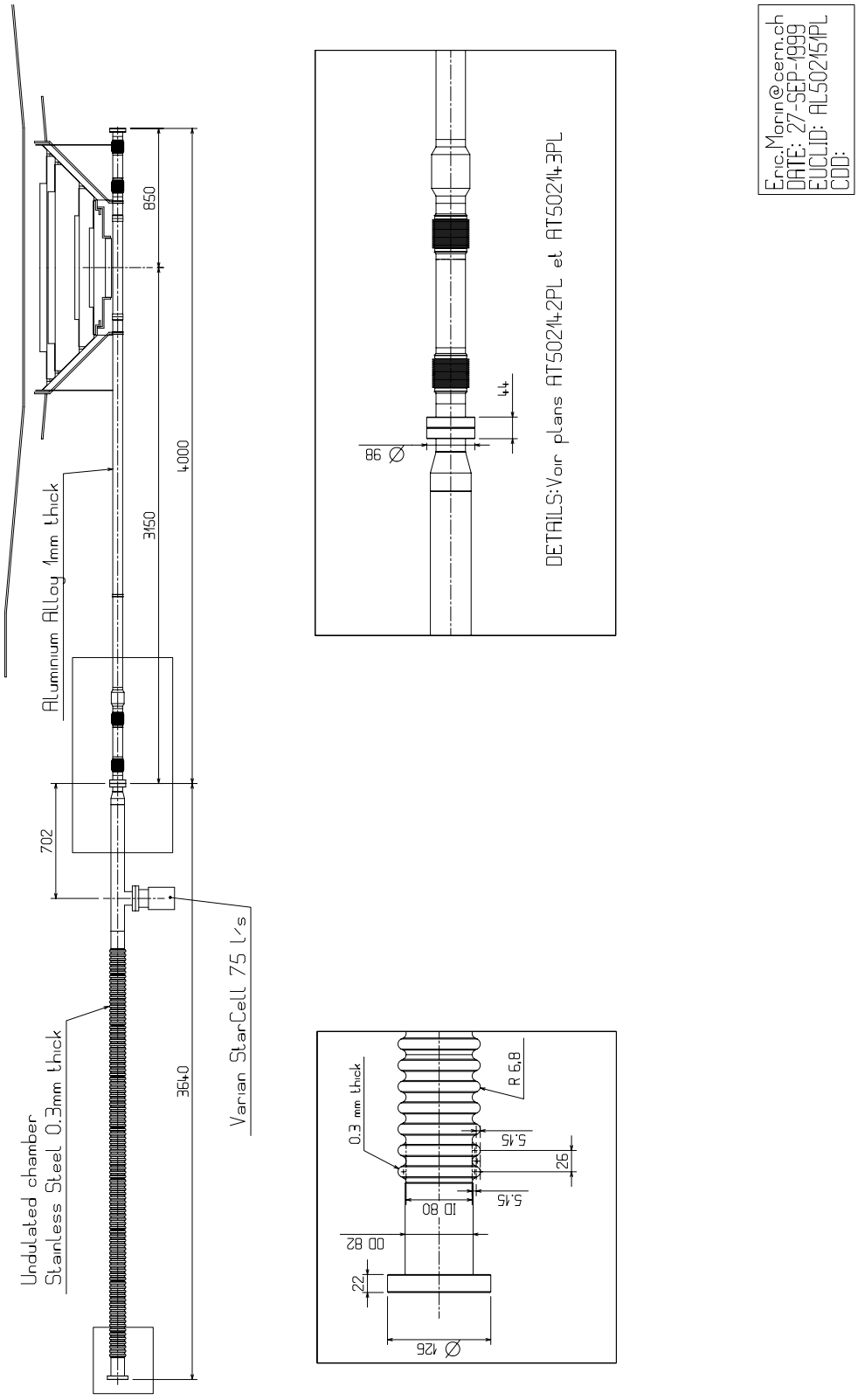

Figure 5.4: Conceptual layout of the ALICE vacuum-chamber system in the PMD region.

Table 5.1: Parameters of the ALICE vacuum chamber

Element	Sub-element	Nominal I.D. (mm)	Wall thickness (mm)	Material
CP	CP/1	58	1	Beryllium
	CP/2	58	1	Aluminium
	CP/3	58	0.8	Austenitic stainless steel and 2 bellows
	CP/4	58	0.8	Austenitic stainless steel and 2 bellows
RB24	RB24/1	58	1	Austenitic stainless steel and ion pump
	RB24/2	80	0.3	Corrugated austenitic stainless steel

It should be noted that Table 5.1 gives only nominal dimensions of the vacuum chamber. They do not include envelopes for tolerances, local shape distortions or bake-out equipment.

5.4 Detector support services

5.4.1 Gas supply system

5.4.1.1 Introduction

The gas supply system consists of a single-pass design that distributes gas to all the supermodules. The detector will have eight volume changes per day. The half-planes of both the preshower and the veto detectors have identical volumes of 60 litres each. The flow rate in each half plane is approximately 20 l/h. The preferred gas for the system at the present time is a mixture of argon and carbon dioxide (70 : 30). The working pressure of the chambers will be 1 mbar. The design parameters of the system can be seen in Table 5.2.

Table 5.2: Parameters of the gas system for the PMD

Total volume	0.240 m^3
Number of chambers	52
Chamber volume	0.0045 m^3
Volume exchange/day	8
Total flow rate	80 l/h
Working pressure	1 mbar

Primary mixing and pressure regulation will be carried out in the surface gas building (SGX). The final distribution and flow control to the individual chambers will take place on the shielding plug area in the access shaft (PX24), which is accessible during LHC machine operation. An overview of the system can be seen in Fig. 5.5.

Figure 5.6: Gas mixer unit located in the surface building.

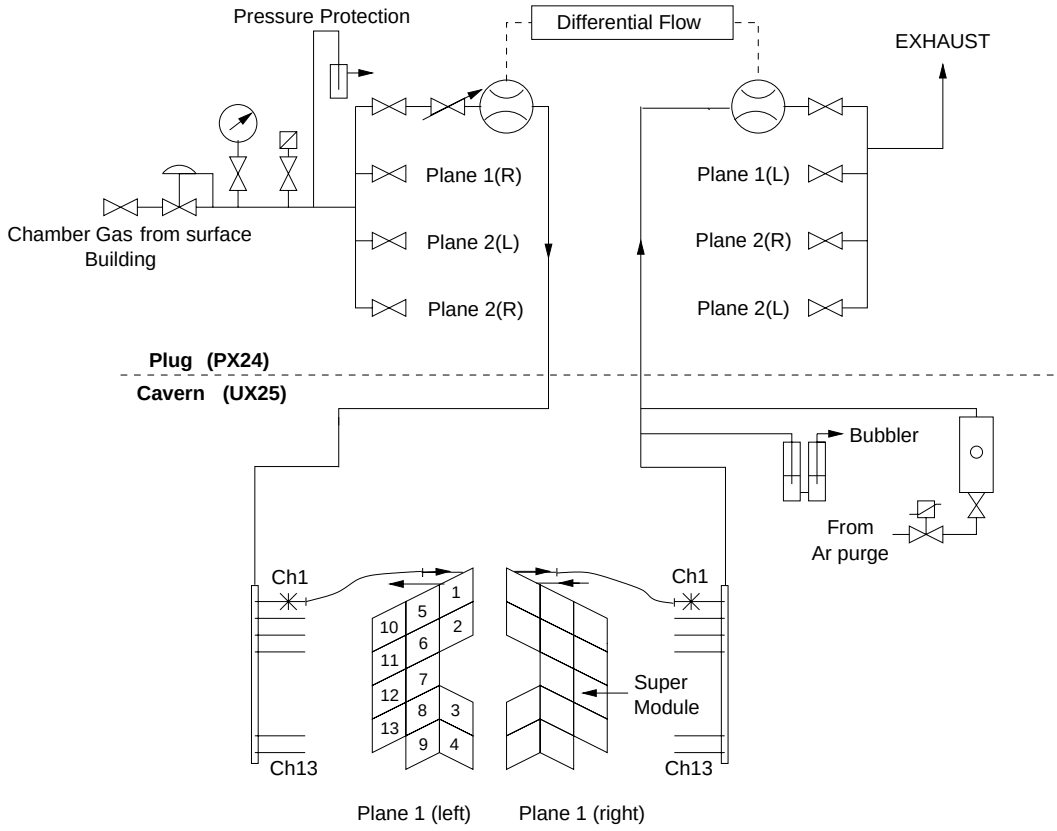

Figure 5.7: Flow distribution scheme for the four detector half-planes.

5.4.1.3 Distribution system

Pressure regulation and flow distribution to each plane will take place on the shielding plug area. Gas entering the distribution manifold from the mixer will pass through a common pressure regulator before being distributed to each plane. A safety relief device is incorporated into the distribution manifold to prevent over-pressure of the chambers, and will either be a simple relief valve or a rupture disc, depending on the pressure limits.

Each distribution channel will incorporate a throttle valve to regulate the flow of gas to each of the four half-planes, see Fig. 5.7. If a suitable low-cost differential flow-meter can be obtained each of the four distribution channels will be monitored, allowing a direct comparison between inlet and outlet flow.

A set of distribution manifolds will be incorporated into the system, and will be installed in close proximity to the detectors. This is shown in Fig. 5.8. These manifolds supply gas to each of the 13 individual chambers on each half-plane. Each channel has a short, flexible, metallic pipe with self-sealing quick connector on both inlet and outlet lines. This permits individual channels to be disconnected from the circulation system for flushing with gas and exhausting to a separate vent line. The return gas from the chambers will be exhausted into the dedicated extraction system on the plug.

5.4.1.4 Distribution pipework

All pipes and fittings within the system will be made of stainless steel. Existing gas pipes at Point 2 will be re-used as far as possible. Table 5.3 shows an overall view of the main piping parameters. At the shielding-plug end they will be modified to link up to the new distribution rack. In the experimental area (UX25) they will be extended into the L3 magnet and up to the chamber manifolds.

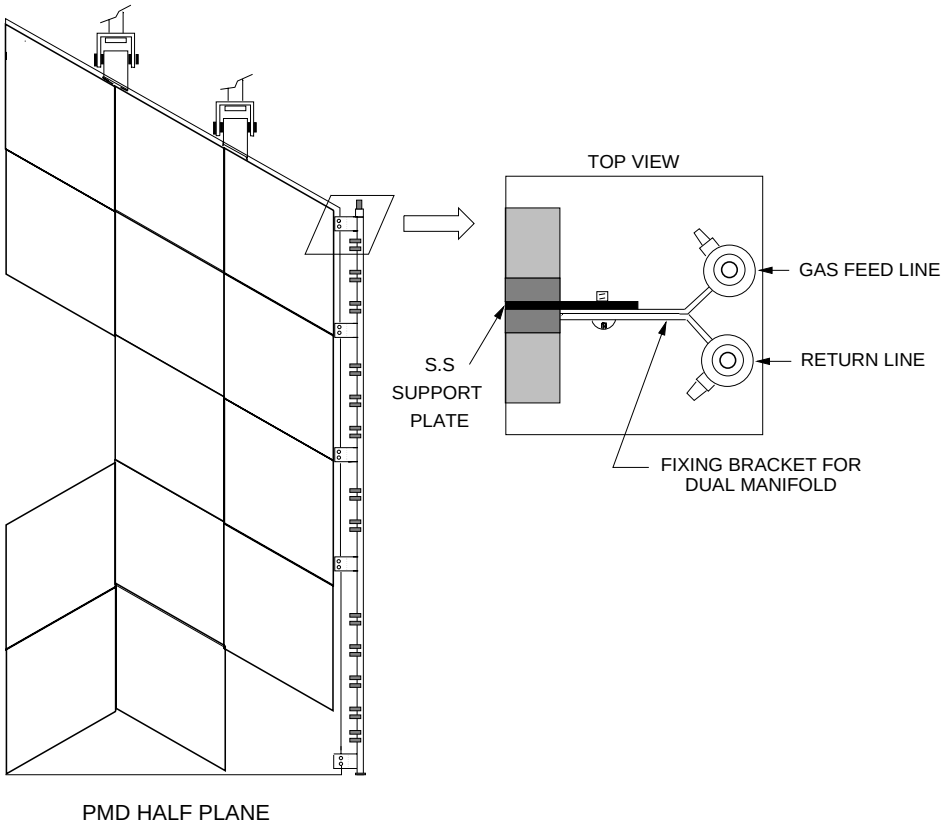

Figure 5.8: Details of the dual-gas manifold at the edge of the PMD half-plane. Each of the feed and return manifolds are provided with 13 pairs of quick connectors for veto and preshower supermodules.

Table 5.3: Parameters of the gas system for the PMD

	No.	Size
SGX-plug	1	22/20 mm
Plug-manifolds	4	16/14 mm flow
	4	18/16 mm return
Manifolds-chambers	52	6/4 mm flow
	52	10/8 mm return

5.4.2 Detector control system

5.4.2.1 General architecture

The ALICE Detector Control System (DCS) is characterized in Ref. [3] and will also be described in detail in the ALICE Computing Technical Proposal. Two major modes of operation will be implemented in the DCS.

(a) In normal operation during data-taking, a controlled start, operation and shutdown of the different sub-detectors will be provided. For this purpose standard operator commands will be available. Malfunctioning will be signalled through centralized alarms. The DCS will be accessed through a global experiment control system and data exchange with DAQ will be provided.

(b) During all other periods the detectors will be operated as required. While operating a part of the detector, access from remote location will be provided.

The above functions will be achieved on the basis of distributed intelligence. Scalability and modularity will be important features of the DCS. In order to obtain fast response and deterministic behaviour, the DCS will be based on a client/server model. At the level of the experiment, networked general-purpose workstations will be dedicated to the management of configuration data of all detectors and equipment, alarms, logging, archiving and data communication. Dedicated controller stations will control the individual detectors. The communication link at the controller level will be based on the recommendations of the CERN Working Group on Field Buses [4]. Remote sensing and actuator equipment at the detector level and in the electronics crates and ancillary equipment, such as safety and general electricity, will be connected either directly to one of the proposed standard buses or via suitable controllers. A supervisory and configuration software system will provide a uniform and coherent user interface to all detectors.

The DCS will have a three-layer design:

- **process layer** for field instrumentation, like sensor heads and actuators;
- **control layer** to interface the process equipment with multipurpose controller stations (using programmable logic controllers); and
- **supervisory layer** consisting of general-purpose workstations linked to the control layer through networks providing TCP/IP communication.

The workstations will be set up as supervisory stations providing the man–machine interface. The controller-level software, which will reside in the control computers linked directly to the process, will be configured individually for each sub-detector.

5.4.2.2 The DCS for the PMD

The DCS of the PMD will provide the following functions:

- control and monitoring of gases flowing through the supermodules,
- control and monitoring of power supplies for the front-end electronics,
- control and monitoring of the HV power supplies,
- monitoring of the temperatures on the supermodules.

The signals to be controlled and monitored for the PMD are listed in Table 5.4.

Table 5.4: Main parameters of the detector control system for the PMD

Systems	Location	Control parameters	Number	Type	Parameters	Control
Gas supply	PX24	Primary flow	2	Analog	Flow	Read
	PX24	Primary pressure	2	Analog	Pressure	Read
	PX24	Safety switch	4	Binary	Voltage	On/Off
LV	PX24	Readout elect.	52	Analog	Voltage	Read/Write
	PX24	Signal control	52	Binary	Voltage	On/Off
	PX24	Current monitoring	52	Analog	Current	Read
	PX24	Current limits	52	Binary	Thresholds	Read/Write
HV	PX24	Chamber voltage	52	Analog	Voltage	Read/Write
	PX24	Chamber current	52	Analog	Current	Read
	PX24	Current limits	52	Analog	Voltage	Read/Write
Temp.	Detector	Temperature	52	Analog	Temp.	Read

5.5 Access, maintenance and services

5.5.1 Access for maintenance and repair

Access to the various parts of the PMD for maintenance is straightforward. Access platforms inside the L3 magnet permit easy access to the front face of the PMD. By displacing the detector planes away from the L3 magnet door (see Chapter 3), access is also provided to the back face of the detector.

In order to provide access into the L3 magnet volume the PMD half-planes must be displaced perpendicularly to the beam axis. The top part of Fig. 5.9 shows the PMD in a closed position and the bottom part shows the half-planes moved apart by about 2 m.

5.5.2 Services

The total heat dissipation for the PMD is about 2 kW. This heat cannot be dissipated into the closed volume of the L3 magnet and will therefore be removed by a fluid cooling system and channelled towards a centralized heat-exchanger unit, which will remove the heat using the CERN mixed water system. These units will be located outside the L3 magnet inside the experimental area.

The gas supply system is described in Section 5.4.1. The HV and LV power supplies will be located in racks in the PX24 counting rooms. Cables from the racks will run in flexible cable trays to the PMD, which will allow movement of the PMD half-planes for maintenance without disconnection. This will eliminate the need for patch panels.

5.6 Safety aspects

The PMD has been the subject of a recent Initial Safety Discussion [5]. The outcome of this ISD was that the PMD does not present any safety risks.

The PMD uses non-flammable gas (Ar / CO_2) and the complete absence of toxic, corrosive, or flammable components makes the PMD an intrinsically safe detector. The PMD is attached to the L3 magnet doors and can be installed directly by the cavern crane, without any interference from other detectors. Apart from the standard load test of the main support structure, installation and access are not a problem for the PMD.

The closed volume inside the L3 magnet will be monitored separately for both flammable gas and oxygen deficiency. Access to the inside of the L3 magnet will be restricted.

The high and low voltages applied to the detector are provided by commercially available and certified power supplies, equipped with a large range of supervision and control functions. All insulation

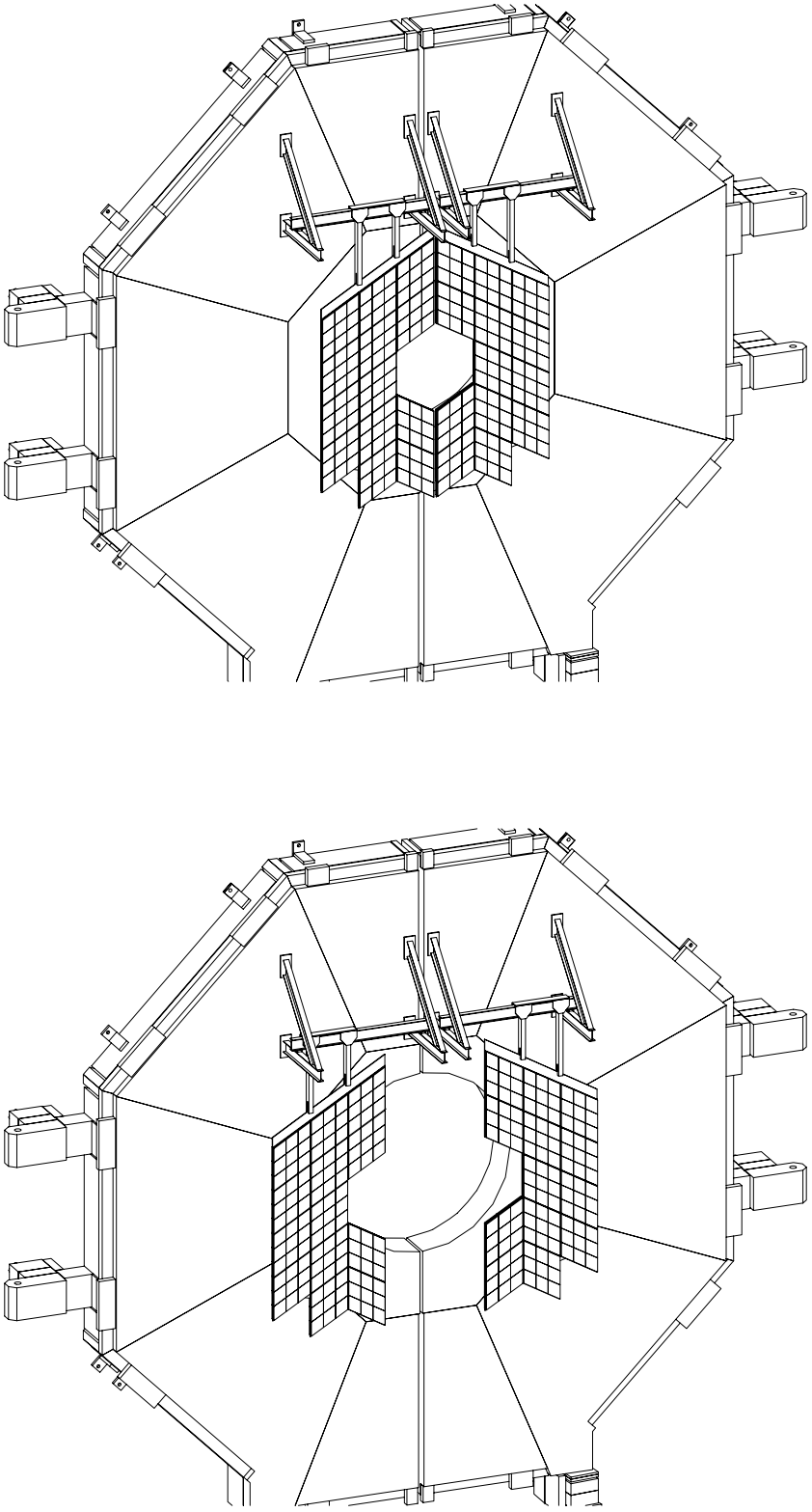

Figure 5.9: Top: Closed configuration of the PMD assembly. Bottom: Open configuration showing the PMD half planes moved apart by about 2 m.

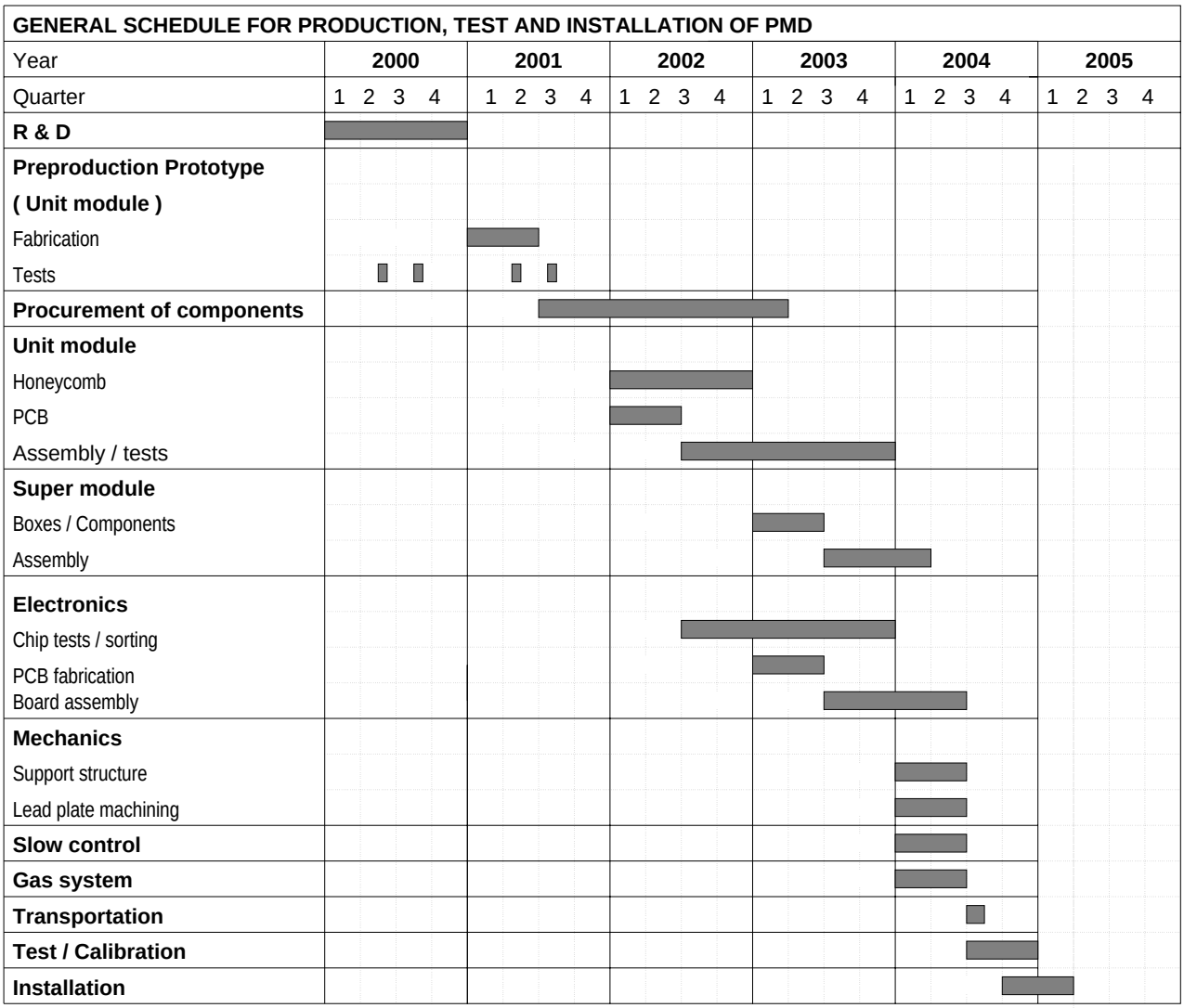

Figure 5.10: General schedule for the production, testing, and installation of the PMD.

materials and cables will conform to CERN Safety Instruction TIS IS41 (The use of plastic and other non-metallic materials at CERN with respect to fire safety and radiation resistance).

5.7 Milestones

5.7.1 Construction schedule

The assembly of the unit modules will be carried out at four different institutes (see Table 5.5) and will be completed 18 months after finalization of the design and procurement of components. The assembly of the supermodules will take nine months. Figure 5.10 shows the general planning for the production and installation of the PMD.

Some R&D effort will be required to study the timing properties of the extended cathode-type honeycomb chambers and the usefulness of the silicon-mode operation of the GASSIPLEX chip in high-rate environments.

5.7.2 Installation schedule

The overall ALICE planning foresees a pre-installation phase of the PMD, which will take place in the assembly hall SXL2 at Point 2 during the last quarter of 2004. This will allow an early preparation of the different support structures and services, and the installation procedure to be analysed and corrected before integrating the detectors into the experimental area. The installation of the PMD is independent of the installation of other sub-detectors.

5.8 Organization

5.8.1 Participating institutions

The following institutes will participate in the construction and operation of the PMD:

- Institute of Physics, Bhubaneswar
- Variable Energy Cyclotron Centre, Calcutta
- Panjab University, Chandigarh
- University of Rajasthan, Jaipur
- University of Jammu, Jammu

5.8.2 Responsibilities

The proposed sharing of responsibilities during the construction and operation of the PMD is shown in Table 5.5

Table 5.5: Sharing of responsibilities

Item	Institutions
Unit modules	Bhubaneswar, Calcutta, Jaipur, Jammu
Mechanics/support	Calcutta
Supermodule assembly	Calcutta
Slow control	Calcutta
Electronics	Calcutta, Chandigarh, Jammu
Software	Bhubaneswar, Calcutta, Chandigarh, Jaipur, Jammu

5.9 Cost estimate and resources

The cost of the PMD is dominated by the cost of the readout electronics. The estimates presented in Table 5.6 are based on the assumption of 200,000 channels of readout electronics. This includes the digitizer and the zero-suppression logic and accessories based on the readout concept of the tracking chambers of the dimuon spectrometer [6]. Other costs are based on current market prices.

The manpower necessary for the construction, testing, installation and commissioning of the PMD will be provided by the participating institutes.

Table 5.6: Cost estimates

Item	Cost (kCHF)
Detector	130
Readout electronics	600
Mechanics & services	160
Data transfer	45
Transportation	10
TOTAL	945

References

Chapter 1

[1] ALICE Collaboration, Technical Proposal, CERN/LHCC/95–71 (1995).
[2] A.K. Dubey et al., ALICE Internal Note INT-99-16 (1999).
[3] M.M. Aggarwal et al., Nucl. Instr. Meth. in Phys. Res. **A372** (1996) 143.
[4] M.M. Aggarwal et al., hep-ex/980726, Nucl. Instr. Meth. in Phys. Res. **A421** (1999) 558.
[5] ALICE HMPID Technical Design Report, CERN/LHCC 98-19 (1998); J.C. santiard et al., ALICE Internal Note, under preparation.
[6] W. Reisdorf and H.G. Ritter, Ann. Rev. Nucl. Part. Sc. **47** (1997) 663.
[7] P. Danielewicz, e-print Nucl-th/9907098.
[8] D.H. Rischke, Nucl. Phys. **A610** (1996) 88c; J.Y. Ollitrault, Nucl. Phys. **A 638** (1998) 195c.
[9] S.A. Voloshin and A.M. Poskanzer, e-print Nucl-th/9906075.
[10] M.M. Aggarwal et al., WA93 collaboration, Phys. Lett. **B403** (1997) 390.
[11] G.C. Mishra, Ph.D. Thesis, Utkal University (1999).
[12] R. Raniwala, S. Raniwala and Y.P. Viyogi, ALICE Internal Note 99-32 (1999).
[13] J.D. Bjorken, Int. J. Mod. Phys. **A7** (1992) 4189; J.D. Bjorken, K.L. Kowalski and C.C. Taylor, SLAC-PUB-6109, Apr., 1993.
[14] A.A. Anselm, M.G. Ryskin, Phys. Lett. **B266** (1991) 482.
[15] J. -P. Blaizot and A. Krzywcki, Phys. Rev. **D46** (1992) 246.
[16] K. Rajagopal and F. Wilczek, Nucl. Phys. **B399** (1993) 395.
[17] Masayuki Asakawa, Zheng Huang and Xin-Nian Wang, Phys. Rev. Lett. **74** (1995) 3126.
[18] M. Ishihara, M. Maruyama and F. Takagi, Phys. Rev. **C57** (1998) 1440.
[19] James Hormuzdiar and Stephen D.H. Hsu, Phys. Rev. **C58** (1998) 1165.
[20] Jorgen Randrup and Robert L. Thews, Phys. Rev. **D56** (1997) 4392.
[21] T.C. Brooks et al., Minimax Collab., Phys. Rev. **D55** (1997) 390.
[22] M.M. Aggarwal et al., WA98 Collaboration, Phys. Lett. **B420** (1998) 169.
[23] T.K. Nayak et al., WA98 Collaboration, Quark Matter ’97 proceedings, Nucl. Phys. **A638** (1998) 249c.
[24] C.M.G. Lates, Y. Fujimoto and S. Hasegawa, Phys. Rep. **65** (1980) 151.
[25] T.K. Nayak et al., WA98 Collaboration, PANIC ’99 proceedings, Nucl. Phys. A, in press.
[26] B.K. Nandi, Ph.D. Thesis, Utkal Univ. (1999).
[27] B.K. Nandi et al., Phys. Lett. **B461** (1999) 142.
[28] D.S. Mukhopadhyay, Ph.D. Thesis, Univ. of Calcutta (1999).
[29] S. Gavin, Nucl. Phys. **A590** (1995) 163c.
[30] V. Koch, J. Randrup, X.N. Wang and Y. Kluger, Nucl. Phys. **A638** (1998) 447.
[31] Joseph I. Kapusta and Ajit M. Srivastava, Phys. Rev. **D52** (1995) 2977.
[32] Sanatan Digal and Ajit M. Srivastava, Mod. Phys. Lett. **A13** (1998) 2369.
[33] M. Stephanov, K. Rajagopal and E. Shuryak, Phys. Rev. Lett. **81** (1998) 4816.
[34] G. Baym and H. Heiselberg, e-print nucl-th/9905022.
[35] G.V. Danilov and E.V. Shuryak, nucl-th/9908027.
[36] G. Roland et al., NA49 Collaboration, Nucl. Phys. **A638** (1998) 91c., H. Appelhauser et al., NA49 Collaboration, e-print hep-ex/9904014.
[37] H. Heiselberg and J.D. Jackson, e-print nucl-th/9809013.
[38] F. Takagi, Phys. Rev. Lett. **53** (1984) 427.
[39] A.C. Das and Y.P. Viyogi, Phys. Lett. **B380** (1996) 437.

[40] M.M. Aggarwal, V.S. Bhatia, A.C. Das and Y.P. Viyogi, Phys. Lett. **B438** (1998) 357.
[41] K. Werner, Phys. Rep. **232** (1993) 87.
[42] Y.P. Viyogi, ALICE Internal Note 98-52 (1998).
[43] R. Brun et al., CERN program library, W5013, R. Brun et al., GEANT3 users' guide, CERN/DD/EE/84-1,
[44] ALICE Dimuon Forward Spectrometer Technical Design Report, CERN/LHCC 99-22.

Chapter 2

[1] Y.P. Viyogi et al., ALICE Internal Note 95-20 (1995).
[2] Y.P. Viyogi, ALICE Internal Note 98-52 (1998).
[3] A.K. Dubey et al., ALICE Internal Note 99-16 (1999).
[4] R. Brun et al., GEANT3 users' guide, CERN/DD/EE/84-1, R. Brun et al., CERN program library, W5013.
[5] K. Werner, Phys. Rep. **C232** (1993) 87.
[6] M. Gyulassy and X.-N. Wang, Phys. Rev. **D44** (1991) 3501.
[7] V. Balagura, Nucl. Instr. Meth. **A368** (1995) 252.
[8] R.T. Jones et al., Nucl. Instr. Meth. in Phys. Res. A343 (1994) 208.
[9] R. Veenhof, CERN Programme Library, entry W5050;
Igor Smirnov, Heed: simulation of ionisation losses in gas mixtures, version 1.01 (1996);
Stephen Biagi, Magboltz: calculation of transport properties in gas mixtures, version 1 (1997);
Rob Veenhof, Garfield: simulation of gaseous detectors, version 6.26 (1999).
[10] Maxwell 3D Field Simulator version 4.1, Ansoft Corporation, USA, supported at CERN.
[11] P. Sarin et al., DAE Symp. on Nucl. Phys., **B39** (1996) 404.
[12] J.-C. Santiard et al., CERN-ECP/94-17, J.-C. Santiard et al., CERN/LHCC/96-39.
[13] D.P. Mahapatra et al., STAR Note SN-310 (1997).
[14] ALICE HMPID TDR, CERN/LHCC 98-19 (1998).
[15] J.-C. Santiard, GASSIPLEX, version 0.7μm, ALICE Internal Note, in preparation; J.-C. Santiard and K. Marent, Proc. of the Fifth Workshop on Electronics for LHC Experiments (to be published).
[16] M.M. Aggarwal et al., ALICE Internal Note 99-20 (1999).
[17] M.M. Aggarwal et al., Nucl. Instr. Meth. **A424** (1999) 395.

Chapter 3

[1] A.K. Dubey et al., ALICE Internal Note 99-16 (1999).
[2] K. Lang et al., Nucl. Instr. Meth. in Phys. Res. **A420** (1999) 392.
[3] J.C. Santiard et al. ALICE Internal Report, under preparation.
[4] ALICE Dimuon Forward Spectrometer Technical Design Report, CERN/LHCC 99-22 (1999).
[5] O. Villalobos Baillie et al., ALICE Internal Note 98-23 (1998).
[6] R.N. Singaraju et al., VECC Internal Note VECC/EXP/98-21 (1998).
[7] ALICE Photon Spectrometer Technical design Report CERN/LHCC 99-4 (1999).
[8] M.M. Aggarwal et al., Nucl. Instr. Meth. in Phys. Res. **A424** (1999) 395.

Chapter 4

[1] ALICE Collaboration, Technical Proposal, CERN/LHCC/95–71 (1995).
[2] K. Werner, Phys. Rep., **C232** (1993) 87.
[3] M. Gyulassy and X.-N. Wang, Phys. Rev. **D44** (1991) 3501.
[4] M.M. Aggarwal et al., Nucl. Instr. Meth. **A372** (1996) 143.
[5] M.M. Aggarwal et al., Nucl. Instr. Meth. **A424** (1999) 395.

[6] S. Chattopadhyay, Z. Ahammed and Y.P. Viyogi, Nucl. Instr. Meth. **A421** (1999) 558.
[7] Y. Takahashi et al., Nucl. Phys. **A461** (1987) 263c.
[8] K. Rajagopal, e-print hep-ph/9703258.
[9] A.K. Dubey et al., ALICE Internal Note 99-16 (1999).
[10] M.M. Aggarwal et al, WA93 Collaboration, Phys. Rev. **C58** (1998) 1146.
[11] ALICE Photon Spectrometer Technical Design Report, CERN/LHCC 99-4 (1999).
[12] ALICE Zero Degree Calorimeter Technical Design Report, CERN/LHCC 99-5 (1999).
[13] A.L.S. Angelis et al., ALICE Internal Note 97-07 (1997).
[14] Y.P. Viyogi, ALICE Internal Note 98-52 (1998).
[15] Y.P. Viyogi, ALICE Internal Note 95-20 (1995).
[16] M.M. Aggarwal et al., WA93 collaboration, Phys. Lett. **B403** (1997) 390.
[17] G.C. Mishra, Ph.D. Thesis, Utkal Univ. (1999).
[18] R. Raniwala, S. Raniwala and Y.P. Viyogi, ALICE Internal Note 99-32 (1999)
[19] A.M. Poskanzer and S.A. Voloshin, Phys. Rev. **C58** (1998) 1671.
[20] S. Raniwala et al, under preparation.
[21] M. Stephanov, K. Rajagopal and E. Shuryak,Phys. Rev. Lett. **81** (1998) 4816.
[22] E.V. Shuryak, Phys. Lett. **B423** (1998) 9.
[23] G. Baym and H. Heiselberg, e-print nucl-th/9905022.
[24] S.A. Voloshin, V. Koch and H.G. Ritter, Phys. Rev. **C60** (1999) 24901.
[25] G. Roland et al., NA49 Collaboration, Nucl. Phys. **A638** (1998) 91c., H. Appelhauser et al., NA49 Collaboration, e-print hep-ex/9904014.
[26] B.K. Nandi, Ph. D. Thesis, Utkal Univ. (1999).
[27] H. Heisdelberg and A.D. Jackson, e-print nucl-th/9809013 (1998).
[28] J.G. Rushbrooke, CERN Preprint EP/84-35 (1984).
[29] S. Abachi et al., D0 Collaboration, Phys. Rev. Lett. **72** (1994) 2332; ibid **76** (1996) 734.
[30] C.M.G. Lates, Y. Fujimoto and S. Hasegawa, Phys. Rep. **65** (1980) 151.
[31] M.M. Aggarwal, V.S. Bhatia, A.C. Das and Y.P. Viyogi, Phys. Lett. **B438** (1998) 357.
[32] F. Takagi, Phys. Rev. Lett. **53** (1984) 427.
[33] A.C. Das and Y.P. Viyogi, Phys. Lett. **B380** (1996) 437.
[34] A.A. Anselm and M.G. Ryskin, Phys. Lett. **B266** (1991) 482.
[35] J. -P. Blaizot and A. Krzywcki, Phys. Rev. **D46** (1992) 246.
[36] J.D. Bjorken, Int. J. Mod. Phys. **A7** (1992) 4189; J.D. Bjorken, K.L. Kowalski and C.C. Taylor, SLAC-PUB-6109, Apr., 1993.
[37] K. Rajagopal and F. Wilczek, Nucl. Phys. **B399** (1993) 395.
[38] Masayuki Asakawa, Zheng Huang and Xin-Nian Wang, Phys. Rev. Lett. **74** (1995) 3126.
[39] M. Ishihara, M. Maruyama and F. Takagi, Phys. Rev. **C57** (1998) 1440.
[40] James Hormuzdiar and Stephen D.H. Hsu, Phys. Rev. **C58** (1998) 1165.
[41] Jorgen Randrup and Robert L. Thews, Phys. Rev. **D56** (1997) 4392.
[42] T.K. Nayak et al., WA98 Collaboration, Quark Matter '97 proceedings, Nucl.Phys. **A638** (1998) 249c.
[43] James V. Steele and Volker Koch, Phys. Rev. Lett. **81**(1998) 4096.
[44] B.K. Nandi, G.C. Mishra, B. Mohanty, D.P. Mahapatra and T.K. Nayak, Phys. Lett. **B449** (1999) 109.
[45] B.K. Nandi, T.K. Nayak, B. Mohanty, D.P. Mahapatra and Y.P. Viyogi, Phys. Lett. **B461** (1999) 142.
[46] S. Gavin et al., Phys. Rev. Lett., **72** (1994) 2143.
[47] S. Gavin and B. Muller, Phys. Lett., **B329** (1994) 486.
[48] J.I. Kapusta and A.P. Vischer, Z. Phys. **C75** (1997) 507.
[49] M.M. Aggarwal et al., WA98 Collaboration, Phys. Lett. **B420** (1998) 169.
[50] T.K. Nayak et al., WA98 Collaboration, PANIC '99 proceedings, Nucl. Phys. A, in press.

[51] Zheng Huang, Ina Sarcevic, Robert Thews and Xin-Nian Wang, Phys. Rev. **D54** (1996) 750.
[52] "Wavelets in Physics", World Scientific, Singapore, eds. Li-Zhi Fang and Robert L. Thews (1998).
[53] T.C. Brooks et al., Minimax Collab., Phys. Rev. **D55** (1997) 390.
[54] D.S. Mukhopadhyay, Ph.D. Thesis, Univ. of Calcutta (1999).

Chapter 5

[1] ALICE Collaboration, Technical Proposal, CERN/LHCC/95–71 (1995).
[2] I.R. Collins et al., ALICE Internal Note 99-35 (1999).
[3] O. Villalobos Baili et al., ALICE Internal Note 98-23 (1998).
[4] Recommendations for the use of Field-buses at CERN in the LHC era, ICALEPS 1997, Beijing, China, Nov. 1997.
[5] Initial Safety Discussion, TIS Internal Note TIS-GS/WW/cn (99-50).
[6] ALICE Dimuon Forward Spectrometer Technical Design Report, CERN/LHCC 99-22 (1999).